SCIENCE • TECHNOLOGY • RESEARCH HIGHLIGHTS • VISIONS
Dissertation
109

Modelling nuclear fuel behaviour and cladding viscoelastic response

Ville Tulkki

VTT

VTT SCIENCE 109

Modelling nuclear fuel behaviour and cladding viscoelastic response

Ville Tulkki

Senior Scientist, VTT Technical Research Centre of Finland Ltd

Thesis for the degree of Doctor of Science in Technology to be presented with due permission for public examination and criticism in lecture hall M1, at Aalto University, on the October 23rd at 1 pm.

ISBN 978-951-38-8346-1 (Soft back ed.)
ISBN 978-951-38-8347-8 (URL: http://www.vttresearch.com/impact/publications)

VTT Science 109

ISSN-L 2242-119X
ISSN 2242-119X (Print)
ISSN 2242-1203 (Online)
http://urn.fi/URN:ISBN:978-951-38-8347-8

JULKAISIJA – UTGIVARE – PUBLISHER

Teknologian tutkimuskeskus VTT Oy
PL 1000 (Tekniikantie 4 A, Espoo)
02044 VTT
Puh. 020 722 111, faksi 020 722 7001

Teknologiska forskningscentralen VTT Ab
PB 1000 (Teknikvägen 4 A, Esbo)
FI-02044 VTT
Tfn +358 20 722 111, telefax +358 20 722 7001

VTT Technical Research Centre of Finland Ltd
P.O. Box 1000 (Tekniikantie 4 A, Espoo)
FI-02044 VTT, Finland
Tel. +358 20 722 111, fax +358 20 722 7001

Juvenes Print, Tampere 2015

Acknowledgments

The work presented has been performed in projects funded by SAFIR2014, the Finnish Research Programme on Nuclear Power Plant Safety 2011–2014, SAFIR2018, the Finnish Research Programme on Nuclear Power Plant Safety 2015–2018, Academy of Finland (IDEA project grant decision 260493) as well as VTT grant for the finalization of the dissertation. A major part of the work for the last two publications in this dissertation was done during my paternal leave in the spring of 2014, for which I owe a debt of gratitude to the Finnish social security system.

I need to thank many people for enabling me to finish this thesis. First, Professor Filip Tuomisto for his guidance during the last leg of my dissertation process, and Professor Emeritus Rainer Salomaa for the introduction to the field of nuclear engineering so many years ago. Mr Seppo Kelppe has provided both the introduction into the interconnected world of fuel behaviour analysis and the perspective to understand its issues. Dr Timo Ikonen joined our fuel group a few years back and has played a major role both in finally pushing our group to a journal publishing and in my research; without him this work would have been a quite different one and finished a lot later. Pre-examiners Dr Bouloré and Dr van Uffelen both provided valuable comments and suggestions to improve the thesis.

My thanks to Dr Timo Vanttola, our Head of Research Area, and Dr Anitta Hämäläinen, my Team Leader, who have trusted me with both the responsibility and the freedom in doing my work. I am grateful to the members of SAFIR2014 Reference Group 3 for their effort and to the fellow RG3 project managers for the peer support. I'd also like to thank IDEA's project manager Sami Penttilä for his flexibility with the project plan that was never followed. I would like to thank my colleagues at VTT and especially the members of our fuel behaviour group for all the good times. My family has always supported me and friends have helped me to keep the life in context. During my paternal leave my in-laws were a great help, especially Tuula as she, on several occasions, visited us and took to looking after Santeri while I was hiding upstairs writing papers on the creep response.

My work with the transient creep response started after Dr Czaba Györi had (on several occasions) pointed out that the models I used at the time were not correct. I was not able to provide a satisfactory answer to the enigma of the transient creep behaviour at the time; I still cannot, but at least this work is a start. Essential in this

work have been the experimental results obtained in Halden research reactor. My thanks to the members of Halden Project for their great work and to the members of Halden Programme Group for the insights gained. I have had an opportunity to discuss my research during Halden Programme Group meetings, EHPG meetings and various conferences with many people and I would like to thank Margaret McGrath, Jan Klouzal, John Foster, Kenneth Geelhood, Kurt Terrani, Glyn Rossiter, Katalin Kulacsy and many others for the discussions, feedback and encouragement.

And finally, when I was finishing my Master's Thesis, Professor Salomaa advised me not to mention any current sweethearts in the preface. As he said it, "young love is fleeting while the thesis preface is eternal". This was a wisdom from a fellow senior scientist who has seen how the world works, and as such I have always passed the advice on to the people whose theses I have been instructing. It brings me great joy and hope for the humanity that none have heeded this advice.

I would like to thank my beloved wife Sanna for her support and encouragement and our sons, Santeri and Joona, for their constant reminders of the important things in life.

Helsinki, September 18th, 2015,

Ville Tulkki

Academic dissertation

Supervising professor	Prof. Filip Tuomisto Department of Physics Aalto University, Finland
Thesis advisor	Prof. Emeritus Rainer Salomaa Department of Physics Aalto University, Finland
Preliminary examiners	Dr Antoine Bouloré Commissariat à l'Energie Atomique, France
	Dr Paul van Uffelen European Commission, Joint Research Centre, Institute for Transuranium elements
Opponent	Dr Susan Ortner National Nuclear Laboratories United Kingdom

List of publications

This thesis consists of the summary part and the following five publications.

I T. Ikonen and V. Tulkki, "The importance of input interactions in the uncertainty and sensitivity analysis of nuclear fuel behavior", *Nuclear Engineering and Design*, **275**, 229–241 (2014).

II T. Ikonen, H. Loukusa, E. Syrjälahti , V. Valtavirta , J. Leppänen and V. Tulkki, "Module for thermomechanical modeling of LWR fuel in multiphysics simulations", *Annals of Nuclear Energy*, **84**, 111–121 (2014).

III V. Tulkki and T. Ikonen, "Modeling of Zircaloy cladding primary creep during load drop and reversal", *Journal of Nuclear Materials*, **445**, 98–103 (2014).

IV V. Tulkki and T. Ikonen, "Viscoelastic modeling of Zircaloy cladding in-pile transient creep ", *Journal of Nuclear Materials*, **457**, 324–329 (2015).

V V. Tulkki and T. Ikonen, "Modelling anelastic contribution to nuclear fuel cladding creep and stress relaxation", *Journal of Nuclear Materials*, **465**, 34–41 (2015).

Author's contribution

Publication I: The importance of input interactions in the uncertainty and sensitivity analysis of nuclear fuel behavior

This publication presents the work on uncertainty and sensitivity analysis of fuel behaviour modelling tools. The sensitivity to input uncertainties is investigated by applying correlation coefficient and variance decomposition analyses. The paper demonstrates that significant improvements over the traditional first order methods can be achieved by using the higher order methods.

The author was responsible for the task definition and the supervision of the original work the manuscript was based on. The author assisted in the interpretation and the analysis of the results and participated in the writing of the manuscript.

Publication II: Module for thermomechanical modeling of LWR fuel in multiphysics simulations

This publication describes the FINIX development and the initial code coupling results in a multiphysics environment. FINIX is a fuel module developed at VTT meant to be implemented in a wide range of host codes.

The author acted as the instructor in the initial FINIX development. The author participated in the writing of the Sections 1, 2 and 6 of the manuscript.

Publication III: Modeling of Zircaloy cladding primary creep during load drop and reversal

This publication describes the development of phenomenological model for nuclear fuel cladding creep during stress transients. The model was based on the results of the IFA-585 experiment performed at the Halden boiling water reactor. The model was successful in replicating the observed transient behaviour.

The author was the primary author of the manuscript.

Publication IV: Viscoelastic modeling of Zircaloy cladding in-pile transient creep

This publication describes the application of viscoelastic tools to explain the observed transient in-pile creep behaviour of the IFA-699 Zircaloy-4 experiment. The model based on the Standard Linear Solid is shown to be functionally the same as the earlier phenomenological model.

The author was the primary author of the manuscript.

Publication V: Modelling anelastic contribution to nuclear fuel cladding creep and stress relaxation

This publication describes the further development of the viscoelastic model for the description of stress relaxation experiments. The time evolution of the stress relaxation phenomena is shown to require a more complex model than what was needed for the earlier creep experiment modelling. Also, the viscoelastic model formulation is altered to better suit the problem at hand.

The author was the primary author of the manuscript.

Contents

List of symbols

Symbol	Description
A, a_i, n, C_i	Material coefficients for FRAPCON-3.4 creep correlation
C	Ratio of primary creep to stress of phenomenological creep model
E	Elastic modulus
F, G	Fitting coefficients in simplified secondary creep model
g_i	Dirichlet-Prony series weighting factor
K	Fitting coefficient in oxide layer growth model
n	Number of anelastic nodels in model
Q_c	Activation energy of creep
Q_o	Activation energy of oxide formation
R	Universal gas constant
S	Sensitivity index
t	Time
Δt	Time step length
T	Temperature
T_i	Total effect index for ith variable
V	Variance
X	Input variable
Y	Function output
w	Oxide layer thickness
δ_{ij}	Kronecker delta
ϵ	Strain
ϵ_{tot}	Total strain
ϵ_p	Primary creep strain
ϵ_p^S	Saturated primary creep strain
ϵ_s	Secondary creep strain
ϵ_{irr}	Secondary creep strain from irradiation creep
ϵ_{th}	Secondary creep strain from thermal creep
ϵ_i	Strain of ith anelastic component

κ	Spring constant
ν	Viscosity
ρ_i	Correlation coefficient (Spearman rho)
σ	Stress
σ_h	Hoop stress
σ_a	Axial stress
σ_r	Radial stress
σ_{eff}	Effective stress
σ_{int}	Internal stress
σ_{ext}	Externally applied stress
$\Delta\sigma_j$	jth stress step
τ	Time constant for creep
τ_i	Time constant for creep of ith Kelvin unit
Θ	Heaviside function

1. Introduction

Nuclear power plants produce energy by the means of a sustained nuclear chain reaction. Thermalized neutrons cause fissions in fissionable nuclei – ^{235}U or ^{239}Pu – creating two daughter nuclei and several neutrons per fission. These neutrons first slow down with collisions with light atoms such as hydrogen, eventually thermalizing and then potentially causing new fissions that sustain the chain reaction. By-products of these fission events are heat, which is eventually used in the turbines to produce electricity, and daughter nuclei, which are contained within the nuclear fuel rods.

Globally, the two most common types of nuclear reactors in electricity generation are pressurized water reactors (PWR) and boiling water reactors (BWR), collectively known as light water reactors. In light water reactors the nuclear fuel is in the form of near-cylindrical UO_2 pellets with a length and diameter of the order of 1 cm. These pellets are stacked inside a thin-walled tube made from Zirconium alloy that is several metres in height and internally pressurized with helium. The fuel rods are organized into fuel assemblies that together with the cooling water form a critical configuration capable of sustaining the nuclear chain reaction. The fuel rods also provide the first barriers to the spread of radionuclides, as the radioactive isotopes are contained within the UO_2 fuel matrix and within the cladding tubes. However, if the fuel rods break, the radioactive isotopes will spread to the coolant primary circuit, and, should the other barriers fail, to the environment. Hence, knowing the state and the behaviour of the nuclear fuel is of utmost importance to the safety.

Both the cladding and the fuel pellets are affected by the conditions in the nuclear reactor. The pellets first shrink as the fabricated porosity is sintered in the elevated temperatures. The temperature gradient across the pellet radius induces high enough stresses to crack the pellets. The fission products accumulate into the pellets, causing them swell. At a high enough temperature or burnup the gaseous fission products release to the gas gap. These released gases affect the heat conductance across the gas gap, affecting the fuel temperature. Eventually a part of the pellet grain structure reforms into high burnup structure.

During its reactor life, the cladding tube is under pressure differential at elevated temperatures and under irradiation. These conditions cause the cladding to creep, first inwards as the reactor system pressure exceeds the fuel internal pressure, and then outwards as the expanding pellet pushes the cladding. The reactor operation

causes additional alternating stresses, to which the cladding must conform. At high burnup, the rod internal overpressure may even push the cladding to creep outwards faster than the fuel pellet swells, potentially creating a self-reinforcing cladding lift-off effect [1], which may lead to fuel failure. Accidents introduce high temperatures and energetic changes to the fuel [2, 3], and the integrity of the fuel must be ensured in all postulated scenarios.

1.1 Role of fuel behaviour in reactor safety

Traditionally, the main focus in the fuel behaviour analysis is the integrity of the fuel rod. The calculated power and thermal hydraulic conditions are taken as inputs and the state of the fuel is obtained as a result without feedback. Yet the nuclear reactor is a strongly coupled system, where the neutronics depend on the fuel and coolant temperature, the fuel temperature from the neutronics and coolant properties and coolant thermal hydraulics on the amount of heat transferred from the fuel. With the increasing calculational capabilities the combining of the formerly separate analysis has become feasible.

In a steady state situation the amount of heat produced in and conducted from the fuel are equal. In these cases the thermohydraulic analysis of the coolant can ignore the internal state of the fuel. However, the heat conduction across the fuel pellet, the gas gap and the cladding determines the fuel temperature, which in turn directly affects the neutronics and the power produced. In transient situations, both the heat stored in the fuel and the rate at which it is conducted to the cladding–coolant interface are essential in dictating the severity of the event [4].

Propagation of uncertainties across different analysis tools of nuclear reactor calculation chain is a current topic [5]. This is investigated in OECD Benchmark for Uncertainty Analysis in Best-Estimate Modeling for Design, Operation and Safety Analysis of LWRs (UAM-LWR) [6], which has previously been successful in determining and propagating the uncertainties in neutronic calculations. The second phase focuses on fuel behaviour, thermal hydraulics and time-dependent neutronics. On the fuel behaviour side, there are several methodological challenges to be overcome.

It is common for codes of other reactor safety disciplines to use simple fuel models. In the fuel the thermal and mechanical behaviour is coupled, and the fuel properties are influenced by the previous power history. Various models are used to describe and explain the observed fuel behaviour, and utilizing simplified models effectively results in a loss of information. While the uncertainties and sensitivities can be meaningfully propagated across the fuel behaviour code, the effort is wasted if there is no accurate fuel description based on similar assumptions in the application using the propagated values. For instance, there might be a chance of gas gap closing at high power, increasing the heat transfer coefficient considerably. Uncertainty propagation would be very hard to model if accurate thermomechanical behaviour is not taken into account or if the gap conductance is modelled based on different assumptions in different codes. The fuel model using the propagated values should be able to both describe the thermomechanical response and the effect of previous

power history consistently across the codes, otherwise a bias is introduced.

Using models that correctly represent the underlying physics is naturally important. However, there are various phenomena in nuclear fuel behaviour that are not completely understood, for instance cladding transient creep. This governs how the cladding conforms to changing conditions, and affects the fuel behaviour in phenomena such as pellet cladding interaction [7] and lift-off [1]. Creep is defined as a time-dependent strain occurring under stress which is lower than the yield point. The creep processes require elevated temperatures, as often the substantial creep deformation occurs above temperatures of half the absolute melting point of the material. However, this depends on the material, and slow creep is observed in lower temperatures (p. 1 of [8]). Cladding creep behaviour is a complex material dependent problem and the various engineering level correlations are usually fitted to a limited set of data.

The creep response of a cladding tube to changing conditions is conventionally modelled using a strain hardening rule. The rule assumes accumulated strain to be invariant during changes in conditions, and is relatively simple to utilize. However the original experiments [9] which are used to justify the use of the strain hardening rule show that it applies only to a restricted set of conditions. Later on, in-pile creep experiments with on-line instrumentation performed at Halden experimental reactor further challenged the use of the strain hardening rule [10–14]. Yet the use of the strain hardening is widespread in fuel behaviour codes. This is probably due to its ease of use, as fuel behaviour codes require models that are both computationally efficient and easily understandable. In order for a new methodology to replace the strain hardening rule, it needs to be as easy to adopt. The understanding of the cladding stress state and mechanical response to changing conditions affects both performance and safety analysis of nuclear fuel, but a model too complex to be implemented in engineering level application will not be widely adopted.

1.2 Scope of the thesis

The scope of this thesis consists of two main themes. The first is the determination of uncertainty and sensitivity of fuel behaviour modelling and its propagation to the rest of the nuclear reactor calculation chain. The use of correlation coefficient analysis is widespread in the analysis of uncertainty and sensitivity of nuclear systems, but is it sufficient given the complexity of the fuel behaviour? And are the fuel models currently in use in reactor physics or dynamics analysis sufficient in order to accurately propagate the information? This, together with the development of the fuel module FINIX initiated to replace the too simple fuel models in codes of other fields, is the focus of Chapter 2 and Publications [I, II]. The second is the analysis and modelling of cladding response to transient stresses. Is it possible to create a methodology for cladding transient response capable of describing observed behaviour? Is there a physical explanation? Can the methodology constructed for describing in-pile creep be extended to laboratory experiments, as well as to stress relaxation? These issues are addressed in Chapter 3 and Publications [III, IV, V].

The use of too simplified, or non-physical, models introduces bias to the analysis and reduces the accuracy of the results. In safety analysis this is compensated by the use of conservative assumptions and a wide uncertainty range. By introducing more physically accurate models it is possible to both reduce conservatism of the analysis and improve the confidence in the validity of the results.

2. Nuclear fuel behaviour

Many of the engineering level, also called integral, codes describe the fuel rod in cylindrical coordinates, assuming an axisymmetrical, i.e., concentric pellet, gas gap and cladding, geometry. The fuel pellet stack is represented by a continuous material, smearing the small details such as cracks and pellet ends. Both the fuel and the cladding are divided into axial and radial volumes, with tight nodalization in the radial direction. The full thermomechanical interaction of fuel is modelled in the radial direction, but often only free volume gas pressure is communicated in the axial direction. This method is referred to as the 1.5-dimensional approach, and it provides the engineering compromise between the modelling accuracy, the information required and the run time of the models. Dedicated models and correlations are used to obtain a correct description of statistical microscopic phenomena in this deterministic macroscopic nodalization. The power produced is obtained from reactor physics calculations, while the heat conduction to the coolant relies on thermal hydraulic analysis. These form the boundary conditions for the thermomechanical analysis.

Many of the phenomena in the fuel rod are driven by thermal processes. However, the temperature of the fuel is determined not only by the heat from the nuclear reactions but by its conduction across the fuel matrix, gas gap, cladding and the cladding-coolant interface. Gas gap conductance for instance is governed by the gap width and gas composition, which are both influenced by present and past fuel temperatures and irradiation. Conductivities of materials such as ceramic UO_2 are also temperature dependent. As it is, the task of solving the thermomechanical state of the fuel usually requires iterative solution that takes the previous power history into account.

The slow buildup of burnup and its effects work on a very different range of time, temperature and pressure scales when compared to fast and energetic accident situations. Both of these require models of their own, and often there is a separate development of two different lines of codes for steady state and transient phenomena. As much of the fuel rod's performance during transients depends on its state at the beginning of the transient, the steady state codes are often used to initialize the transient model, as is the case of FRAPCON [15] and FRAPTRAN [16, 17] codes. Other possibilities include the use of a database of the state of the spent fuel at a given burnup, as is the default option in SCANAIR [18, 19], or extension of one

code to cover both steady state and transient phenomena as has been done in e.g. TRANSURANUS [20].

2.1 Fuel models in multiphysics analysis

Existing codes can be and have been combined for multiphysics studies. For instance at VTT there have been several coupling schemes involving fuel behaviour such as FRAPTRAN-GENFLO [21] and Serpent-ENIGMA [22]. Internationally external couplings of existing codes have been done, for example, for ENIGMA [23] and TRANSURANUS and DYN3D [24]. There are large platforms enabling code couplings such as the French SALOME platform [25] and MOOSE [26] developed at Idaho National Laboratories. Improved fuel models have also been implemented in host codes [27, 28].

The issues with coupling pre-existing codes often stem from the fact that the codes have been designed as stand-alone tools. The coding conventions, especially in legacy codes, potentially make the coupling difficult. The information between applications is transferred through external tables or functions, which is demanding in the cases of large simulation cases, and in some occasions can result in loss of data. The successful use of the combined system also requires a working knowledge of all the individual pieces. While using dedicated multiphysics platforms alleviates some of these issues, the code compatibility and requirements for both computing power and information remain. The time required for the calculation can also be an issue, as for instance the modelling of all the fuel rods in the reactor in a full-core multiphysics simulation. Also the use of tools developed by separate actors potentially brings issues with intellectual property rights as the licenses may not allow for e.g. the modification or the redistribution of the original code.

Despite the challenges, coupled multiphysics analysis has its benefits. The improved desciption of different phenomena will assist in quantifying the effect of various interactions. Figure 2.1 shows an example from an earlier work on code coupling done at VTT [22]. The reactor physics code Serpent was coupled with VTT's version of the fuel behaviour code ENIGMA, and a simple PWR base irradiation case from IAEA Coordinated Research Programme FUMEX-III benchmark was calculated. The figure shows the calculated centreline temperature and changes in dimensions of the fuel rod as calculated by ENIGMA. The effect of fuel behaviour on the homogenized cross-sections are shown, as well as that of geometry only. While most of the change to the cross-sections stems from the different temperature used, there is also an observable geometry effect stemming from the increased water subchannel size. This is important since the changes in geometry are rarely taken into account in reactor physics analysis.

2.1.1 FINIX development

Development of the FINIX fuel behaviour module was initiated to address the issue of realistic fuel description in reactor safety codes and propagation of uncertainties over

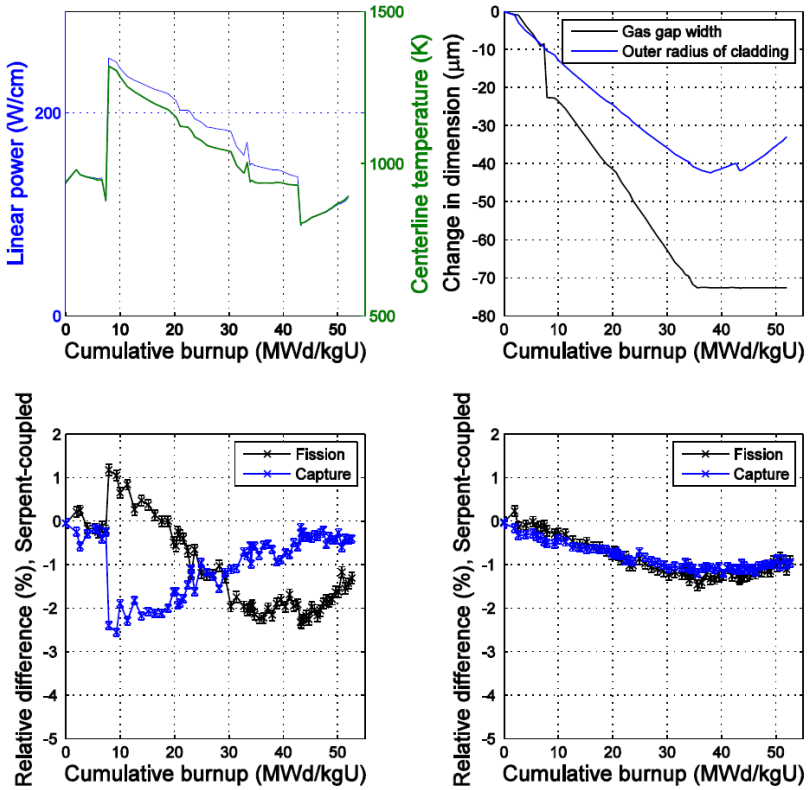

Figure 2.1. (Up, left) The given linear power and the calculated centreline temperatures of the FUMEX PWR. (Up, right) The corresponding changes in the dimensions of the fuel rod. (Down) Homogenized cross-sections of the fully (geometry and temperature) coupled simulation are presented in the left plot and the effect of the changing geometry (temperature constant) is shown on the right. Figure from Ref. [22].

the calculation chain. The aim in the development has been to produce a module with standardized inputs and outputs that can be implemented in a variety of codes. The module itself can be maintained and updated, and the updated version subsequently easily implemented in the host codes. FINIX is to provide a simple but sufficient fuel rod model so that the essential thermomechanical behaviour is reproduced, but with minimal required fuel specific information from the user.

FINIX solves the thermomechanical behaviour of the fuel rod in cylindrical and axisymmetric geometry for several axial nodes. The heat transfer and geometry changes are fully coupled in the radial direction, and the axial nodes are connected via free volume gas pressure, in line with the common 1.5-dimensional approach. The iterative solution scheme of FINIX alternates between solving the heat transfer

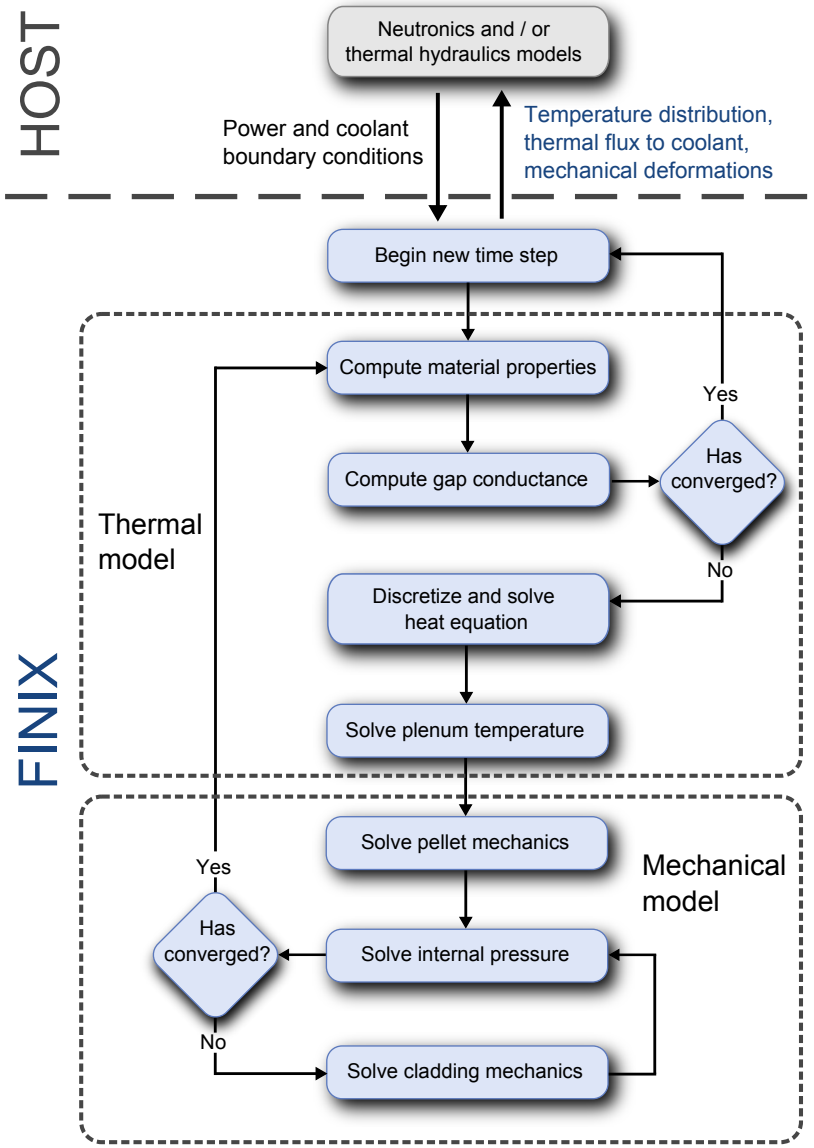

Figure 2.2. Schematic illustration of the FINIX module and its role in a multiphysics simulation. The iteration of the thermal and mechanical solutions is indicated by the flowchart. The convergence checks are assumed to automatically fail on the first iteration.

and mechanical models until a convergence is reached. The scheme is illustrated in Figure 2.2. The flowchart demonstrates the coupled solution to the fuel thermomechanical state.

The initial FINIX development has focused on the thermomechanical behaviour during moderate power transients. The host codes are primarily interested in the thermal feedback in moderate events, and therefore the initial scope of the code development has excluded the high energy phenomena such as cladding ballooning during LOCA and grain boundary fracturing in RIA scenarios. Also, the effects of long-term irradiation such as cladding creep and oxidation, fuel swelling and fission gas release are not modelled yet. The initialization to high burnup can be done with FRAPCON fuel behaviour code.

FINIX uses publicly available correlations to describe the dependence of various material properties on quantities such as temperature, burn-up, chemical composition, etc. The detailed descriptions are available in the FINIX code description [29]. FINIX results have been compared against FRAPTRAN-1.4 fuel behaviour code and experimental data from Halden IFA-429 and IFA-432 test series [I, 30]. The code comparison for reactivity transient simulations show that most of the differences in the results can be attributed either to the differences in the case initialization or the lack of the cladding mechanical models in FINIX. The experimental results are fairly well predicted, with most of the data predicted within $\pm$200 K. Among the used data set, FINIX has a small bias towards underpredicting the temperatures. These differences most probably stem from the lack of dedicated steady state models.

The simulation results can be improved in various ways. Ref. [I] describes the FINIX performance at the state where most of the development had been focused in obtaining a stable transient heat transfer solution. For the transient cases the major improvements can be obtained by the implementation of the mechanical deformation models. For the long term irradiation, various steady state models need to be implemented such as fuel densification and swelling, cladding creep and fission gas models.

It has been assumed that the host code is the expert system providing boundary conditions, such as radial power profile and heat flux from cladding surface to coolant. If the host code does not provide this information, several simple correlations are used by FINIX. Such a case would for instance be reactor physics code which usually does not have a dedicated thermal hydraulics module.

FINIX has been implemented in several VTT in-house codes. These are the Monte Carlo reactor physics code Serpent 2 [31] and the reactor dynamics codes TRAB-1D [32], TRAB3D [33] and HEXTRAN [34]. In the Serpent 2 reactor physics code the integration of FINIX has enabled accurate temperature feedback. This is important in the analysis of reactivity insertion events, where without temperature feedback the reactor power keeps increasing. With increasing temperature the doppler-broadening of capture cross sections inhibits the fission chain reaction, lowering the power. In TRAB-1/3D codes the gap conductance has been modelled with simple correlations or single values, and FINIX provides improved fuel description. The comparison between FINIX and the benchmark fuel rod model of TMI MSLB

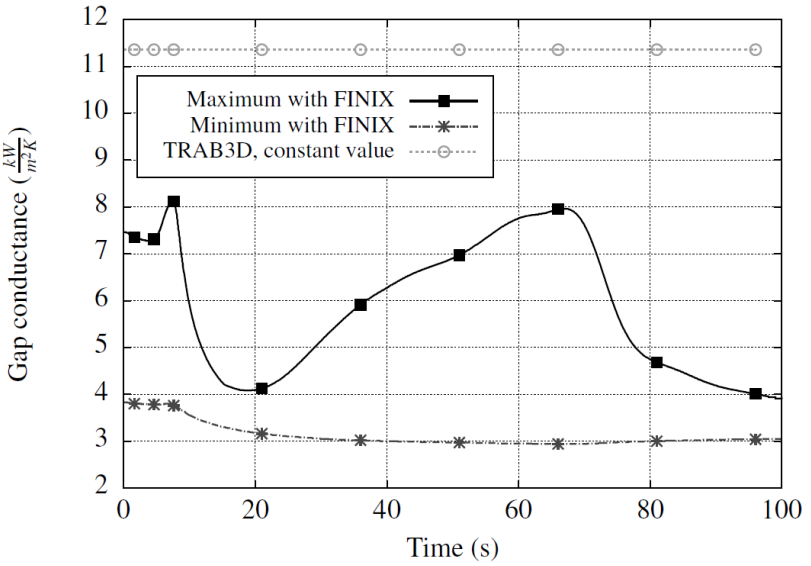

Figure 2.3. Gap conductance with different fuel rod models in the TMI MSLB benchmark.

benchmark can be seen in Figure 2.3, showing both the gap conductance evolution in the FINIX as well as the example of often static gap models utilized in benchmarks. In this particular case the main difference in the simulation results was from the initial fuel temperature [II].

Development of the FINIX module is an on-going work. Future work follows two parallel paths, with the first focusing on improving the fuel modelling capabilities in LOCAs and in steady state, and the second concentrating on developing methods for uncertainty propagation and system initialization with incomplete information. The aim of both is in keeping with FINIX's general goal of enhancing accessibility and reliability of fuel behaviour modelling in multiphysics simulations.

One of the missing models relevant for reactivity insertion events is the model for cladding permanent deformation [30]. It affects the stress relaxation process during the contact between the pellet and the cladding, and influences the fuel behaviour after the pellet cools as the gas gap may re-open. The on-going development of cladding mechanical model is discussed in Chapter 3.

2.2 Uncertainty and sensitivity in nuclear fuel modelling

There are several applications of uncertainty and sensitivity analysis in nuclear fuel modelling. For instance, in Finnish regulatory guides the baseline for safety analysis methodology is to use conservative analysis supplemented with sensitivity studies [35]. The alternative method is the best estimate method supplemented with

uncertainty analysis. The uncertainty and sensitivity analysis can also be used to obtain information on the relationships between input and output variables, thus aiding in focusing the effort in e.g. model development. Uncertainty analysis of fuel performance modelling has been performed by various authors, e.g. Refs. [36–42].

In uncertainty and sensitivity analysis a complex model such as a fuel behaviour code can be represented in a black box fashion as $Y = f(\mathbf{X})$, where Y is the output and $\mathbf{X} = [X_1, X_2, \ldots, X_{k-1}, X_k]$ is the vector of k input variables. Each input X_i is a statistical variable with a given mean μ_i and variance $V(X_i)$. Uncertainty of Y and its sensitivity to the uncertainties of individual X_is can be investigated with various tools.

The most common statistical tool in the nuclear field is Spearman's rank correlation, which is used by, for instance, most of the OECD/NEA CSNI BEMUSE (Best Estimate Methods Uncertainty and Sensitivity Evaluation) programme participants [43]. Spearman's rank correlation coefficient is a measure of how well the relationship between variables can be described using a monotonic function. The correlation coefficient ρ_i is calculated [44]

$$\rho_i = \frac{\mathrm{cov}(x_i, y)}{\sqrt{V(x_i)}\sqrt{V(y)}}, \tag{2.1}$$

where x_i and y are the realizations of the variables X_i and Y arranged in ascending order with ranked values $1 - N$ and $\mathrm{cov}(x_i, y)$ the covariance of these ranks. The correlation coefficient ρ_i can be used to obtain the sensitivity of Y to X_i, with ρ_i^2 estimating the contribution of the ith variable. This method performs well on linear and nonlinear monotonic additive systems. Fuel behaviour codes, with complex models that may change correlations at various points of simulation runs, are not necessarily such systems. Therefore, it was considered necessary also to investigate more advanced methods [I].

In variance decomposition [45] the variance $V(Y)$ is expressed as

$$V(Y) = \sum_i^k V_i + \sum_i^k \sum_{j>i}^k V_{ij} + \cdots + V_{12\ldots k}. \tag{2.2}$$

Here, V_i is the first order effect on the variance $V(Y)$ due to the variable X_i, V_{ij} the second order effect due to the interaction of X_i and X_j, and so on, up to $V_{12\ldots k}$, which is the kth order effect due to the interaction of all k input variables. Dividing both sides of Eq. (2.2) by $V(Y)$ gives

$$\sum_i^k S_i + \sum_i^k \sum_{j>i}^k S_{ij} + \cdots + S_{12\ldots k} = 1, \tag{2.3}$$

where $S_i \equiv V_i/V(Y)$ is the first order sensitivity index, $S_{ij} \equiv V_{ij}/V(Y)$ is the second order sensitivity index, and so on. The sum of all sensitivity indices up to the kth order is one.

Total effect index T_i takes into account all the first-order and interaction effects of one variable X_i. The total effect index for variable X_i is defined as

$$T_i = \sum_{l}^{k} \delta_{il} S_l + \sum_{l}^{k} \sum_{m>l}^{k} (\delta_{il} + \delta_{im}) S_{lm} + \cdots + S_{12\ldots k}, \tag{2.4}$$

where δ_{ij} is the Kronecker delta. For example, for a three-variable model ($k = 3$), the total effect of variable X_1 is $T_1 = S_1 + S_{12} + S_{13} + S_{123}$. By investigating the total effects index T_i and the first order sensitivity index S_i it is possible to estimate the contribution of interaction effects on the resulting uncertainty of output Y.

2.2.1 Case study with FRAPCON-3.4

Uncertainty and sensitivity analysis study was performed [I] with FRAPCON-3.4 fuel behaviour code [15]. The case investigated was a hypothetical irradiation at TMI-1 PWR which is the PWR reference case for the OECD Benchmark for Uncertainty Analysis in Best-Estimate Modeling for Design, Operation and Safety Analysis of LWRs (UAM-LWR) [6]. For the variation in the fuel rod fabrication parameters, the values from the benchmark were used as a guideline, and for the material correlations and computational models the values provided by the FRAPCON developers [15, 46] were used.

The full results of the analysis can be found in the original paper [I], and only the findings relevant to this thesis are discussed here. The input parameters were ranked by their importance to the variance of gap conductivity, internal pressure, fuel maximum and cladding average temperatures, cladding outer diameter, cladding hoop stress and fission gas release fraction. The five most important were, in order:

1. Initial cladding outer diameter,
2. fission gas release model (investigated in this study by varying the diffusion coefficient),
3. cladding thickness,
4. fuel thermal expansion, and
5. cladding creep.

Four of these directly affect the width of the gas gap: Cladding outer diameter and thickness define the initial dimensions, fuel thermal expansion defines the immediate reduction of the width of the gas gap at power and cladding creep coefficient affects the time evolution of the gas gap. The fission gas diffusion coefficient contributes to the eventual fission gas release and the gas composition in the free volume. The results depend on the choice of varied inputs (e.g. whether the initial gas gap width is varied directly or as a function of cladding diameter and thickness and pellet diameter, the only varied parameter in fission gas release model was the diffusion coefficient), as well as the choice of the models (for instance the fission gas model used is very simple and more mechanistic models could change the outcome) but the results obtained can be used as a general guideline.

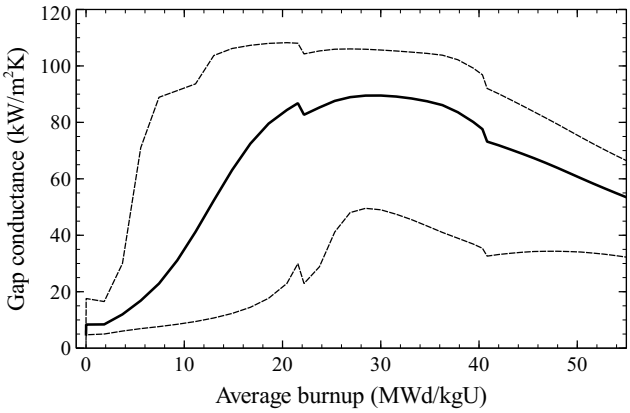

Figure 2.4. The average gap conductance (solid line) and its 95 % confidence limits (dashed lines) as a function of burnup.

Table 2.1. The proportion of variance explained by additive contributions to the gap conductance, as given by $\sum_i^k \rho_i^2$ for different burnups (in MWd/kgU).

Burnup	$\sum_i^k \rho_i^2$
0.01	0.96
5.5	0.95
22	0.65
38	0.68
49	0.76

Figure 2.4 displays the average gap conductance and its 95 % confidence limits at the central axial node as a function of burnup. This is the value of interest to the users of system codes, as it affects the amount of energy deposited in the fuel as well as the rate at which it is conducted to the cladding surface. Unfortunately, the commonly used Spearman rank correlation coefficients do not perform well in explaining the variance in gap conductance at medium to high burnup, as shown in Table 2.1. While at low burnup the Spearman correlation coefficients account for virtually all variance, the 65–76 % ratio of explained variance might not be enough to fully demonstrate the root cause to the observed uncertainty.

The Sobol' sensitivity indices for the gap conductance at the central axial node as a function of burnup are shown in Figure 2.5 for the input variables with the highest contribution. Both the first order effects and the total effect indices are displayed. The variables affecting gap width dominate to 20 MWd/kgU of burnup, and then inputs affecting fission gas release begin to contribute an increasing fraction to the variance in gap conductance. The reason for this is illustrated in Figures 2.6 and 2.7, displaying the averages and 95 % confidence limits of gas gap width and fission gas release fraction. The variance in the gap width is reduced after reaching approxi-

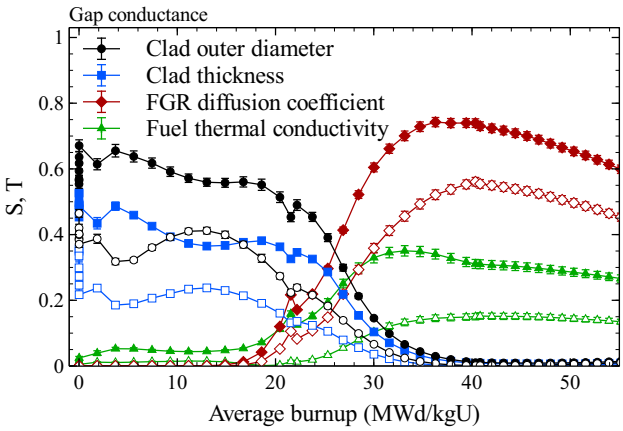

Figure 2.5. Sobol' sensitivity indices for the gap conductance as a function of burnup. Open symbols correspond to the first order effects and the closed symbols correspond to the total effect indices. Error bars indicate 95 % confidence limits. For clarity, only a subset of input variables are plotted in the Figure.

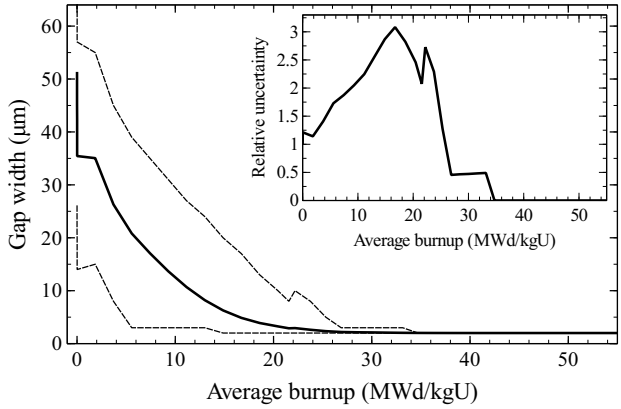

Figure 2.6. Main plot: the average gap width (solid line) and its 95 % confidence limits (dashed lines) as a function of burnup. Inset: the relative uncertainty of the gap width in proportion to the mean gap width.

mately 20 MWd/kgU as the gap closes, whereas the fission gasses are retained in the fuel pellet at low burnup. This demonstrates the need to take previous power history into account when investigating the uncertainties in fuel performance. For accurate uncertainty propagation for low burnup, the factors affecting the gap width are the most important ones. Manufacturing parameters affect both the dimensions and the composition of the cladding and the pellet. And while there are correlations

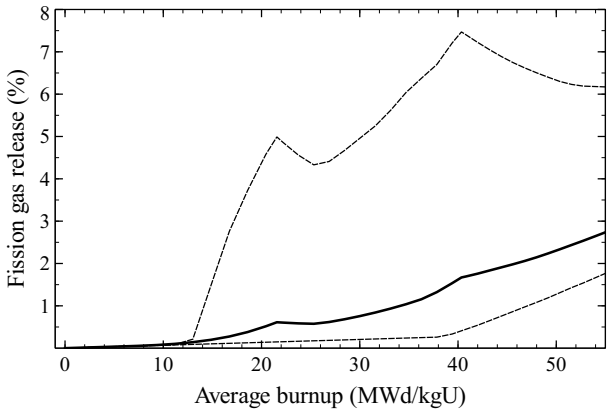

Figure 2.7. The average amount of released fission gas (solid line) and its 95 % confidence limits (dashed lines) as a function of burnup.

fitted to describe the creep of various cladding types, the handling of transient conditions has long been problematic.

While no far-reaching conclusions can be made based on the investigation of a single case, the results suggests that first order sensitivity analysis methods should be used with caution in fuel performance modelling. With the possible exception of fuel centerline (also corroborated by [41]) and cladding temperatures, the analysis should be complemented with higher order methods that take into account input interactions. The specific values for the effects of the inputs will depend on the case investigated as well as the models used to describe the fuel behaviour.

The interactions of the inputs and the necessity for higher order methods stem from the complexity of the system. For the same reason, identifying a single dominant source of uncertainty is not possible. The relative importance of the inputs depends not only on the considered output, but also on burnup. For instance, out of the 21 considered inputs, 15 have a contribution larger than 10 % to the uncertainty of some output at some point in the scenario. In addition to complicating the analysis, this fact also makes it difficult to rule out inputs as a source of output uncertainty.

Last but not least complication is the availability of the uncertainty ranges and distributions, as well as possible correlation between these values, for all the variables to be considered. For instance while there is a wealth of data for thermal conductance of the unirradiated UO_2, same cannot be said for the case of the irradiated UO_2 [41]. The manufacturing parameters, such as the inner radius and thickness of the cladding, may also be correlated due to the manufacturing processes involved. Such information is not readily available. As it is, when performing uncertainty and sensitivity studies, many assumptions must be made a priori.

3. Cladding mechanical response

3.1 Background

Zirconium, having a low neutron cross-section, is especially suited to be a structural material in a nuclear reactor. Various alloys have been developed as Zirconium is too soft and prone to corrosion to be used as a cladding in itself. Variants of Zircaloy-2 are still used in BWRs, whereas in PWRs the previously common Zircaloy-4 is being phased out by advanced materials such as M5, M-MDA and Optimized ZIRLO that endure extended irradiations better [47]. For Russian VVER fuel the cladding has traditionally been E110, which has a 1 % Niobium content.

Zirconium alloys feature hexagonal close packed (HCP) structure, illustrated in Fig. 3.1, leading to anisotropic material properties. During the manufacturing of the cladding this anisotrophy is accentuated as the basal poles are mainly oriented radially.

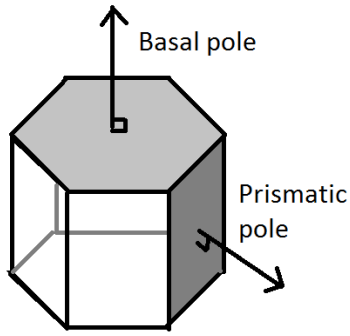

Figure 3.1. Illustration of single chrystal hexagonal close packed structure. Prismatic (dark gray) and basal (light gray) planes and corresponding poles are shown.

3.1.1 Deformation of materials

Materials respond to imposed stresses by deforming. This response depends on both materials and conditions, for instance rubber is more ductile than metals and materials tend to become more ductile as the temperature increases. Depending on the stress and the prevailing conditions, the deformation may be recoverable or permanent, and it may evolve with time. On a macroscopic scale, the deformation properties of materials can be investigated with, for instance, creep experiments, where a load is imposed and the deformation is measured, and stress relaxation experiments, where the sample is forcibly strained and the resulting stress is measured. While the engineering applications are mainly interested in macroscopic response this stems from the microscopic structure of the material in question.

On the macroscopic scale, the material response to stresses has several components, and various authors use same names to represent different material behaviour or its components[1]. In the following the terms *elastic*, *anelastic*, *plastic* and *creep* are used to denote the recoverable immediate, recoverable time-dependent, non-recoverable immediate and non-recoverable time-dependent components of strain, as is common in the literature referring to nuclear fuel cladding. In addition to this, as a cladding mechanical model is constructed, it is defined as *viscoelastic* to represent the fact that, unlike in most models in use, the anelastic response of the material is explicitly taken into account.

For metals the responses usually considered are elastic, plastic and, at elevated temperature, creep responses. In the usual applications anelastic response operates in parallel with primary creep [8], and thus its effect is in part included in the primary creep formulations. Also, the prevailing conditions such as elevated temperatures and the presence of radiation influence the magnitude of the anelastic contribution [54].

[1] According to Nowick (p. 3 of [48]) material behaviour may be

elastic which is time-independent instantaneous recoverable deformation,
plastic which is time-independent permanent deformation,
anelastic which is time-dependent recoverable deformation, and usually also has an immediate component and
viscoelastic which is time-dependent permanent deformation, which may have also immediate and recoverable components.

On the other hand, Was (p. 711 of [49]) defines the strain components as

elastic which is time-independent and instantaneous recoverable deformation,
anelastic which is recoverable deformation depending on strain rate,
plastic which is permanent deformation and
creep as the time-dependent component of plastic strain.

Several authors working on fuel cladding behaviour [50–52] also use terms

elastic for time-independent and instantaneous recoverable deformation,
plastic for time-independent and instantaneous permanent deformation,
creep for the time-dependent permanent strain and
viscoplastic for the combination of plastic and creep strains.

Time-dependent recoverable deformation is either ignored [50–52] or considered as an additional anelastic component [53, 54].

Creep behaviour defines the long-term behaviour of fuel cladding, and it has been widely investigated (e.g. Refs. [50–65]). There are various mechanisms behind creep deformation (Chapter 14 of [49]):

Thermal creep refers to the creep processes occurring in the absence of radiation. These are driven by stress and thermal activation.

- **Dislocation creep** is a form of thermal creep where dislocations glide along slip planes. The creep rate is controlled by obstacles in the planes, which the dislocation must pass by climbing to a plane not intersecting the obstacle.
- **Diffusional creep** is a high temperature, low stress regime creep where the thermal diffusion of vacancies controls the creep rate. Diffusional creep due to volume or lattice diffusion by way of vacancies is termed Nabarro-Herring creep. Grain boundary dominated diffusion dominates at lower temperatures and is called Coble creep.

Irradiation creep refers to the creep processes influenced by irradiation, increasing the total creep rate especially in the reactor operation regime. Irradiation increases the number of interstitials and vacancies.

- **Stress-induced preferential nucleation of loops** (SIPN) is a process where stress influences the formation of interstitial loops preferentially to planes in perpendicular to stress, and inhibits vacancy loop formation to those planes. This causes the solid to increase in length in the direction of the applied tensile stress.
- **Stress-induced preferential absorption** (SIPA) is a process where the atoms are transferred from planes parallel to the applied stress to perpendicular to it.
- **Climb and glide** under irradiation is the same process as the dislocation creep in thermal creep, but assisted by the irradiation defect formation.

Twinning is commonly only a high stress phenomenon, but the HCP structure makes Zirconium alloys susceptible to it (p. 747 of [49], Ref. [47]). It creates a strength differential in tensile and compressive directions [66].

These mechanisms operate at different rates depending on prevailing conditions. The irradiation also causes localized effects thanks to e.g. collision cascades. In reactor conditions for Zirconium alloys most likely mechanism to set the rate for the low stress creep is the SIPA (p. 756 of [49]).

In addition to creep, due to the HCP structure, Zirconium alloys experience irradiation growth. The growth is volume conserving distortion occurring without an applied stress. It expands the lattice crystal in the direction normal to the basal pole and contracts in the direction of the basal pole, in a sense flattening the crystal. Macroscopically this typically results in an increase in the length and decrease in the diameter of the cladding tube due to its manufactured texture.

Anelastic deformation originates from several sources. According to Blanter et al. [67] these are:

Point defects such a interstitial atoms which move or rotate in response to stresses to new positions.

Dislocations or line defects that move to accomodate the external stresses. These are common in materials that have undergone plastic deformation.

Interfaces of the larger scale structures. Examples of such interfaces are grain boundaries, and the relaxation may originate from a grain boundary sliding or movement in normal direction (grain growth).

Thermoelastic relaxation in which spatially heterogenous thermoelastic stresses produce temperature gradients that relax by heat flow.

The sources for anelastic deformation and creep are largely the same, and the difference is in the permanency of the microstructural changes. While some definitions of the term creep include the slow recoverable deformation, and mechanistic deformation models can also exhibit the recoverable component, this in practice has led to ignoring the anelastic component in engineering models. In this work it is assumed that the creep deformation and the anelastic deformation can be separated. In fact, it will be shown that there is no need to assume permanent deformation due to primary creep to explain the results of the instrumented in-pile experiments.

3.1.2 Creep models in fuel behaviour codes

While many of the microstructural phenomena are understood on the mechanical level, most of the engineering scale tools rely on the empirical models. The general form of the correlations stems from either observed or theoretical relationships, and the coefficients are fitted to the experimental data. Often the basic relationships are determined from the laboratory experiments, and the in-pile data is used to adjust the correlation to match the in-pile observations. An example of such an evolution is the thermal creep correlation developed by Matsuo [50] which was later on altered for reactor conditions by Limbäck and Andersson [51] and further developed for the use of the FRAPCON-3.4 fuel behaviour code [15].

Many of the models used by integral codes assume material deformation is a sum of elastic and viscoplastic (creep and plastic deformation) components [50–52, 59]. The creep is assumed to have three phases: primary creep where the strain rate is relatively high but decreasing, secondary or steady state creep featuring a near-constant deformation rate and the tertiary creep phase with quickly increasing strain leading to the breaking of the material. In normal operation the creep rupture and tertiary creep are not of concern as the fuel is in the reactor for only a limited period of time. Thus a common assumption in the creep models utilized in the integral fuel behaviour codes is that the creep strain ϵ_{cr} can be divided into two parts, primary ϵ_p and secondary ϵ_s (also known as steady state creep):

$$\epsilon_{cr} = \epsilon_p + \epsilon_s. \tag{3.1}$$

Table 3.1. Model coefficients of FRAPCON-3.4 creep model for stress relief annealed (SRA) and recrystallized (RXA) cladding.

Coefficient	SRA	RXA
A	1.08×10^9	5.47×10^8
n	2.0	3.5
C_0	4.0985×10^{-24}	1.87473×10^{-24}
C_1	0.85	0.85
C_2	1.0	1.0
$f(T)$, $T < 570$ K	0.7283	0.7994
$f(T)$, $570 < T < 625$ K	$-7.0237 + 0.0136T$	$-3.18562 + 0.00699132T$
$f(T)$, $T > 625$ K	1.4763	1.1840

The secondary steady state part usually consists of thermal and irradiation creep contributions ($\epsilon_s = \epsilon_{th} + \epsilon_{irr}$) [15, 51]. Often the primary creep is a function of the secondary creep rate [50, 51]:

$$\epsilon_p = \epsilon_p^S(1 - e^{f(\dot{\epsilon}_s, t)}), \text{and} \tag{3.2}$$

$$\epsilon_p^S = B \cdot \dot{\epsilon}_s^b, \tag{3.3}$$

where saturated primary creep ϵ_p^S is related to secondary creep rate with constants B and b, and also the time for primary creep to saturate is a function $f(\dot{\epsilon}_s, t)$ of the secondary creep rate.

In this work two creep correlations from the literature are used. The thermal creep correlation by Matsuo [50] and FRAPCON-3.4's correlation [15, 68, 69]. The Matsuo model is

$$\epsilon_{tot} = \epsilon_p^S \left(1 - e^{-52(\dot{\epsilon}_s t)^{0.5}}\right) + \dot{\epsilon}_s t, \tag{3.4}$$

$$\epsilon_p^S = 2.16 \times 10^{-2}(\dot{\epsilon}_s)^{0.109} \text{ and} \tag{3.5}$$

$$\dot{\epsilon}_s = 1.57 \times 10^{13} \frac{E}{T}(\sinh \frac{1.13 \times 10^3 \sigma_h}{E})^{2.1} e^{-\frac{2.72 \times 10^5}{RT}}, \tag{3.6}$$

where T is the temperature in K, t is the time in hours, σ_h is the hoop stress, R = 83144621 J/molK is the universal gas constant and the elastic modulus $E = 1.148 \times 10^5 - 59.9T$ MPa.

FRAPCON-3.4's correlation [15, 68, 69] is effectively the model developed by Limbäck and Andersson [51] modified to use effective stress σ_{eff} instead of hoop stress. The steady state creep correlation components yield relative strain per hour:

$$\dot{\epsilon}_{th} = A \frac{E}{T}(\sinh \frac{a_i \sigma_{\text{eff}}}{E})^n e^{-\frac{Q_c}{RT}}, \tag{3.7}$$

$$\dot{\epsilon}_{irr} = C_0 \cdot \phi^{C_1} \cdot \sigma_{\text{eff}}^{C_2} \cdot f(T) \text{ and} \tag{3.8}$$

$$a_i = 650 \left(1 - 0.56 \left(1 - e^{-1.4 \times 10^{27} \Phi^{1.3}}\right)\right), \tag{3.9}$$

where variables E, T and R are the same as in Matsuo's model, Φ is the fast neutron fluence in neutrons/cm^2, Q_c = 201 kJ/mol the activation energy of the creep,

ϕ the fast neutron flux (n/m^{2}s^{-1}) and variables A, n, C_i and the function $f(T)$ have different values depending on the cladding type and the environment as described in Table 3.1 [69]. The use of σ_{eff}

$$\sigma_{\text{eff}} = \sqrt{0.5((\sigma_a - \sigma_h)^2 + (\sigma_h - \sigma_r)^2 + (\sigma_r - \sigma_a)^2)} \tag{3.10}$$

is justified by an improved modelling of creep in tensile and compressive directions [69]. Here $\sigma_{a,h,r}$ denote stresses in axial, hoop and radial directions and isotropic behaviour is assumed for simplicity.

3.1.3 Creep response to transient stresses

According to the investigations by Lucas and Pelloux [9], the thermal creep deformation at temperatures below 375 °C can be described by a strain hardening rule when the stress is increased. In strain hardening, it is assumed that the creep response follows a curve as seen in single stress level experiments, and the changing stress state is taken into account by moving to the new stress/strain curve at the point where accumulated strain is retained, thus keeping the strain invariant during change. This is illustrated in Figure 3.2. Lucas and Pelloux do note that the strain hardening rule fails in situations where the load is reduced or reversed. Yet their work is used as a justification for the use of the strain hardening rule in most of the models since [51, 59, 70].

Murty and Yoon investigated strain transients following stress changes [53] in laboratory conditions, and proposed a creep model which assumes an anelastic strain component in addition to the traditional elastic and plastic contributions. This anelastic component is used to successfully explain the observed accumulation of reverse strain at load drop, while the traditional plastic contribution from creep is assumed to follow the strain hardening rule. Also, Matsuo investigated the creep behaviour of Zircaloy-4 under variable conditions [70], and formulated a set of rules for stress reversal situations based on reversible creep hardening surfaces.

Several experiments investigating cladding creep response to stress transients have been performed at the Halden Boiling Water Reactor, the most successful to date being IFA-585 [11, 13, 71] and IFA-699 [14]. Halden reactor features the ability for the on-line measurements of in-pile experiments, and these provide a valuable asset for model development and validation. It was observed in both the IFA-585 and IFA-699 experiments that the total saturated primary creep is proportional to the change in the applied stress. This observation challenges both the use of strain hardening rule as well as the models proposed by Murty and Yoon and by Matsuo, as the initial primary creep is similar to the consequent re-initiated primary creep without evidence of subsequent hardening behaviour.

Modelling stress relaxation using creep correlations has been challenging with models using strain hardening rule. In a stress relaxation experiment, a forced strain is applied to a segment and the stress is measured as a function of time. Stress relaxation refers to the observation that the stress imposed by forced strain gradually relaxes. In a stress relaxation experiment the highest stresses are encountered

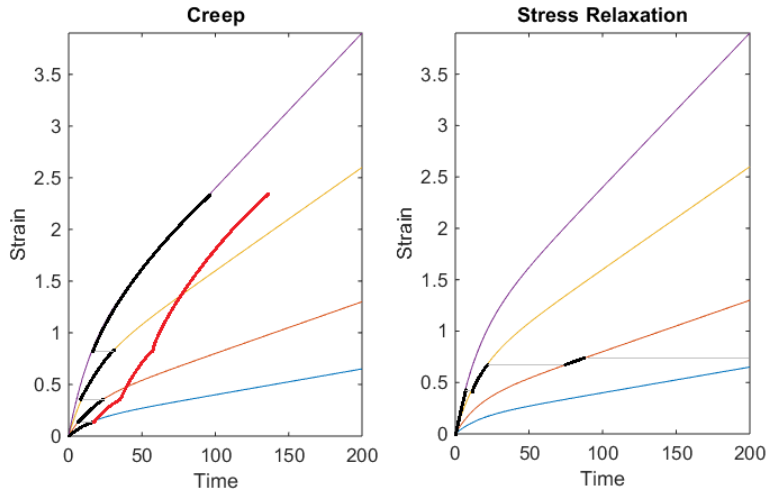

Figure 3.2. Transient creep (left) and stress relaxation (right) behaviour according to strain hardening rule (arbitrary units). Coloured lines indicate creep curves under different conditions, thin gray lines the transition between conditions and black lines the resulting strain curves. In the creep experiment the total actual strain after the first stress step is illustrated with the thick red line. It is assumed in the creep example that the transitions are always to conditions resulting in higher creep rates. In a stress relaxation plot the stress is lowered in each time step, and the strain rate rapidly approaches the steady state rate. In realistic stress relaxation case the stress is constantly diminishing; however, the figure shows a stepwise reduction of stress for illustrative purposes.

when the deformation is applied, and then the stresses reduce as the elastic strain turns into plastic strain. If the strain hardening rule is applied to the constantly diminishing stress case, all the changes advance the apparent time towards the steady state creep region. Effectively, in a stress relaxation experiment, nearly all of the deformation would be accounted for by the steady state creep, as the initial high stress provides enough strain for lower stress primary creep to saturate, as illustrated in Figure 3.2.

Results obtained from stress relaxation experiments have been used to obtain information on cladding creep properties in the region where creep stress dependency is linear, claimed to be the region of less than 150 MPa of stress by the authors of the studies [54, 72]. These stresses are encountered after the initial fast relaxation, and it is implicitly assumed that all the transient behaviour similar to primary creep has already happened during the loading of the sample and the initial fast relaxation. Recent studies [73, 74] claim that by increasing the stress exponent in the creep correlations originally derived from creep experiments by Matsuo [50], the loading and initial relaxation can be also described. However, in these studies it is assumed that all the cladding behaviour can be described with equations originally describing only

the steady state behaviour, which is curious considering the transient nature of the stress relaxation experiments. There are also other interpretations to the stress relaxation results, such as dividing the stresses into transient and remnant [75], but these interpretations do not have direct correspondence to the creep experiments.

Formulations of increasing complexity for describing the exact state of cladding do exist, e.g. [52, 76]. Of interest here is the work of Delobelle et al. [52] where a complex model with kinematic variables is created. They concentrate on describing the anisotropy of the material and intentionally leave out the description of anelastic properties from the model. However, they note that its inclusion would be warranted to describe the cladding response to changing temperature. The model created is still considered too computationally intensive for use in fuel behaviour codes [77] so there is still demand for the simplifying approach.

3.1.4 Cladding mechanical model development

The observations of IFA-585 [11, 13, 71] and IFA-699 [14] experiments prompted the development of an initial purely phenomenological model for re-initializing primary creep [III]. It was assumed that if the saturated primary creep is proportional to the change in stress, this relationship should extend to the whole duration of the primary creep. An internal variable σ_{int} was postulated that would represent the state cladding is conditioned to, and it would change towards the current stress state at a rate relative to the difference between the σ_{int} and the applied stress. The change in σ_{int} would be realized as macroscopic strain. As such, it was possible to formulate a set of equations to describe the primary creep strain $\epsilon_p(t)$:

$$\epsilon_p(t + \Delta t) = \epsilon_p(t) + C(\sigma_{ext} - \sigma_{int}(t))(1 - e^{-\frac{\Delta t}{\tau}}), \tag{3.11}$$

$$\sigma_{int}(t + \Delta t) = (\sigma_{int}(t) - \sigma_{ext})e^{-\frac{\Delta t}{\tau}} + \sigma_{ext}, \tag{3.12}$$

where the notation σ_{ext} has been used for the externally applied stress, t for time and C and τ are coefficients fitted to the experiments. Equations (3.11) and (3.12), together with the initial conditions $\sigma_{int}(t_0) = \sigma_0$ and $\epsilon_p(t_0) = 0$, constituted the phenomenological primary creep model. This was also initially noted [III] and then confirmed [IV] to correspond to the Standard Linear Solid used in the analysis of viscoelasticity. This prompted the continued investigation on the anelastic and viscoelastic properties of the cladding materials [IV, V]. As the work performed in references [III, IV, V] represents a continuity, the intermediate development of the viscoelastic model formulation is not fully detailed in this summary. The model evolution was:

Phenomenological creep model based on assumed internal variable σ_{int} that was able to replicate the observed transient stress response of IFA-585 experiment [III]. Laboratory creep experiments by Matsuo [70] were also investigated, and it was shown that the model performed well if traditional primary creep was assumed.

Standard Linear Solid (SLS) derived model based on Maxwell formulation reproduced observations of IFA-699 Zircaloy-4 well [IV]. It was shown that the SLS solution is identical to the phenomenological model of the earlier work.

General Kelvin model based model was required for simulation of stress relaxation [V]. The internal variable approach was adopted to obtain a numerical solution to the model.

As all the earlier results can also be gained using the more appropriate general Kelvin model based model, the description and formulation of the earlier models is omitted in this work. Those can be found from the references [III, IV].

The goal for the methodology and model development has been the replacement of the widely used strain hardening rule. Since one of the reasons for the wide adoption of strain hardening rule is its simplicity, the replacement model also needs to be simple, easily understandable and computationally light-weight. In this work the focus has been in the stress and strain response of the cladding, and both the temperature and the irradiation effects have been implicitly taken into account by the variable C at this stage.

3.2 Viscoelastic model formulation

In studies of the viscoelastic properties of solids, a common method of describing models is via so-called mechanical analogues. These combine springs representing the elastic component of the material to dashpots representing the viscous components. The springs' displacement is $\epsilon_{\text{spring}} = \sigma/\kappa_i$, where κ_i is the elastic modulus of spring i and σ is the external stress affecting the given component, while the dashpots' rate of displacement is of $\dot{\epsilon}_{\text{dashpot}} = \sigma/\eta_i$, where η_i is the viscosity of the dashpot i.

An analogue with a spring and a dashpot in parallel is called Kelvin, Voigt-Kelvin or Voigt model in the literature. For clarity this two–component construct is called Kelvin unit in this work. A general Kelvin model is a serial arrangement of n Kelvin units and a spring, as depicted in Fig. 3.3. The individual Kelvin units model various relaxation processes that take place at different time scales. The strain response to N step stress increases $\Delta\sigma_j$ at times t_j is [IV]

$$\epsilon(t) = \frac{\sigma(t)}{\kappa_0} + \sum_{j=1}^{N} \Delta\sigma_j \sum_{i=1}^{n} \frac{1}{\kappa_i} \left(1 - e^{-\frac{t-t_j}{\tau_i}}\right) \Theta\left(t - t_j\right), \tag{3.13}$$

where κ_0 is the elastic modulus of the lone spring, κ_i is the elastic modulus of the spring of the ith spring-dashpot system, $\tau_i = \eta_i/\kappa_i$ is the characteristic relaxation time of ith spring-dashpot system and Θ is the Heaviside step function. Higher n provides more accurate representation of a system with multiple relaxation modes at the cost of increasing model complexity. It should be noted that the individual Kelvin units are not meant to represent individual physical processes, but instead a macroscopic aggregate of various microscopic processes acting on similar time scales.

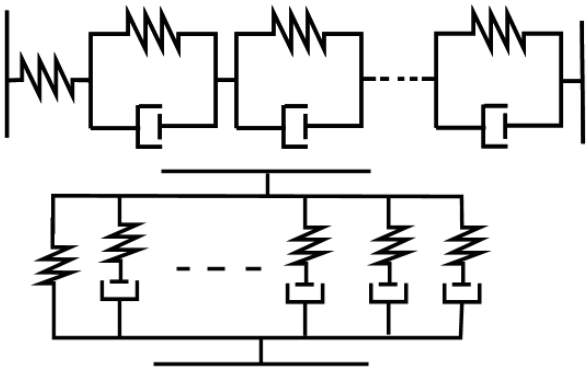

Figure 3.3. Mechanical analogue for the general Kelvin model (top) and the general Maxwell model (bottom).

The general Kelvin model is often used to analyze cases where the stress is a known input, as the stress is transmitted along the whole system as per force balance and the solutions of individual Kelvin units are separable. In the cases where the imposed elongation is known, the general Maxwell model, consisting of a parallel arrangement of a spring and n Maxwell units (a spring and a dashpot in series) is used instead. For both general models using $n = 1$ creates a Standard Linear Solid (SLS) model (see e.g. pp. 87–88 of [78]).

Usually the choice between Kelvin and Maxwell formulations is made based on the topic investigated. The aim here is to construct a model capable of simulating both creep and stress relaxation of fuel cladding. There is also a need to model the steady state creep, and this can be accomplished with a dashpot-like element placed in series to the rest of the solution. The steady state creep dashpot is decoupled from the rest of the solution in the imposed stress case but coupled in the imposed strain case. Therefore, the "pure" solution to the general Kelvin model in the creep simulations can still be obtained, while no such advantage can be had with the general Maxwell model. Therefore the former was chosen as a basis for the model.

The special case of the general Kelvin model with $n = 1$ units yields exponential time evolution, i.e. $e^{-t/\tau}$ for the anelastic deformation or primary creep. For Zirconium alloy claddings, the time evolution of primary creep has been argued to be of the form $e^{-\sqrt{t}}$ [50, 51] or a more complex one [53]. The $e^{-\sqrt{t}}$ form in particular is an instance of a stretched exponential or Kohlrausch function [79, 80], which describes a system with several relaxation mechanisms operating at different rates. The stretched exponential can be approximated by a Dirichlet-Prony series (a weighted sum of exponential functions) [81]:

$$e^{-(t/\tau)^{\beta}} \approx \sum_{i=1}^{n} g_i e^{-t/\tau_i} \tag{3.14}$$

where each instance of e^{-t/τ_i} describes a relaxation mechanism with a time constant of τ_i and weight of g_i where $\sum g_i = 1$. This is the mathematical background justifying use of general Kelvin models with $n > 1$ to describe the systems with observed time evolution of the type of Eq. (3.14).

3.2.1 Computational model

A model is constructed with a spring for elastic response, n number of Kelvin units and a dashpot for creep deformation, all in series. While conventionally the creep deformation includes the primary creep, in this model the primary creep is as a whole given by the Kelvin units. This is in line with observed in-reactor creep behaviour [13, 14]. In general the higher the model's n the better the description. However, this both increases the complexity of the model and sets requirements for the amount and quality of the experimental data. The system for $n = 2$ is displayed in Fig. 3.4.

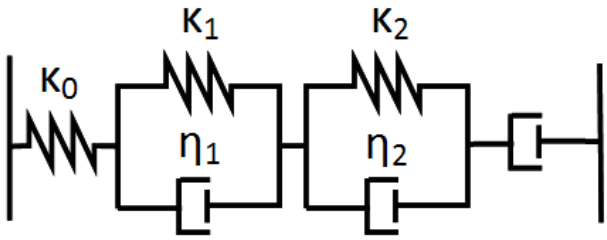

Figure 3.4. Mechanical analogue for the model describing cladding mechanical response containing a series of spring, two Kelvin units and a dashpot representing the creep deformation.

The number of components in a system as depicted in Fig. 3.4, as well as non-linearity of most creep deformation correlations, makes finding an analytical solution to the system challenging. A common engineering solution [82] is to use the internal variable approach, where the strain of each individual component is calculated.

For stress relaxation an explicit numerical solution is used, calculating the stress arising from the elastic deformation of the lone spring based on the difference between the imposed strain and the strain of Kelvin units and the lone dashpot as per Eq. (3.15). This stress determines the system stress as a whole. Then the strains of the Kelvin units and the lone dashpot are calculated assuming the stress stays constant for the duration of the time step. The strains of the Kelvin units are calculated based on Eq. (3.16) and the steady state creep strain from Eq. (3.17):

$$\sigma(t) = \left(\epsilon_{tot}(t) - \epsilon_s(t) - \sum_{i=1}^{n} \epsilon_i(t) \right) \kappa_0, \tag{3.15}$$

$$\epsilon_i(t+\Delta t) = \epsilon_i(t) + (\sigma(t) - \epsilon_i(t)\kappa_i) \cdot \left(1 - e^{-\frac{\Delta t}{\tau_i}}\right) \kappa_i^{-1}, \tag{3.16}$$

$$\epsilon_s(t+\Delta t) = \epsilon_s(t) + f(\sigma(t)) \cdot \Delta t, \tag{3.17}$$

where ϵ_{tot} is the total (imposed) strain, κ_0 the elastic spring constant, ϵ_i, κ_i and τ_i are the strain, spring constant and characteristic time of the ith Kelvin unit, ϵ_s is the steady state creep strain, Δt the time step used and σ the stress. $f(\sigma)$ denotes the function for the steady state creep rate, which may be a simple function of stress or a more complex function such as the ones used by Matsuo [50] or Limbäck and Andersson [51]. This solution scheme requires using very short time steps in stress relaxation cases.

For solving the system during imposed stress (creep experiment), Eqs. (3.16) and (3.17) can be used directly as the stress σ is known and each Kelvin unit as well as the lone spring and the lone dashpot experiences the same stress. In order to ascertain the strain of the whole system ϵ_{tot} the individual strain components are combined:

$$\epsilon_{tot}(t) = \frac{\sigma(t)}{\kappa_0} + \epsilon_s(t) + \sum_{i=1}^{n} \epsilon_i(t). \tag{3.18}$$

Similarly to the model used in references [III, IV] this approach provides an exact solution to the cladding creep behaviour at given stress with arbitrary time step.

For the simulations initial values for the internal strains ϵ_i are needed. In this work an assumed value of $\epsilon_i(0) = 0$ has been used unless otherwise specified. The validity of this assumption will be discussed later.

3.2.2 Qualitative behaviour

The contribution of the anelastic strain component is demonstrated with an investigation of the qualitative behaviour of two models, a reference model with elastic and creep components and the viscoelastic model with elastic, anelastic and creep components. The former model corresponds in behaviour to the traditional strain hardening models in situations where enough strain has been accumulated for the primary creep to be fully developed. The anelastic component is modelled with a single Kelvin unit yielding slow recoverable deformation, whereas the elastic and creep components are the same in both models.

One technique for investigating the metal transient response is called stress dip experiment (e.g. p. 67 of Ref. [8]). In the experiment, a load is first applied to a sample until a steady strain rate is achieved. Then, the load is reduced for a while and finally increased to its original value. According to Ref. [8], the sample deformation appears to stop for a while at the load reduction before it starts to creep at the rate corresponding to the reduced stress. After the subsequent increasing of the stress the strain rate increases for a while before returning to the strain rate corresponding to the applied stress. Models not taking the anelastic contribution into account do not explain these observations but, as illustrated in Fig. 3.5a, the observed behaviour is well in line with the one provided by the viscoelastic model.

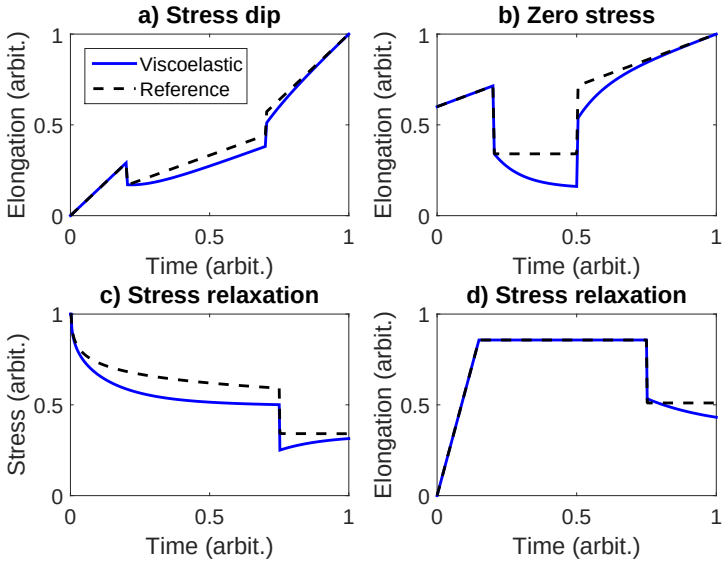

Figure 3.5. Qualitative behaviour of viscoelastic model as compared to a reference model with purely elastic and creep components. The solid line denotes the viscoelastic model and the dashed line the reference model results. In the simulation shown in the upper left plot (a), the sample stress has first been held until steady state creep has been obtained. Then the stress is reduced for a while, and returned to its original value. The viscoelastic model shows an apparent stop at stress dip, and faster elongation at the return to stress. The upper right plot (b) features a similar situation, but with the stress reduced to zero. The apparent deformation continues in the viscoelastic model, but will return to in line with the previously achieved rate as is seen in several experiments [51, 83]. The lower left plot (c) features a stress relaxation experiment where the elongation is reduced mid-experiment as per Ref. [75]. The viscoelastic model shows in this particular case an increase in stress as reported. In the lower right plot (d), the stress relaxation experiment ends with a release of the sample, yielding $\sigma = 0$ at the last part of the plot. This causes a viscoelastic deformation that is not seen if the sample deformation is assumed to consist of solely elastic and plastic components.

Several authors of experimental papers [51, 83] describe issues encountered when, during a creep experiment, the stress is reduced to zero while the sample is still at the experimental temperatures. Limbäck and Andersson [51] describe the need to quickly cool down the sample before the creep recovery sets in, and Kozar et al. [83] measure the change in strain during the zero stress period. Fig. 3.5b shows the difference between traditional and viscoelastic interpretation following a prolonged zero stress period. It should be noted that it is common to clean up such periods of zero stress from experimental results, as according to strain hardening

rule they should not have any effect on the sample strain. However, this results in fast dips in measured strain, which is subsequently recovered, as seen for instance in Fig. 3 of Kozar et al. [83]. It should be noted that Harries [84] explained the observed behaviour with anelastic strain component already in the 1970s.

Kapoor et al. [75] have performed stress relaxation experiments where they attempted to expedite the acquisition of what they call remnant stress (stress remaining after a long time from the beginning of the stress relaxation experiment) by stepwise reduction of imposed elongation. They report observing on some occasions that after the elongation reduction the stress of the sample increases, contrary to what the creep models would indicate. As demonstrated in the Fig. 3.5c this can be explained by the viscoelastic properties of the material. The plot also shows that the addition of an anelastic component to the mechanical model increases the rate of initial stress relaxation.

Finally, the strain recovery annealing experiment is illustrated in Fig. 3.5d. While the rate of stress relaxation depends on the assumed creep strain rate, one definite viscoelastic effect can be demonstrated. At the end of the stress relaxation experiment when the loading device is relaxed, i.e. no elongation is imposed and the stress of the sample is at zero, the anelastic deformation continues if the elevated temperature is maintained. Should the deformation be purely creep no deformation should be seen after the load is removed. The same effect can be obtained with post test annealing of the samples. Such observations of strain recovery annealing are reported by Causey et al. [54] who describe them being anelastic in nature.

3.2.3 Validation cases

The cases investigated with the developed model were the in-pile experiments IFA-585 (BWR segment) [III,13] and IFA-699 (Zircaloy-4 segment) [IV,14], and laboratory experiments by Matsuo (creep response to transients) [III, 70] and Delobelle et al. (stress relaxation) [V, 52].

IFA-585 experiment featured a pre-irradiated BWR cladding tube that was pressurized to several stress states, both compressive and tensile, while under irradiation in the Halden research reactor. The cladding deformation was measured with on-line diameter gauges which were calibrated to unpressurized reference diameters on the end plugs. There was also a composite PWR rod in the test but, as the diameter measurements were reported [10] to be anomalous relatively early on in the experiment, it was not included in the analysis. The BWR rod sample was irradiated prior to the Halden experiment in a commercial reactor to a fast neutron dose of 6×10^{21} n/cm^2. Also, during the first experimental cycle there were issues with rod pressurization which are not included in the analysis. For the simulations it was assumed that the cladding had been conditioned to the $\sigma_{eff} = -52$ MPa at $t = 0$, which was the planned effective stress on the cladding in the initial cycle. The temperature of the cladding sample varied between 575–595 K.

IFA-699 investigated the creep of the Zircaloy-4, E110, M5 and M-MDA cladding tube segments containing fuel pellets for a realistic temperature gradient. The experiment was still on-going during the writing of the recently declassified Halden Work Report HWR-882 [14], but at the time it had lasted for nearly 3000 full power hours and had subjected the cladding samples to hoop stress levels of 0, -75, -50 and +30 MPa of hoop stress, with negative values indicating compression and positive values tension. This was achieved by alternating the segment internal pressure (to 18.2, 8.5, 11.6 and 22.7 MPa) while the external pressure was at a steady 16.2 MPa, simulating PWR conditions. The model was compared with the measurements of Zircaloy-4 segment. The mid-wall cladding temperature was estimated to be approximately 625 K.

Matsuo performed several laboratory experiments investigating transient creep of Zircaloy-4. For examining the Matsuo's out-of-pile tests the experimental data points were extracted from Figures 3, 4, 7 and 9 of Ref. [70]. The data details creep behaviour during load increase from 77.9 MPa to 148.1 MPa of tensile hoop stress, load drop from 156.9 MPa to 74.3 MPa of tensile hoop stress and two series of load reversal steps alternating between tensile hoop stress of 148 MPa and compressive hoop stress of 78 MPa. Cladding temperature during these tests was 662.9–664.0 K.

Delobelle et al. [52] performed various experiments, including both creep and stress relaxation, for Zircaloy-4 samples with two different experimental heat treatments. As they performed both experiments using similar samples it was possible to use the creep experiment to determine the required material-dependent coefficients for the viscoelastic model and use them to simulate the stress relaxation experiment. While Ref. [52] provides a wealth of experimental data, most of it focuses on investigation of material anisotropy. Uniaxial data from the publication was used. It concerned the experiments in the axial direction for both the recrystallized (R) and the cold worked stress relieved (CWSR) Zircaloy-4 at 623 K (350 °C). The data for creep experiment was taken from Fig. 16 and for stress relaxation from Fig. 15 of Ref. [52]. All the experiments discussed were performed at the same temperature. In the creep experiments the stress was increased stepwise and the elongation measured. For the R sample, the stress steps used were 125, 135, 150 and 170 MPa, and for the CWSR sample 170, 250 and 300 MPa. In the stress relaxation experiments the sample was deformed to a desired strain at the rate of $6.6 \cdot 10^{-4} \mathrm{s}^{-1}$. Then the strain was held constant for 48 hours and the stress measured. The strain steps were 0.4 %, 0.8 %, 1.2 %, and 4 % for the R sample and 0.4 %, 0.8 %, and 1.2 % for the CWSR sample.

Steady state creep rate, while not the focus of this work, has a strong effect on the results as all the possible errors are compounded. Steady state creep rate is also affected by material composition and the final heat treatment. As all the cases investigated featured different samples and conditions, different steady state creep models were used in the analyses.

For the analysis of the IFA-585 and IFA-699, the FRAPCON-3.4's steady state correlation (Eqs. (3.7) and (3.8)) was used. There were uncertainties in the IFA-585 test results [12], especially related to the effect of the different rates of oxide layer growth between the sample and the end plugs and experimentally measured secondary creep rate [13]. For the steady state creep it has been noted that IFA-585 experiment features very high secondary creep rates [13] compared to other creep experiments such as those of Ref. [59]. This was also seen in the initial analysis. For IFA-585 analysis the FRAPCON-3.4 correlation used for secondary creep rate was multiplied by a factor of 2 in order to better match the experimental results.

For analysis of the Matsuo's out-of-pile tests the secondary creep part was modelled after the correlation by Matsuo (Eqs. (3.4)– (3.6)) multiplied by a factor of 1.25 for improved correspondence with experimental results. This was required by the fact that Matsuo used $e^{-\sqrt{t}}$ time evolution of primary creep contrary to the e^{-t} of the SLS model. The former evolution features a long tail which was partially compensated by the multiplication. As the correlation uses hoop stress as a driving force and the experiment was reported using it, the hoop stress was used as a driving force in the analysis.

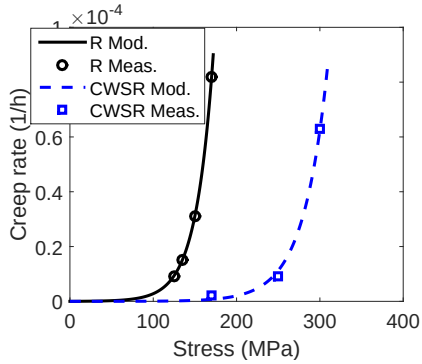

Figure 3.6. Steady state creep rate for R and CWSR claddings as a function of applied stress. Lines represent model results and circles and squares values calculated from experimental data. Experimental data obtained from Fig. 16 of [52] and simulated rates as per Eq. (3.19).

The analysis of the experiments by Delobelle et al. used a simple engineering model for the modelling of the steady state creep:

$$\dot{\epsilon}_s = F \sinh(G\sigma), \tag{3.19}$$

where coefficients $F = 4.5168 \times 10^{-6}$, and $G = 4.2416 \times 10^{-7}$ for R sample and $F = 4.82 \times 10^{-2}$ and $G = 3.43 \times 10^{-2}$ for CWSR sample are fitted to the steady state creep data obtained from Fig. 16 of [52]. The resulting steady state creep rates are displayed in Fig. 3.6. The use of a hyperbolic sine function is a common engineering approximation used to cover both the low stress region below 100 MPa where $\dot{\epsilon} \sim \sigma$

Table 3.2. Model coefficients used to model the elastic and anelastic contributions to the strain.

Cladding	κ_0 (MPa)	κ_1 (MPa)	κ_2 (MPa)	τ_1 (h)	τ_2 (h)
IFA-585 n = 1	N/A	5.2×10^5	–	100	–
IFA-699 n = 1	N/A	2.0×10^5	–	40	–
Matsuo n = 1	N/A	2.6×10^4	–	40	–
Delobelle R n = 0	3.9×10^4	–	–	–	–
Delobelle R n = 1	3.9×10^4	2.52×10^4	–	26	–
Delobelle R n = 2	3.9×10^4	4.80×10^4	4.49×10^4	6.5	65
Delobelle CWSR n = 0	7.3×10^4	–	–	–	–
Delobelle CWSR n = 1	7.3×10^4	2.08×10^5	–	24	–
Delobelle CWSR n = 2	7.3×10^4	4.40×10^5	3.03×10^5	8.0	80

and the high stress region where $\dot{\epsilon} \sim \sigma^5$ [85,86]. Delobelle et al.'s experiments were performed in the axial direction, so axial stress was used.

Table 3.2 lists the coefficients used in the anelastic part of the model. The model used in IFA-585, IFA-699 and Matsuo investigations corresponds to the viscoelastic model with n = 1. Originally the coefficients to IFA-585 and Matsuo cases were obtained by estimating the fitting visually [III]. For IFA-699 the time constant used in the Matsuo experiments was considered adequate [IV]. For the Delobelle experiments the κ_i and τ_i were fitted with Matlab minimization routine to the initial creep step, and in the n = 2 case it was assumed that $\tau_2 = 10\tau_1$ [V]. Elastic response, represented by κ_0, was not used in the analysis of the Halden and Matsuo experiments. The data used for the Halden experiments had been processed and the elastic contribution had been removed. The experimental procedure used by Matsuo, where the measurements were performed outside the furnace, also does not measure the elastic strain. Original papers on IFA-585, IFA-699 and Matsuo experiments [III, IV] used C as a correlation between stress and observed primary creep. This has been converted to the format presented in this work with relation $C = \kappa_1^{-1}$.

3.3 Results

3.3.1 In-pile creep

The comparison between the simulated and measured strain, together with the applied effective stress for IFA-585 experiment, is shown in Fig. 3.7. The mid-wall effective stress with positive values signifying tension and negative values compression is also shown in Fig. 3.7. The match between the experiment and the simulation is good, especially at the beginning of the experiment. However, errors, mostly due to the uncertainties in the secondary creep rate, compound during the simulation. In Fig. 3.8 only the initial strain after each stress step is shown and the plotting of the strain at the beginning of each stress step is shifted to zero. The results show excellent agreement between the simulated and measured behaviour. Thus it can

be argued that the error seen in Fig. 3.7 is mostly due to the uncertainty in the apparent secondary creep rate, and that the creep response to stress reversal can be modelled using the viscoelastic model.

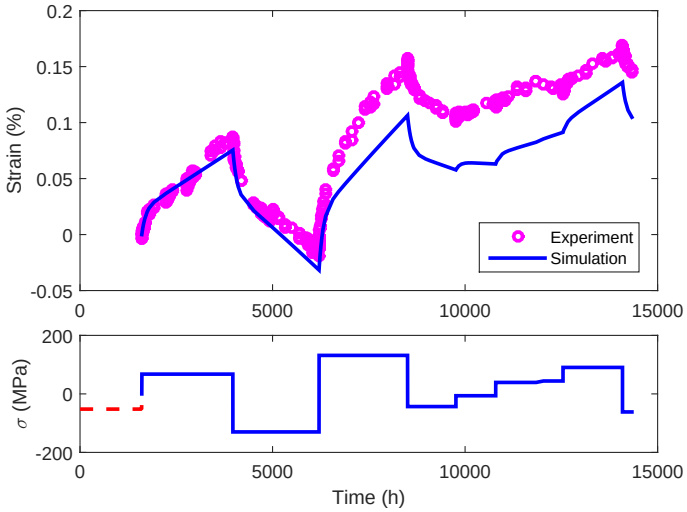

Figure 3.7. IFA-585 BWR experiment (circles) and simulated behaviour (line). The applied stress history is displayed in the bottom plot.

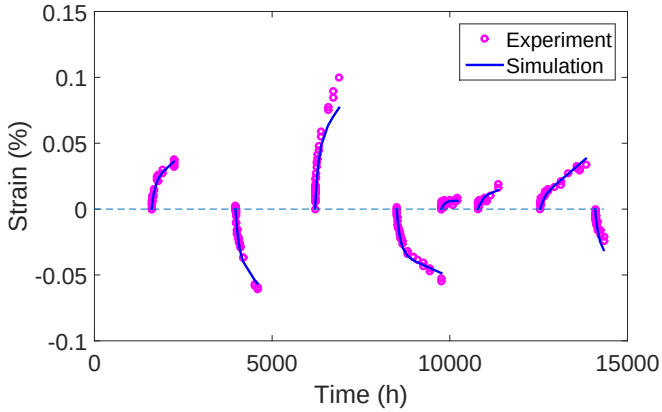

Figure 3.8. The model behaviour against measurements for the beginning of each stress step. The plots start at $\epsilon = 0$ at the beginning of each pressure step.

For IFA-699 Zircaloy-4 experiment the measured values are shown as dots and the base simulation as a solid line in Fig. 3.9. The measured values in Fig. 3.9

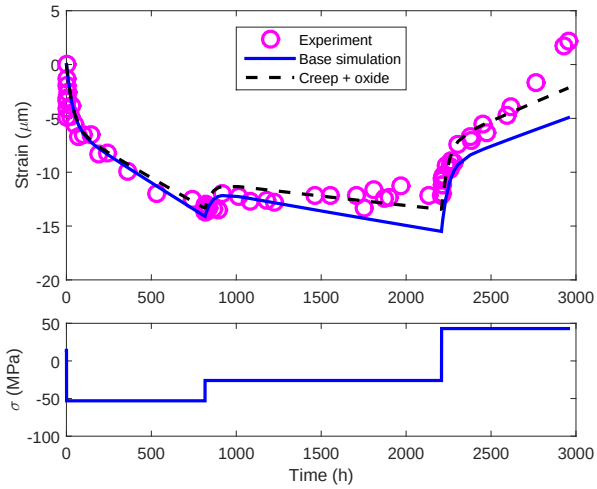

Figure 3.9. Creep of Zircaloy-4 segment in IFA-699 experiment, with measurements shown in circles and simulated values with lines.

consistently trend toward the positive (or tensile, outward) direction. An oxide growth contribution was included to the simulations according to Eq. (3.20) [87]

$$w = Ke^{-\frac{Q_o}{RT}} t^{1.02474} \tag{3.20}$$

where assuming a constant temperature, w is the formed oxide layer thickness in μm, K = 23663.76 $\mu m \cdot h^{-1}$, Q_o/R = 8645.4 K is the activation energy for the oxide formation, T = 625 K is the interaction layer temperature and t is time in hours. As the oxidation replaces metal with less dense oxide, the net effect is the increase of the apparent diameter by a fraction of one third of the oxide layer thickness. The creep with oxide layer contribution is shown with a dashed line in Fig. 3.9. This case would represent a situation where the Zircaloy-4 segment is heated by the fuel inside and thus oxidises faster than the measurement calibration piece which was assumed to be at coolant temperature (approximately 50 K lower than the test sample). The oxide layer equation employed is a simple formula fitted to publicly available post-irradiation data for PWR fuels with Zircaloy-4 cladding, and as such caution should be used when utilizing it for samples in Halden flask conditions.

3.3.2 Out-of-pile behaviour

The results of the simulations of Matsuo experiments are shown in Figures 3.10a–d as the *baseline* line. While for Fig. 3.10a the match is good, the experiments with load reversals, depicted in Figures 3.10c and 3.10d, demonstrate the need for additional assumptions. The transient creep during the subsequent stress steps was clearly smaller than during the initial primary creep stage. Matsuo uses in his work [70] a

concept of creep hardening surface. In the viscoelastic model similar improvement can be achieved by assuming that there are hardening processes which double the value of κ_i after the first transient, simulating traditional primary creep. With such an assumption, simulation results according to the *hardening* line in Figs. 3.10a–d were achieved.

Figure 3.10a shows the results of a test where the hoop stress was first set σ_h = 77.9 MPa and then increased to σ_h = 148.1 MPa. The match between the experiment and simulation is good, and here the effect of the hardening is not overly clear. It should be noted that this kind of experiment where the stress is increased is where the strain hardening rule provides good results.

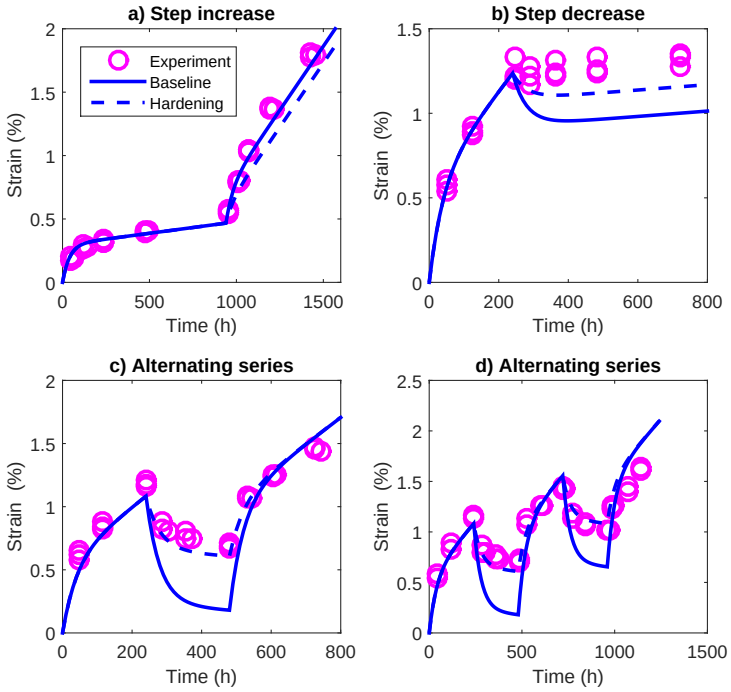

Figure 3.10. Simulated (lines) and experimental (circles) cladding response to a) step stress increase, b) step stress decrease, c) series of stress reversals and d) series of stress reversals. Experimental data from Figures 3, 4, 7 and 9 of Ref. [70].

Figure 3.10b shows the results of a test where the hoop stress was first set σ_h = 156.9 MPa and then reduced to σ_h = 74.3 MPa. Matsuo notes that "a certain amount of strain recovery is observed just after the load drop" [70] which is also shown by the viscoelastic model. The strain recovery phenomenon is documented also by Murty [53]. The discrepancy between the simulation and the experiment can be mostly attributed to a slightly too low secondary creep rate.

Figures 3.10c and 3.10d show the results of two experiments where the load was alternated between tension (σ_h = 148.1 MPa) and compression (σ_h = −78.0 MPa). Here the need for assuming some hardening behaviour in primary creep is evident. The match between the experiment and simulation is good, therefore demonstrating the applicability of the model in load reversal situations also for out-of-pile conditions. The need for the hardening assumption which was not needed in the IFA-585 and IFA-699 analysis raises a question whether the Zirconium alloy primary creep behaviour during in-pile and out-of-pile experiments are equivalent.

The simulations of the Delobelle et al. creep and stress relaxation experiments are shown in Fig. 3.11 for R samples and in Fig. 3.12 for the CWSR samples. The simulations are performed with models with 0, 1 and 2 Kelvin units. The model with 0 Kelvin units is shown only for the stress relaxation plot, where it represents the traditional strain hardening law model in stress relaxation, as discussed in Section 3.1.3.

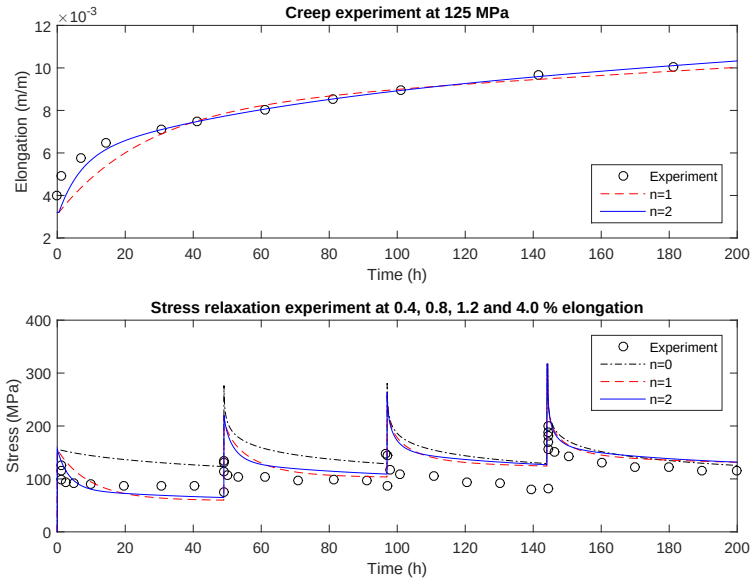

Figure 3.11. Creep and relaxation of R samples. Comparison between the experimental data (circles) and simulations with model with a different number n of Kelvin units. n = 0 represents the pure elastic and creep deformation.

3.4 Discussion

The anelastic contribution to cladding mechanical behaviour has been investigated and accounted for in some models in the 1970s and 1980s [53, 54, 84, 88]. How-

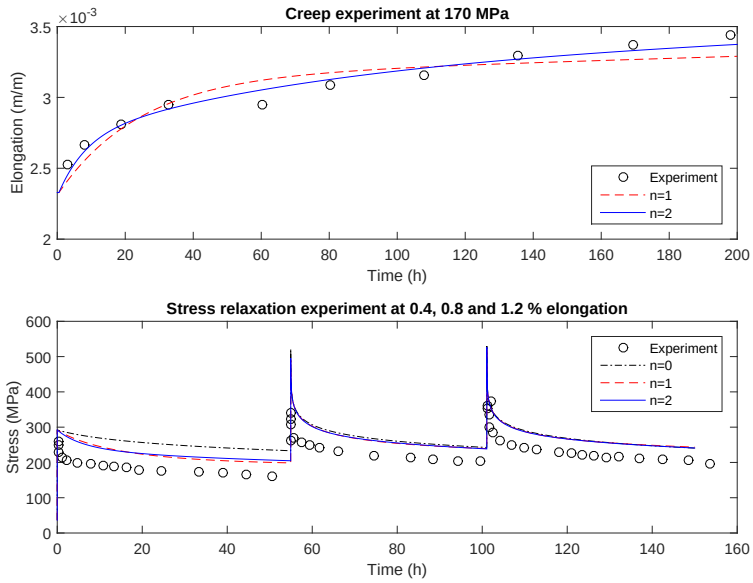

Figure 3.12. Creep and relaxation of CWSR samples. Comparison between the experimental data (circles) and simulations with model with a different number n of Kelvin units. $n = 0$ represents the pure elastic and creep deformation.

ever, later on it has been neglected [9, 51, 52, 70], either implicitly or explicitly, and several experimentally observed cladding transient responses have remained unexplained. In this work a viscoelastic model assuming the separation of the permanent and the anelastic deformations was constructed. The viscoelastic model is able to provide a qualitative interpretation of the observations on the cladding response to transient stresses such as load drops, creep reversal and stress relaxation. In scenarios where a commonly used strain hardening rule is known to work, such as stress increases, the viscoelastic model behaves similarly to strain hardening models. The observed time evolution of the primary creep can be explained by various concurrent processes operating at different time scales and approximated by a series of relaxation processes. The model can be used to simulate various creep experiments performed both in laboratory conditions and in-pile. The model is self-consistent in the sense that the creep and stress relaxation are simulated with the single model, and a model fitted to the results of one type of experiment can in principle used to simulate also other kinds of situations.

The major difference of the model presented in this work to the conventional approach is the separation of the anelastic component from the permanent creep deformation. The anelastic component is modelled with Kelvin units, an approach which is known to be able to model the behaviour of various substances for small deformations. As this limitation is also inherent in the 1D approach for cladding modelling

in engineering level codes, it should not reduce the usability domain of the fuel behaviour codes. The successful replication of the IFA-585 and IFA-699 results by the model (Figs. 3.8 and 3.9) demonstrates the validity of the chosen approach.

Figures 3.11 and 3.12 show that by including Kelvin units the stress relaxation modelling is also improved. While the creep results with the model without anelastic contribution (n = 0) would not represent traditional models, as there is no primary creep contribution, with the stress relaxation it provides the results corresponding to the use of strain hardening rule. Increasing the number of Kelvin units enhances the correspondence between the measurements and the simulation results. This is especially noticeable in the stress relaxation of the R sample in Fig. 3.11. However, the stress relaxation experiments also demonstrate the current shortcomings of the model. The stresses, especially the maximum ones, are generally overestimated. The time evolution of the model, while qualitatively correct, is still somewhat too slow.

The comparison of Figures 3.11 and 3.12 demonstrates that the creep strength of the material also has an effect on whether taking viscoelastic effects into account is necessary. The viscoelastic contribution to creep resistant CWSR specimen is small, and this shows in the stress relaxation experiment. On the other hand, in the soft R specimen the viscoelastic contribution is visible in both the creep and stress relaxation experiments.

3.4.1 Case comparison

When comparing the values for κ_i and τ_i tabulated in Table 3.2, a rough grouping of the samples should be done. Model coefficients were fitted for long-time evolution for the first three experiments, so Delobelle n = 2 τ_2 should be compared to their τ_1s. Correspondingly Delobelle n = 1 κ_1s denotes the anelastic elongation and is compared to the κ_1s of the other experiments. The samples in IFA-699, Matsuo's experiments and Delobelle et al.'s experiments were Zircaloy-4, although the last one featured two different heat treatments. The IFA-585 segment investigated here was Zircaloy-2, which has a heat treatment that hardens it. In effect, Delobelle CWSR and IFA-585 have a hardening treatment whereas rest of the samples do not.

The hardening treatment is obvious in the model coefficients. For time constants, Delobelle CWSR is close to the IFA-585, whereas the Matsuo (and by extension IFA-699) and Delobelle R feature a faster time evolution. Softer material deforms more, as shown by the lower κ_1s of Zircaloy-4 materials. Comparing laboratory and in-pile experiments, the time constants appear similar; however, based on the $\kappa_1 s$ it would appear that the anelastic strain is smaller for in-pile experiments. Causey et al. [54] show that the opposite is true: anelastic strain obtained in-pile should be larger than the strain in laboratory conditions. There are several probable causes for the difference: The experiment of Delobelle et al. was in the axial direction, others measured diameter change in internally pressurized tubes. The coefficients are fitted to general stress in Halden cases and to hoop stress in Matsuo's cases. And, what is more, Halden data was preprocessed to remove the elastic strain, and it may be

that some of the anelastic contribution was also removed in the process.

3.4.2 Validity range for the model

The temperature range investigated was 575–625 K for in-pile and 623–664 K for laboratory experiments, whereas the stress ranged between compressive 78 MPa and tensile 148 MPa in creep experiments. In this range, which corresponds to reactor operating conditions, the model performed well. The stress relaxation experiment featured higher stresses and, as discussed above, indicates that additional models are needed for simulation of high stress and high strain rate scenarios. According to Lucas and Pelloux [9], the strain hardening rule fails at 400 °C (673 K), which they attribute to defect annealing. Was states, on the other hand, that for Zirconium alloys the temperature range between 175–523 °C (448–796 K) is an athermal region where in-reactor creep is independent of temperature (p. 754 of [49]). Causey et al. also note that the proportion of recovered strain fraction in post experiment annealing is similar between the irradiated and non-irradiated samples up to 720 K [54]. At higher temperatures no additional strain is recovered for non-irradiated samples whereas the increased recovery continues to 770 K for irradiated samples.

One explanation for the behaviour reported by Lucas and Pelloux is that they try to fit their observations to strain hardening rule. The temperature increase to 400 °C was the last in the series and, according to the strain hardening rule, the previously accumulated strain would diminish the effect of the change in the conditions. Therefore the anomalous behaviour they reported may have been the result of using a wrong model for interpretation. However, the observed creep behaviour should not be extrapolated to and above 400 °C without further data on transient creep behaviour at those temperatures.

3.4.3 Model uncertainties

The viscoelastic model predictions shown previously have required some case by case adjustments. These adjustments may either be reasonable or the result of a non-physical model. The sources of uncertainty include:

Material properties are influenced by composition and heat treatment, which vary in investigated segments.

Empirical models must be individually tuned for each material.

Missing models especially relating to fast deformation observed in stress relaxation cases.

Simplified models such as describing the thick-walled tube with wall centre properties are commonly used.

As-fabricated condition of the cladding will affect the initial observed primary creep.

Determination of the steady state creep rate contains several uncertainties. The steady state creep model affects the results, especially in the later periods of

the experiments as possible errors accumulate.

Experimental procedures differ across the experiments, and as literature data has been relied on there is no control over the procedures in this work.

In- and ex-pile behaviour may differ both quantitatively and qualitatively.

Several of these are discussed in detail in the following.

3.4.4 Fast deformation

In stress relaxation experiments the maximum stresses are encountered when the strain has reached the target value. They are overestimated by the viscoelastic model as well as the model used by the authors of the original experimental paper [52]. The peak stress given by the model is dominated by the elastic modulus of the material. Delobelle et al. [52] assume the reason is that the experiment reaches the plastic instability region of the sample materials, meaning that during the imposing of the strain the sample plastically deforms. This is probable as the strain rate is high enough to require very fast relaxation processes if the instantaneous plastic deformation is ruled out.

The modelling of especially the R specimen could be improved by using higher n to simulate a larger range of time dependent processes. However, as the data available are just a few points, increasing n would potentially result in overfitting. Also, it should be noted that the current implementation presented in Eqs. (3.15) to (3.17) requires the use of time steps shorter than the smallest τ_i in the stress relaxation simulations. This limits the n to be used in an actual fuel behaviour application.

Further model development would be required for the modelling of fast deformation. Ideally, the model would be based on a comprehensive data set of experimental data on samples used also for creep and stress relaxation experiments.

3.4.5 Behaviour in- and ex-pile

The few correlation based creep models that take anelastic deformation into account also keep the traditional primary creep included in the formulation. Murty and Yoon add an anelastic component to the usual elastic and creep components [53], thus indicating that a part of the transient deformation is due to delayed elasticity. Matsuo proposes hardening surfaces [70] which are effectively similar. In contrast to these, the whole of transient deformation is explained by anelastic component in the model developed in this work. The reason for this difference might be the difference in in- and ex-pile behaviour. Murty investigates cladding creep in out-of-pile experiments and, as shown in Figs. 3.10c and 3.10d, it could be that the in-pile creep differs quantitatively from out-of-pile creep. However, an alternative explanation would be in the initial as manufactured condition of the cladding and different experimental procedures.

In-pile experiments are expensive and the test rigs, once inserted in the reactor, need to be committed for the duration of the reactor cycle. Therefore, the operation of the testing device is ensured prior to the actual experiment. This is achieved with

pre-experiment tests, which include tests at experimental temperatures. According to the strain hardening rule and common understanding of the creep phenomena, if there is no stress the cladding should not strain. However, should the cladding be pre-stressed by the manufacturing processes, this pre-experiment testing period at zero stress would condition the cladding. Such care would not be needed in laboratory experiments, which can be aborted if there is a problem with the test device. Therefore the effect of manufacturing processes could be seen in laboratory experiments.

The work of Garzarolli et al. [56] provides insight into the issue of cladding initial condition. They irradiated several closed end tube samples with different internal pressures at guide tubes of fuel assemblies at commercial reactors. According to their findings, the primary creep is stronger in the tensile direction and actually quite small in compression. This was an in-pile experiment, and, according to the observations from the Halden experiments, the primary creep should be similar in both directions. Interpreted with the viscoelastic model presented in this work, there is one possible explanation: the manufacturing processes condition the cladding to non-zero initial stress conditions, which are seen in laboratory experiments but are annealed out by the pre-experiment testing procedures in Halden. Residual stresses from manufacturing processes have been observed at microscopic level [89], but their macroscopic effects are to be determined.

3.4.6 Steady state creep rate

The selection of the steady state creep model does affect the results obtained. In addition to the uncertainties inherent in the effects of fabrication of different samples, there are several unresolved issues:

The driving force for the creep. Most of the experiments report the cladding hoop stress (e.g. [50, 51, 70]), whereas according to Geelhood [69] using effective stress would yield identical behaviour at compression and tension, and according to Foster and Baranwal [90] the deviatoric component of the hoop stress would be the driving force for the creep.

The effect of differing oxide formation rates. Varying oxide formation rates may affect the measurements as the oxide is less dense than the metal it replaces. This is especially relevant in the Halden experiments where the diameter measurement uses separate reference parts [13, 14]. Contrary to unfuelled IFA-585, the IFA-699 featured segments with fuel pellets that potentially increased the cladding temperature above that of the reference sample.

The effects of irradiation growth in in-pile experiments. In many cladding tubes the irradiation growth both increases the length of the pipes and conserves volume [49, 56]. This leads to a constant rate change in diameter during irradiation, with the rate and direction depending on the cladding texture, cold work and the final heat treatment.

The possible strength differential of Zirconium alloys. There is a strength differential in tensile and compressive directions arising from the hexagonal close packed crystal structure [66]. This strength differential is observed in high stress situation and is attributed to twinning; however, whether it affects the creep behaviour is not clear.

4. Conclusions and future prospects

Nuclear fuel provides the first two safety barriers to prevent the spread of radionuclides: the fuel pellet matrix and the cladding tube. Therefore, using the correct tools to analyze the state of the fuel under irradiation is important. This thesis addressed two topics of fuel behaviour modelling. The first, discussed in Chapter 2, was the treatment of uncertainty and sensitivity in dedicated fuel behaviour codes and the propagation of the results to the other reactor analysis expert codes. The second topic, discussed in Chapter 3, was the modelling of the cladding response to changing stresses.

The focus of the uncertainty and sensitivity analysis was the sensitivity of gap conductance to the uncertainty of the input. It was shown in the Publication [I] that the input interactions yield a meaningful amount of the total resulting uncertainty. This is important as the gap conductance both affects fuel behaviour and varies 10-fold during the rod reactor life. In order to correctly represent these uncertainties stemming from fuel behaviour in other codes a development of fuel module FINIX was initiated. The initial development and first results of implementation to Serpent and TRAB-3D codes were presented in Publication [II].

The uncertainty and sensitivity analysis can be expanded in two directions. The current work consists of an analysis of a steady state code, and the logical extension is a similar work on transient code such as FRAPTRAN-1.5. Not only stand-alone uncertainty and sensitivity analysis should be performed, but also the propagation of the uncertainties from the steady state initialization should be studied. The other direction is methodological, as the variance decomposition method still deals with means and variances. There are situations such as a nearly closed gas gap where the outputs are not neatly represented by such a presentation. The whole concept of propagating uncertainties through the reactor calculation chain requires work as the various fields do not use equivalent methods and models. FINIX development consists of both improvement to internal structures and addition of new models to take account of e.g. ballooning during LOCA scenarios.

The development of the cladding mechanical response model was described in Chapter 3. The deformation under stress was discussed and the relevant processes outlined. Currently in engineering applications correlations fitted to experiments are used in place of more mechanistic models. Most of the cladding creep correlations

use strain hardening rule to take changing conditions into account, and have difficulties in dealing with load drop and reversal situations. In Publication [III] a phenomenological model was constructed to describe cladding transient behaviour. The cladding model was then reformulated using tools of the viscoelastic theory in Publications [IV, V]. The final model is capable of reproducing the observed cladding behaviour in in-pile and laboratory creep experiments as well as the results of the stress relaxation experiment.

Future development of the viscoelastic model include investigation of the cladding as-manufactured state to its initial strain behaviour and inclusion of explicit temperature and irradiation effects to the model. As discussed in Section 3.4 the as-manufactured state may affect the observed primary creep, and therefore explain at least in part the discrepancy between in-pile and laboratory experiments. In order for the model to be implemented in a fuel behaviour code the effect of temperature needs to be accounted for. This may prove challenging as the temperature effect has been assumed to follow the strain hardening rule and as a consequence few experiments with changing temperature have been published. The effect of the irradiation should also be included by an addition of an explicit fast flux term to the model. This would require experimental data of cladding behaviour under wide variety of neutron fluxes.

The viscoelastic model has been developed based on published experimental data. The experiments investigated samples with different compositions and heat treatments, and were based on the premise of strain hardening transient behaviour. Therefore, a focused experimental campaign designed based on the understanding accumulated in this work would provide essential information on transient behaviour of Zirconium alloys.

Bibliography

[1] W. Wiesenack, T. Tverberg, M. McGrath, E. Kolstad, and S. Beguin, "Rod overpressure/lift-off testing at halden in-pile data and analysis," *Journal of Nuclear Science and Technology*, vol. 43, pp. 1037–1044, 2006.

[2] OECD/NEA, "Nuclear fuel behaviour under reactivity-initiated accident (RIA) conditions state-of-the-art report," tech. rep., 2010.

[3] OECD/NEA, "Nuclear fuel behaviour in loss-of-coolant accident (LOCA) conditions," tech. rep., 2009.

[4] H. Glaeser, "GRS method for uncertainty and sensitivity evaluation of code results and applications," *Science and Technology of Nuclear Installations*, vol. 2008, p. 798901, 2008.

[5] M. Ionescu-Bujor and D. Cacuci, "A comparative review of sensitivity and uncertainty analysis of large-scale systems – II: Statistical methods," *Nuclear Science and Engineering*, vol. 147, pp. 204–217, 2004.

[6] T. Blyth, M. Avramova, K. Ivanov, E. Royer, E. Sartori, and O. Cabellos, "Benchmark of uncertainty analysis in modeling (UAM) for design, operation and safety analysis of LWRs, volume ii: Specification and support data for the core cases (phase ii) [draft version 1.0]. Technical Report NEA/NSC/DOC(2012)?," *Nuclear Energy Agency*, 2012.

[7] B. Cox, "Pellet-clad interaction (PCI) failures of zirconium alloy fuel cladding a review," *Journal of Nuclear Materials*, vol. 172, pp. 249–292, 1990.

[8] F. Nabarro and F. de Villiers, *Physics Of Creep And Creep-Resistant Alloys*. CRC Press, 1995.

[9] G. Lucas and R. Pelloux, "Some observations on time-hardening and strain-hardening rules for creep in Zircaloy-2," *Nuclear Technology*, vol. 53, pp. 46–57, 1981.

[10] A. Donaldson, "In-reactor creep behaviour of zircaloy under variable loading conditions in IFA-585," *HWR-413*, 1994.

[11] M. McGrath, “In-reactor creep behaviour of Zircaloy-2 under variable loading conditions in IFA-585,” *HWR-471*, 1996.

[12] M. McGrath, “In-reactor creep behaviour of zircaloy cladding,” *Proceedings of the 2000 International Topical Meeting on LWR Fuel Performance*, 2000.

[13] J. Foster and M. McGrath, “In-reactor creep behavior of zircaloy-2,” *Proceedings of the 2007 LWR Fuel Performance Meeting*, 2007.

[14] S. Hanawa, “In-reactor creep behaviour of LWR fuel claddings: Initial results from IFA-699,” *HWR-882*, 2008.

[15] K. Geelhood, W. Luscher, and C. Beyer, “FRAPCON-3.4: A computer code for the calculation of steady-state thermal-mechanical behavior of oxide fuel rods for high burnup,” *NUREG/CR-7022, Vol.1*, 2011.

[16] K. Geelhood, W. Luscher, C. Beyer, and J. Cuta, “FRAPTRAN 1.4: A computer code for the transient analysis of oxide fuel rods,” Tech. Rep. NUREG-CR-7023, Vol. 1, Pacific Northwest National Laboratory, 2011.

[17] K. Geelhood, W. Luscher, and C. Beyer, “FRAPTRAN 1.4: Integral assessment,” Tech. Rep. NUREG-CR-7023, Vol. 2, Pacific Northwest National Laboratory, 2011.

[18] A. Moal, V. Georgenthum, and O. Marchand, “SCANAIR a transient fuel performance code part one: General modelling description,” *Nuclear Engineering and Design*, vol. 280, pp. 150–171, 2014.

[19] V. Georgenthum, A. Moal, and O. Marchand, “SCANAIR a transient fuel performance code part two: Assessment of modelling capabilities,” *Nuclear Engineering and Design*, vol. 280, pp. 172–180, 2014.

[20] P. Van Uffelen, C. Györi, A. Schubert, J. van de Laar, Z. Hozer, and G. Spykman, “Extending the application range of a fuel performance code from normal operating to design basis accident conditions,” *Journal of Nuclear Materials*, vol. 383, pp. 137–143, 2008.

[21] A. Hämäläinen, J.-O. Stengård, J. Miettinen, R. Kyrki-Rajamäki, and K. Valtonen, “Coupled code FRAPTRAN-GENFLO for analysing fuel behaviour during PWR and BWR transients and accidents,” in *IAEA Technical Committee Meeting on Fuel Behavior under Transient and LOCA Conditions (IAEA-TECDOC-1320). Halden, Norway 10-14 September 2001.*, p. 43, 2001.

[22] T. Viitanen and V. Tulkki, “Combining reactor physics and fuel performance calculations,” in *Top Fuel Reactor Fuel Performance 2012 Transactions. Manchester, United Kingdom, 2–6 September*, pp. 695–701, 2012.

[23] G. Rossiter, “Development of the ENIGMA fuel performance code for whole core analysis and dry storage assessments,” *Nuclear Engineering and Technology*, vol. 43, pp. 489–498, 2011.

[24] L. Holt, U. Rohde, M. Seidl, A. Schubert, P. Van Uffelen, and R. Macian-Juan, "Two-way coupling between the reactor dynamics code DYN3D and the fuel performance code TRANSURANUS at assembly level," in *Proceedings of the 2014 22nd International Conference on Nuclear Engineering ICONE22 July 7-11, 2014, Prague, Czech Republic*, pp. ICONE22–30812, 2014.

[25] V. Bergeaud and M. Tajchman, "Application of the SALOME software architecture to nuclear reactor research," in *Springsim '07 Proceedings of the 2007 spring simulation multiconference*, pp. 383–387.

[26] D. Gastona, C. Newmana, G. Hansena, and D. Lebrun-Grandié, "MOOSE: A parallel computational framework for coupled systems of nonlinear equations," *Nuclear Engineering and Design*, vol. 239, pp. 17968–1778, 2009.

[27] U. Rohde, "The modeling of fuel rod behaviour under RIA conditions in the code DYN3D," *Annals of Nuclear Energy*, vol. 28, p. 1343, 2001.

[28] ISL Inc., "RELAP5/MOD3.3 code manual volume i: Code structure, system models, and solution methods," Tech. Rep. NUREG-CR-5535 Rev 4, Vol. 1, Information Systems Laboratories, Inc., 2010.

[29] T. Ikonen, "FINIX fuel behavior model and interface for multiphysics applications. Code documentation for version 0.13.9," Tech. Rep. VTT-R-06563-13, VTT Technical Research Centre of Finland, 2013.

[30] H. Loukusa, "Validation of the FINIX fuel behavior code version 0.13.9," Tech. Rep. VTT-R-06565-13, VTT Technical Research Centre of Finland, 2013.

[31] J. Leppänen, *Development of a New Monte Carlo Reactor Physics Code*. PhD thesis, Helsinki University of Technology, 2007.

[32] M. Rajamäki, "TRAB, a transient analysis program for BWR," Tech. Rep. 24, Technical Research Centre of Finland, Nuclear Engineering Laboratory, 1976.

[33] E. Kaloinen and R. Kyrki-Rajamäki, "TRAB-3D, a new code for three-dimensional reactor dynamics," in *CD-ROM Proceedings of ICONE-5, 5th International Conference on Nuclear Engineering. Nuclear Advances through Global Cooperation*, (Nice, France), May 26-30 1997.

[34] R. Kyrki-Rajamaki, "Three-dimensional reactor dynamics code for vver type nuclear reactors.," Tech. Rep. 246, DrTech thesis. Technical Research Centre of Finland, 1995.

[35] STUK, "Ydinvoimalaitoksen deterministiset turvallisuusanalyysit." Ohje YVL B.3 / 15.11.2013.

[36] N. Gutierrez, A. Lingenfelter, R. Rand, and G. Potts, "Statistical methodology for fuel rods thermal-mechanical design and licensing analysis," *Transactions of TopFuel 2006, Int. meeting on LWR fuel performance*, pp. 235–239, 2006.

[37] T. Ozawa and T. Abe, “Development of probabilistic design method for fast reactor fuel rod,” *Nuclear Science and Engineering*, vol. 152, pp. 37–47, 2006.

[38] V. I. Arimescu, “Best-estimate BWR thermal-mechanical analysis based on nonparametric order statistics,” *Proc. Water reactor fuel performance meeting 2008, paper 8094*, 2008.

[39] G. Sauer and W. Besemböck, “Reliable statistical fuel rod analysis,” *Proc. Water reactor fuel performance meeting 2008, paper 8031*, 2008.

[40] A. Wensauer and I. Distler, “Application of probabilistic methods to fuel rod design evaluation,” in *Proc. Techn. Com. Meeting IAEA, 2326 Nov. 2009, Villingen, Switzerland, IAEA-TECDOC-1654*, pp. 65–74, 2009.

[41] A. Bouloré, C. Struzik, and F. Gaudier, “Uncertainty and sensitivity analysis or the nuclear fuel thermal behavior,” *Nuclear Engineering and Design*, vol. 253, pp. 200–210, 2012.

[42] A. Arkoma, M. Hänninen, K. Rantamäki, J. Kurki, and A. Hämäläinen, “Statistical analysis of fuel failures in large break loss-of-coolant accident (LBLOCA) in EPR type nuclear power plant,” *Nuclear Engineering and Design*, vol. 285, pp. 1–14, 2015.

[43] OECD/NEA, “BEMUSE phase V report, uncertainty and sensitivity analysis of a LB-LOCA in ZION nuclear power plant,” *NEA/CSNI/R(2009)13*, 2009.

[44] P.H. Kvam and B. Vidakovic, “Nonparametric statistics with applications to science and engineering,” *John Wiley & Sons*, 2007.

[45] I. Sobol’, “Sensitivity analysis for non-linear mathematical models,” *Mathematical modelling and computational experiment*, vol. 1, pp. 407–414, 1993.

[46] K. Geelhood, W. Luscher, C. Beyer, D. Senor, M. Cunningham, D. Lanning, and H. Adkins, “Predictive bias and sensitivity in NRC fuel performance codes,” *NUREG/CR-7001*, 2009.

[47] K. Linga Murty and I. Charit, “Texture development and anisotropic deformation of zircaloys,” *Nuclear Energy*, vol. 48, pp. 325–359, 2006.

[48] A. Nowick and B. Berry, *Anelastic relaxation in crystalline solids*. New York: Academic Press, 1972.

[49] G. Was, *Fundamentals of Radiation Materials Science: Metals and Alloys*. Springer, 2007.

[50] Y. Matsuo, “Thermal creep of Zircaloy-4 cladding under internal pressure,” *Journal of Nuclear Science and Technology*, vol. 24, no. 2, pp. 111–119, 1987.

[51] M. Limback and T. Andersson, “A model for analysis of the effect of final annealing on the in- and out-of-reactor creep behavior of zircaloy cladding,” *ASTM STP*, vol. 1295, pp. 448–468, 1996.

[52] P. Delobelle, P. Robinet, P. Geyer, and P. Bouffioux, “A model to describe the anisotropic viscoplastic behaviour of Zircaloy-4 tubes,” *Journal of Nuclear Materials*, vol. 238, pp. 135–162, 1996.

[53] K. Murty and K. Yoon, “Prediction of creep transients in zircaloy fuel cladding using anelastic strain model,” *Transactions of the 5th International Conference on Structural Mechanics in Reactor Technology (SMiRT-5)*, vol. C3/6, 1979.

[54] A. Causey, F. Butcher, and S. Donohue, “Measurement of irradiation creep of zirconium alloys using stress relaxation,” *Journal of Nuclear Materials*, vol. 159, pp. 101–113, 1988.

[55] D. Franklin, G. Lucas, and A. Bement, “Creep of zirconium alloys in nuclear reactors,” *ASTM STP*, vol. 815, 1983.

[56] F. Garzarolli, H. Stehle, and E. Steinberg, “Behavior and properties of zircaloys in power reactors: A short review of pertinent aspects in LWR fuel,” *ASTM STP*, vol. 1295, pp. 12–32, 1996.

[57] Y. S. Kim, “Generalized creep model of Zircaloy-4 cladding tubes,” *Journal of Nuclear Materials*, vol. 250, pp. 164–170, 1997.

[58] I. Schaffler, P. Geyer, P. Bouffioux, and P. Delobelle, “Thermomechanical behavior and modelling between 350c and 400c of Zircaloy-4 cladding tubes from an unirradiated state to high fluence (0 to 85 1024 nm.2, e > 1 mev,” *Transactions of the ASME*, vol. 122, pp. 168–176, 2000.

[59] A. Soniak, N. L’Hullier, J.-P. Mardon, V. Rebeyrolle, P. Bouffioux, and C. Bernaudat, “Irradiation creep behavior of Zr-base alloys,” *ASTM STP*, vol. 1423, pp. 837–862, 2002.

[60] C. Nam, B.-K. Choi, M.-H. Lee, and Y.-H. Jeong, “Creep strength of Zircaloy-4 cladding depending on applied stress and annealing temperature,” *Journal of Nuclear Materials*, vol. 305, pp. 70–76, 2002.

[61] K. Ito, K. Kamimura, and Y. Tsukuda, “Evaluation of irradiation effect on spent fuel cladding creep properties,” *Proceedings of the 2004 International Meeting on LWR Fuel Performance*, pp. 440–451, 2004.

[62] M. Griffiths, N. Christodoulou, and S. Donohue, “Damage dependence of irradiation deformation of Zr-2.5Nb pressure tubes,” *ASTM STP*, vol. 1467, p. 686, 2005.

[63] J. Moon, P. Cantonwine, K. Anderson, S. Karthikeyan, and M. Mills, “Characterization and modeling of creep mechanisms in Zircaloy-4,” *Journal of Nuclear Materials*, vol. 353, pp. 177–189, 2006.

[64] R. Holt, "In-reactor deformation of cold-worked Zr-2.5Nb pressure tubes," *Journal of Nuclear Materials*, vol. 372, pp. 182–214, 2008.

[65] H. Wang, Z. Hu, W. Lu, and M. Thouless, "A mechanism-based framework for the numerical analysis of creep in Zircaloy-4," *Journal of Nuclear Materials*, vol. 433, pp. 188–198, 2013.

[66] J. Zhan, X. Gao, J. Sobotka, B. Webler, and B. Cockeram, "Modeling the tension-compression asymmetric yield behavior of β-treated Zircaloy-4," *Journal of Nuclear Materials*, vol. 451, pp. 292–299, 2014.

[67] M. Blanter, I. Golovin, H. Neuhäuser, and H. Sinning, *Internal Friction in Metallic Materials: A Handbook*. Springer, 2007.

[68] K. Geelhood, "Recent updates to NRC fuel performance codes and plans for future improvements," *Nuclear Engineering and Technology*, vol. 43, pp. 509–522, 2011.

[69] W. Luscher and K. Geelhood, "Material property correlations: Comparisons between FRAPCON-3.4, FRAPTRAN 1.4 and MATPRO," *NUREG/CR-7024*, 2011.

[70] Y. Matsuo, "Creep behaviour of zircaloy cladding under variable conditions," *ASTM STP*, vol. 1023, pp. 678–691, 1989.

[71] "IFPE database NEA IFPE/IFA-585 experimental data," . last modified 13-MAR-2008.

[72] D. Fraser, P. Ross-Ross, and A. Causey, "The relation between stress-relaxation and creep for some zirconium alloys during neutron irradiation," *Journal of Nuclear Materials*, vol. 46, pp. 281–292, 1973.

[73] Y. Long, C. Beard, S. Henk, and G. Zhou, "ZIRLO high performance fuel cladding material high stress creep model," *Proceedings of 2010 LWR Fuel Performance Meeting*, p. Paper 054, 2010.

[74] G. Zhou, L. Hallstadius, G. Wikmark, Y. Long, and J. Foster, "Evaluation and modeling of in-reactor creep and stress-relaxation tests of ZIRLO fuel cladding under wide stress conditions," *Proceedings of 2011 Water Reactor Fuel Performance Meeting*, pp. Paper T2–038, 2011.

[75] R. Kapoor, S. Wadekar, and J. Chakravartty, "Deformation in Zr-1Nb-1Sn-0.1Fe using stress relaxation technique," *Materials Science and Engineering A*, vol. 328, pp. 324–333, 2002.

[76] L. Jernkvist, "A model for inelastic deformation of irradiated Zirconium alloy cladding under transient conditions," *Transactions of the 15th International Conference on Structural Mechanics in Reactor Technology (SMiRT-15)*, vol. C04/3, pp. 477–484, 1999.

[77] M. Rautenberg, D. Poquillon, P. Pilvin, C. Grosjean, J. Cloue, and X. Feaugas, “Thermal isocreep curves obtained during multi-axial creep tests on recrystallized Zircaloy-4 and M5 alloy,” *Nuclear Engineering and Design*, vol. 269, pp. 33–37, 2014.

[78] D. Gutierrez-Lemini, *Engineering Viscoelasticity*. Springer, 2014.

[79] R. Kohlrausch *Pogg. Ann. Phys. Chem.*, vol. 91, p. 179, 1854.

[80] R. Anderssen, S. Husain, and R. Loy, “The kolrausch function: properties and applications,” *Anziam Journal*, vol. 45, pp. C800–C816, 2004.

[81] R. S. Anderssen, M. P. Edwards, S. A. Husain, and R. J. Loy, “Sums of exponentials approximations for the kohlrausch function,” *19th International Congress on Modelling and Simulation*, pp. 263–269, 2011.

[82] H. Banks, S. Hu, and Z. Kenz, “A brief review of elasticity and viscoelasticity for solids,” *Advances in Applied Mathematics and Mechanics*, vol. 3, no. 1, pp. 1–51, 2011.

[83] R. Kozar, A. Jaworski, T. Webb, and R. Smith, “In situ monitored in-pile creep testing of zirconium alloys,” *Journal of Nuclear Materials*, vol. 444, pp. 14–22, 2014.

[84] D. Harries, “Irradiation creep in non-fissile metals and alloys,” *Journal of Nuclear Materials*, vol. 65, pp. 157–173, 1977.

[85] T. Hayes, M. Kassner, and R. Rosen, “Steady-state creep of a-zirconium at temperatures up to 850 c,” *Metallurgical and Materials Transactions A*, vol. 33A, pp. 337–343, 2002.

[86] T. Hayes and M. Kassner, “Creep of zirconium and zirconium alloys,” *Metallurgical and Materials Transactions A*, vol. 37 A, pp. 2389–2396, 2006.

[87] J. Kättö, “Corrosion and its modeling in nuclear reactor fuel cladding,” 2013. M.Sc thesis, Aalto University School of Engineering, 80 pages.

[88] F. Povolo and B. Molinas, “High-temperature internal friction in polycrystalline zirconium and Zircaloy-4,” *Journal of Nuclear Materials*, vol. 114, pp. 85–94, 1983.

[89] D. Gloaguen, T. Berchi, E. Firard, and R. Guillen, “Measurement and prediction of residual stresses and crystallographic texture development in rolled zircaloy-4 plates: X-ray diffraction and the self-consistent model,” *Acta Materialia*, vol. 55, pp. 4369–4379, 2007.

[90] J. Foster and R. Baranwal, “ZIRLOTM irradiation creep stress dependence in compression and tension,” *16th ASTM Zirconium Symposium*, 2010.

PUBLICATION I

The importance of input interactions in the uncertainty and sensitivity analysis of nuclear fuel behavior

Nuclear Engineering and Design, **275**, 229–241.

Nuclear Engineering and Design 275 (2014) 229–241

Contents lists available at ScienceDirect

Nuclear Engineering and Design

journal homepage: www.elsevier.com/locate/nucengdes

The importance of input interactions in the uncertainty and sensitivity analysis of nuclear fuel behavior

T. Ikonen*, V. Tulkki

VTT Technical Research Centre of Finland, P.O. Box 1000, FI-02044 VTT, Finland

HIGHLIGHTS

- Uncertainty and sensitivity analysis of modeled nuclear fuel behavior is performed.
- Burnup dependency of the uncertainties and sensitivities is characterized.
- Input interactions significantly increase output uncertainties for irradiated fuel.
- Identification of uncertainty sources is greatly improved with higher order methods.
- Results stress the importance of using methods that take interactions into account.

ARTICLE INFO

Article history:
Received 13 June 2013
Received in revised form 5 May 2014
Accepted 16 May 2014

ABSTRACT

The propagation of uncertainties in a PWR fuel rod under steady-state irradiation is analyzed by computational means. A hypothetical steady-state scenario of the Three Mile Island 1 reactor fuel rod is modeled with the fuel performance FRAPCON, using realistic input uncertainties for the fabrication and model parameters, boundary conditions and material properties. The uncertainty and sensitivity analysis is performed by extensive Monte Carlo sampling of the inputs' probability distribution and by applying correlation coefficient and Sobol' variance decomposition analyses. The latter includes evaluation of the second order and total effect sensitivity indices, allowing the study of interactions between input variables. The results show that the interactions play a large role in the propagation of uncertainties, and first order methods such as the correlation coefficient analyses are in general insufficient for sensitivity analysis of the fuel rod. Significant improvement over the first order methods can be achieved by using higher order methods. The results also show that both the magnitude of the uncertainties and their propagation depends not only on the output in question, but also on burnup. The latter is due to onset of new phenomena (such as the fission gas release) and the gradual closure of the pellet-cladding gap with increasing burnup. Increasing burnup also affects the importance of input interactions. Interaction effects are typically highest in the moderate burnup (of the order of 10–40 MWd/kgU) regime, which covers a large portion of the operating regime of typical nuclear power plants. The results highlight the importance of using appropriate methods that can account for input interactions in the sensitivity analysis of the fuel rod behavior.

1. Introduction

The nuclear fuel rod of a light-water reactor consists of an oxide fuel pellet stack enclosed inside a metallic cladding tube. The pellet stack is held in place by a spring and the rod is pressurized with heat-conducting gas, facilitating heat transfer across the gap between the pellets and the cladding. Analysis of the fuel rod's behavior under irradiation in a nuclear reactor involves solving the transfer of heat from the pellet into the surrounding coolant through the gap and the cladding, the mechanical response of the pellet and the cladding to thermal and mechanical stresses, the irradiation-induced changes in materials, and the release of gaseous fission products into the gas gap. All the phenomena are interconnected, constituting an extremely complex system with rich behavior in different operating regimes and strong dependency on burnup (Bailly et al., 1999; Cacuci, 2010).

The system can be modeled numerically with dedicated fuel performance codes, which traditionally focus either on the steady

* Corresponding author. Tel.: +358 40 659 2130; fax: +358 20 722 5000.
E-mail address: timo.ikonen@vtt.fi (T. Ikonen).

http://dx.doi.org/10.1016/j.nucengdes.2014.05.015
0029-5493/

state irradiation or the simulation of transient scenarios. In both cases, one of the main purposes of numerical modeling is to provide understanding on how the individual phenomena interact and create the overall response of the rod to external conditions. An important aspect of such a study is the acquisition of detailed data that can be used to ensure that the rod performs within the safety and regulatory guidelines, and also to guide in revising the safety regulations (Rashid et al., 2011).

There are several sources of uncertainty in fuel performance analysis. The rod's fabrication parameters, experimentally determined material properties and system parameters are never precise, but introduce various amounts of uncertainties into the system. These are propagated to model outputs such as the fuel centerline temperature, internal pressure and gap conductance. To ensure safe operation of the fuel rod, these uncertainties must be taken into account, either by conservative analysis or best estimate analysis accompanied by evaluation of the related uncertainties. In best estimate analysis quantifying both the magnitude and the source of the output uncertainties is necessary. The latter involves determining the contribution of the uncertainty of each model input to the overall output uncertainty, and is called sensitivity analysis.

Sensitivity analysis in nuclear engineering has recently concentrated mostly on the reactor physics and neutronics and, on the other hand, on thermal hydraulic modeling. Sensitivity analysis of the fuel behavior models has received considerably less attention, although it is known that uncertainties related to fuel modeling can be significant and may also have broader impact on the thermal hydraulics and neutronics modeling (Christensen et al., 1981; Wilderman and Was, 1984; Syrjälahti, 2006; Boulore et al., 2012). In addition, most studies focus on the direct (first-order) effects of the input on the model output. A common approach is to evaluate, *e.g.*, the Spearman correlation coefficients or the first-order Sobol' indices from the model output (Boulore et al., 2012; Glaeser, 2008), which neglect the higher order interactions between the input variables. However, for a complex system such as the fuel rod (Rashid et al., 2011), these interactions can play a major role in the overall output uncertainties, and should not be neglected *a priori* (Saltelli et al., 2008).

In this paper, we investigate the role of input interactions in the uncertainty and sensitivity analysis of the nuclear fuel rod. For this purpose, we use the FRAPCON fuel performance code (Geelhood et al., 2011a,b) and perform statistical analysis of the code's output by evaluating both the conventionally used Spearman correlation coefficients (Draper and Smith, 1998; Kvam and Vidakovic, 2007) and the Sobol' sensitivity indices (Saltelli et al., 2008; Sobol', 1993). We consider a steady state scenario, and focus on identifying the major sources of uncertainties, characterizing interactions between inputs and their dependencies on burnup. Since the initial states of transient calculations with non-fresh fuel are usually generated by such steady state simulations, our results have direct relevance for transient analyses also.

The structure of the paper is as follows. In Section 2, we discuss the fuel performance code FRAPCON-3.4 used in the analysis of the scenario, and in Section 3 we describe the statistical analysis methods. The specifications of the modeled scenario and the input uncertainties are given in Section 4. In Section 5, we first show the best estimate plus uncertainty results of the scenario. Then, we illustrate how the data can be analyzed with the conventional methods and show that such an analysis remains incomplete in most cases. In Section 5.4, we repeat the analysis using the Sobol' variance decomposition method. We show that the variance decomposition analysis gives a consistent and much more complete picture of the system's response to the input uncertainties. According to the analysis, the shortcomings of the Spearman correlation method are due to non-additive interactions between the input variables. These produce uncertainties, whose source can be identified only with higher order methods such as the variance decomposition. We also compare the quantitative effectiveness of the variance decomposition to the Spearman correlation method, showing significant improvement. Using the evaluated total effects, we rank the input uncertainties with respect to their overall importance. We summarize the results of the paper in Section 6.

2. The fuel performance code FRAPCON

The fuel performance model used in this study is the FRAPCON-3.4 code that is maintained by the Pacific Northwest National Laboratory (Geelhood et al., 2011a,b). FRAPCON is a deterministic fuel performance code that calculates the steady-state response of light-water reactor fuel rods during long-term burn-up. Boundary conditions such as the power history and the coolant properties, in addition to the rod fabrication parameters, are supplied as input. The output of the code comprises several observables, including the fuel and cladding temperature distributions in the radial and axial directions, mechanical deformations of the pellet and the cladding, internal pressure, gap conductance, and so on. The physical phenomena described in the code include heat conduction through the fuel, gap and cladding into the coolant, fuel densification and swelling, cladding elastic and plastic deformations, fission gas release and cladding oxidation. The thermal and mechanical solutions are strongly coupled through the gap conductance, which is a function of, for example, pellet and cladding dimensions, and has a strong influence on the radial heat conduction. In addition to the gap conductance, the different submodels become interconnected via phenomena such as the fission gas release, which influences both the thermal and mechanical solutions through gap conductance and pressure and is itself affected by the fuel temperature.

The strong coupling between the different phenomena imply that the model is highly nonlinear and interactions between input variables are very likely. To analyze the output of such a model, we use the statistical methods described in Section 3, which involve Monte Carlo sampling of the input variables from given probability distributions. As FRAPCON is a deterministic code (one input producing exactly one deterministic solution), the sampling of input variables has to be done by external means. For this purpose we have developed a Python script that performs the sampling using methods discussed in Section 3 and generates the FRAPCON input files (Ikonen, 2012). The code is then run and the results post-processed on a Linux cluster.

3. Statistical analysis methods

3.1. General considerations

A fuel performance code is typically very complex, with dozens of input variables and several output observables of interest. In the analysis of such a complex system, determining the propagation of uncertainties from input to output can be a delicate task. Numerous alternative methods of uncertainty and sensitivity analysis exist, each having their advantages and disadvantages. Two ways to group different methods is to distinguish between deterministic and statistical methods, and local and global sensitivity analysis (Saltelli et al., 2008; Ionescu-Bujor and Cacuci, 2004; Cacuci and Ionescu-Bujor, 2004).

With deterministic methods, one estimates the response of the model output to the changes in the value of an input variable either by analytical means, or by deterministic sampling of individual values. With statistical methods, on the other hand, one samples the values of the input variables from a distribution and calculates the

response (output) of the model for each sampled value. The distribution of the output can then be analyzed with various statistical methods. Most of the deterministic methods are also local, meaning that the sensitivity of the output is measured in the neighborhood of a single point in the input variable space, typically varying only one variable at a time. With global sensitivity analysis one varies all the input variables at once, solving the model for each sampled combination of the variables.

For the purposes of this study, analytical and deterministic methods seem impractical. This is both due to the mathematical complexity of the system that is being studied, and the amount of labor that would be necessary in implementing analytical methods into a fuel performance code. However, since the code is very fast computationally (taking only a few seconds per model evaluation), evaluating the uncertainties and sensitivities by statistical sampling is efficient. In addition, we focus on global instead of local analysis methods, because they are better suited for describing the interactions between different input variables (Saltelli and Annoni, 2010). Specifically, the analysis is done using the Spearman correlation coefficients (Draper and Smith, 1998; Kvam and Vidakovic, 2007) and Sobol' variance decomposition (Sobol', 1993; Saltelli, 2002; Glen and Isaacs, 2012). The former represents a more standard method of sensitivity analysis in the nuclear engineering field, while the latter is a more advanced method that has recently asserted itself among practitioners of sensitivity analysis (see, *e.g.* Saltelli et al., 2010 and references therein).

Before describing the methods in detail, we start by defining the problem and the associated notations.

3.2. Preliminaries and problem definition

A model of a complex system can be represented as a mapping $Y = f(\mathbf{X})$, where Y is the output and $\mathbf{X} = [X_1, X_2, \ldots, X_{k-1}, X_k]$ is the vector of k input variables. Without any loss of generality, we may restrict our discussion to the case of a single output, Y. The uncertain value of each variable X_i is characterized by a probability distribution $\mathcal{P}_i(X_i)$, from which one can obtain the mean μ_i and the variance σ_i^2 of X_i. Here, we only consider distributions with finite μ_i and σ_i^2. In principle, the elements of $\mathbf{X}$ can be correlated, but in this work we consider the inputs of a fuel performance code uncorrelated. Hence, we will restrict our analysis to the case where the elements of $\mathbf{X}$ are independent.

In addition to determining the uncertainty in Y that arises from the uncertainty of $\mathbf{X}$, we wish to establish how the uncertainty of each variable X_i contributes to the uncertainty of Y. *Specifically, our goal is to find the proportion of the uncertainty (variance) of Y that is explained by the uncertainty (variance) of* X_i. Moreover, we wish to look at interactions, that is, the effect of changing more than one variable simultaneously. To do this, we first need to make a few formal definitions.

First, let us quantify the effect of changing just one variable, X_i. The linearized response in Y to the change in X_i is given by the partial derivative $\frac{\partial Y}{\partial X_i}$. However, the derivative alone does not take into account the uncertainty of different input variables: if the functional form of f is the same for X_i and X_j, the derivative will be the same regardless of the magnitude of σ_i or σ_j. However, the variable with the larger variance will cause a larger uncertainty in the output. Therefore, it is more practical to consider as a sensitivity measure the standard-deviation-normalized derivative

$$r_i^{\mathrm{lin}} = \frac{\sigma_i}{\sigma_Y}\frac{\partial Y}{\partial X_i}. \tag{1}$$

Here σ_Y denotes to standard deviation of Y and the superscript 'lin' in r_i^{lin} implies that this is a linearized sensitivity measure.

In practice, the derivative in Eq. (1) is evaluated numerically from a sample of size N by fitting. For linear regression, it can be shown that the least-squares-estimated angular coefficient $\hat{b}$ is related to the covariance $\mathrm{cov}(X_i, Y)$ of the variables X_i and Y as follows (Draper and Smith, 1998)

$$\frac{\sigma_i}{\sigma_Y}\hat{b} = \frac{\mathrm{cov}(X_i, Y)}{\sigma_i \sigma_Y} \equiv R_i. \tag{2}$$

The quantity R_i is the Pearson correlation coefficient. For a linear model, R_i is the statistical equivalent of the normalized derivative of Eq. (1). In addition, it can be shown that the square of R_i can be written as the ratio of the variance of the regression-fitted values and the variance of the original data (Draper and Smith, 1998). Thus, R_i^2 is the proportion of *variance explained* by a linear function of X_i.

As a sensitivity measure, R_i^2 is very limited. It can give a complete description of the propagation of uncertainties from $\mathbf{X}$ to Y only for a *linear* and *additive* systems. (A system is linear, if the function f is linear, and additive, if f can be written as a sum in which each term only depends on one variable X_i.) In such case, the sum $\sum_i^k R_i^2 = 1$. However, if the system is nonlinear or non-additive, a linear sensitivity measure can explain only part of the uncertainty of Y, so that $\sum_i^k R_i^2 < 1$. For this reason, improved sensitivity measures are needed to analyze nonlinear models.

3.3. Spearman correlation coefficients

A widely used extension of the Pearson R_i to nonlinear monotonic functions is the Spearman rank correlation coefficient ρ_i (Draper and Smith, 1998; Kvam and Vidakovic, 2007). The corresponding sensitivity measure ρ_i^2 has been widely used to classify correlations in data, also in nuclear engineering. It is also one of the GRS recommended methods of uncertainty and sensitivity analysis (Glaeser, 2008).

Mathematically, the Spearman ρ_i is a linear correlation calculated for ranks, not the data itself. To obtain the ranks x_i and y, the realizations of the variables X_i and Y are arranged into ascending order and assigned values from 1 to N. The correlation coefficient ρ_i is then calculated as (Kvam and Vidakovic, 2007)

$$\rho_i = \frac{\mathrm{cov}(x_i, y)}{\sigma_{x_i}\sigma_y}. \tag{3}$$

The rank correlation coefficient ρ_i can be used in the same manner as the Pearson R_i to obtain the sensitivity of the output Y to the input variables X_i, with ρ_i^2 giving an estimate of the contribution of the ith variable to the variance of Y. On nonlinear systems, the rank correlation method performs considerably better than the linear regression method. However, due to its construction, its ability to describe non-monotonic or non-additive models is limited (Sallaberry and Helton, 2006). For instance, for the simplest possible non-additive function $Y = f(X_1, X_2) = X_1 X_2$, with X_1 and X_2 normal and $\mu_1 = \mu_2 = 0$, one has the correlation coefficients $\rho_1 = \rho_2 = 0$, leaving all of the model's variance unexplained. In a fuel performance code, where such interactions between different input variables are important, the rank correlation coefficient may be an inadequate descriptor of the system. Therefore, more advanced methods need to be considered to study the effect of variable interactions.

3.4. Sobol' variance decomposition

3.4.1. Definition of the sensitivity indices

The variance decomposition method was first proposed by Sobol' (Sobol', 1993). The idea is to express the variance $V(Y)$ of the output as a finite sum, where each term corresponds to the

contribution of one input variable X_i or to the interaction of several input variables. The variance of Y is written as

$$V(Y) = \sum_{i}^{k} V_i + \sum_{i}^{k}\sum_{j>i}^{k} V_{ij} + \cdots + V_{12\ldots k}. \quad (4)$$

Here, V_i is the *first order effect* on the variance $V(Y)$ due to the variable X_i, V_{ij} the *second order effect* due to the interaction of X_i and X_j, and so on, up to $V_{12\ldots k}$, which is the kth order effect due to the interaction of all k input variables. Dividing both sides of Eq. (4) by $V(Y)$ gives

$$\sum_{i}^{k} S_i + \sum_{i}^{k}\sum_{j>i}^{k} S_{ij} + \cdots + S_{12\ldots k} = 1, \quad (5)$$

where $S_i \equiv V_i/V(Y)$ is the *first order sensitivity index*, $S_{ij} \equiv V_{ij}/V(Y)$ is the *second order sensitivity index*, and so on. The sum of all sensitivity indices up to kth order is one. Up to second order, the terms of the variance decomposition of Eq. (4) are $V_i = V(E(Y|X_i))$ and $V_{ij} = V(E(Y|X_i, X_j)) - V(E(Y|X_i)) - V(E(Y|X_j))$. Here the notation $E(Y|X_i)$ denotes the conditional expectation value of Y with fixed X_i. The variance of this expectation value, $V(E(Y|X_i))$ is then taken over the different values of X_i. The quantity V_i thus gives the contribution of X_i to the variance of Y, when the effect of all other variables is averaged out. However, V_i does not include any interaction effects of X_i with the other variables. The second order effect, V_{ij}, takes into account the interactions between two variables, X_i and X_j. Higher order terms are defined in a similar manner. Further discussion, along with illustrative examples, can be found, *e.g.*, in Chapters 1 and 4 of (Saltelli et al., 2008).

To make the connection with the previous discussion, let us look at the first order index S_i more closely. The index is defined as

$$S_i = \frac{V(E(Y|X_i))}{V(Y)}, \quad (6)$$

thus giving proportion of the variance caused by X_i in proportion to the total variance of Y. Therefore, in light of the discussion of Section 3.2, *for a linear model* it holds that $S_i = R_i^2$. The sensitivity index S_i is therefore a generalization of the linear regression correlation coefficient (or rather, its square). The variance decomposition method can therefore be used to extract the same information as linear regression (and more, as we will discuss), apart from the sign of the correlation, which is trivially obtainable.

Since S_i describes the additive (non-interacting) contribution of X_i to the variance of Y, the sum of the first order indices has an upper bound

$$\sum_{i}^{k} S_i \leq 1. \quad (7)$$

The equality is exact only for additive models, for which all the higher order indices are zero. However, nonlinearity does not imply break-down of the equality; the equality holds even for nonlinear systems, as long as the model is additive.

3.4.2. Total effect index

Measuring all the sensitivity indices up to kth order would explain all of the models variance. To do this in practice, however, would be a formidable computational task. Fortunately, it turns out that it is relatively inexpensive to estimate the so-called *total effect index*, T_i, which takes into account all the first-order and interaction effects of one variable X_i. The total effect index for variable X_i is defined as

$$T_i = \sum_{l}^{k} \delta_{il} S_l + \sum_{l}^{k}\sum_{m>l}^{k} (\delta_{il} + \delta_{im}) S_{lm} + \cdots + S_{12\ldots k}, \quad (8)$$

where δ_{ij} is the Kronecker delta. For example, for a three-variable model ($k = 3$), the total effect of variable X_1 is $T_1 = S_1 + S_{12} + S_{13} + S_{123}$.

The degree of non-additivity of the model with respect to input variable X_i can be characterized by the difference $T_i - S_i$. For additive models, having no interaction terms, this difference is equal to zero. On the other hand, for non-additive models the difference is positive:

$$T_i - S_i = 0 \,(\text{additive models}) \quad (9)$$

$$T_i - S_i > 0 \,(\text{non} - \text{additive models}) \quad (10)$$

A large difference signals the importance of interactions involving the variable X_i.

Since the second and higher order indices are included in the total effect indices of more than one variable, it holds that

$$\sum_{i}^{k} T_i \geq 1. \quad (11)$$

Again, the equality is exact for additive models.

3.4.3. Numerical implementation

Efficient evaluation of the Sobol' sensitivity indices has been studied considerably in the recent years (Saltelli et al., 2008, 2010; Glen and Isaacs, 2012; Jansen, 1999; Homma and Saltelli, 1996; Lilburne and Tarantola, 2009). The brute force method would use the bare definitions of the conditional variances to compute the indices. However, there are several more efficient approaches. Most of them rely on reducing the computational load by performing the random sampling in a very specific way, accomplished as follows.

First, two sets of random inputs are generated. The first set (the "sample") consists of Nk independent input values (N for each k inputs), used to solve the model N times. This gives N independent realizations of the output, $Y_{0,n}$, with $n = 1, 2, \ldots, N$ (the meaning of the subscript '0' will become apparent shortly). The same is then repeated for another independent set of random inputs (the "re-sample"), yielding another N independent solutions of the model. For the re-sampled outputs, we use the primed notation $Y'_{0,n}$. The sample and the re-sample inputs are then mixed to form k sets of inputs from the previously generated random numbers. This is done by taking all the input values from the sample set, except those corresponding to the input variable i, which are taken from the re-sample set. For each i, this gives a set of Nk input variables, which are again used to evaluate the model N times, giving the outputs $Y_{i,n}$. Here the subscript i is used to indicate the variable for which the re-sample set is used, with '0' signifying that no inputs from the re-sample are used. The mixing procedure is then repeated, this time using the re-sample set for all variables except one, and the sample set for the variable i. Evaluation of model with these inputs then gives the primed results, $Y'_{i,n}$. The whole procedure requires a total of $N(2k+2)$ model evaluations, the computational effort thus scaling linearly with the number of inputs k. For a more thorough discussion of the procedure, see, for instance, Chapter 4 of Saltelli et al. (2008), or Saltelli et al. (2010), Glen and Isaacs (2012).

Having obtained the outputs from the randomly sampled inputs, what remains is the calculation of the sensitivity indices. For this, there are many different formulas, each constructing the conditional variances in a slightly different way from the output combinations (for a recent review and comparison, see Glen and Isaacs, 2012). In this work, several different variants were assessed,

including those discussed in Saltelli et al. (2008, 2010), Saltelli (2002), Lilburne and Tarantola (2009), Jansen (1999). For the analyzed data, the method labeled 'D3' in Glen and Isaacs (2012) proved to be the most efficient one, giving the smallest errors with fixed N. The method subtracts spurious correlations (correlations caused by finite sample size in an ideally uncorrelated data) and uses double estimates for improved accuracy. The derivation of the method is described in Glen and Isaacs (2012).

The method is formulated using standardized output $Z_{i,n}$, defined as

$$Z_{i,n} = \left(Y_{i,n} - m_i\right)/\sqrt{v_i}, \tag{12}$$

where m_i is the mean $m_i = \frac{1}{N}\sum_n Y_{i,n}$ and v_i is the variance $v_i = \frac{1}{N}\sum_n Y_{i,n}^2 - M_i^2$. Analogous definition holds for the primed output. From the standardized data various correlations are then calculated. In the following, we drop the subscript n, so that $Z_i \equiv Z_{i,n}$, and the sum implies summation over n from 1 to N. The required correlations are

$$C_i = \frac{1}{2N}\sum\left(Z_0' Z_i + Z_0 Z_i'\right), \tag{13}$$

$$C_{-i} = \frac{1}{2N}\sum\left(Z_0 Z_i + Z_0' Z_i'\right), \tag{14}$$

$$P_i = \frac{1}{2N}\sum\left(Z_0 Z_0' + Z_i Z_i'\right), \tag{15}$$

$$C_{ai} = \frac{C_i - P_i C_{-i}}{1 - P_i^2}, \tag{16}$$

$$C_{a-i} = \frac{C_{-i} - P_i C_i}{1 - P_i^2}, \tag{17}$$

for the one-variable indices, and

$$C_{ij} = \frac{1}{2N}\sum\left(Z_i' Z_j + Z_i Z_j'\right), \tag{18}$$

$$C_{-ij} = \frac{1}{2N}\sum\left(Z_i Z_j + Z_i' Z_j'\right), \tag{19}$$

$$P_{ij} = \frac{1}{2N}\sum\left(Z_i Z_i' + Z_j Z_j'\right), \tag{20}$$

$$C_{aij} = \frac{C_{ij} - P_{ij} C_{-ij}}{1 - P_{ij}^2}, \tag{21}$$

$$C_{a-ij} = \frac{C_{-ij} - P_{ij} C_{ij}}{1 - P_{ij}^2}. \tag{22}$$

for the second-order indices. In the above the C's are the double estimate correlations, the P's the spurious correlations and the C_a's correlation estimates partly adjusted for spurious correlations.

The estimators for the sensitivity indices are then obtained as follows. The first-order index, or the main effect, is

$$S_i = C_j - P_j \frac{C_{a-i}}{1 - C_{ai} C_{a-i}}, \tag{23}$$

the total effect is

$$T_i = 1 - C_{-j} + P_j \frac{C_{a-i}}{1 - C_{ai} C_{a-i}}, \tag{24}$$

and the second order effect is

$$S_{ij} = C_{ij} - P_{ij} \frac{C_{a-ij}}{1 - C_{aij} C_{a-ij}} - S_i - S_j. \tag{25}$$

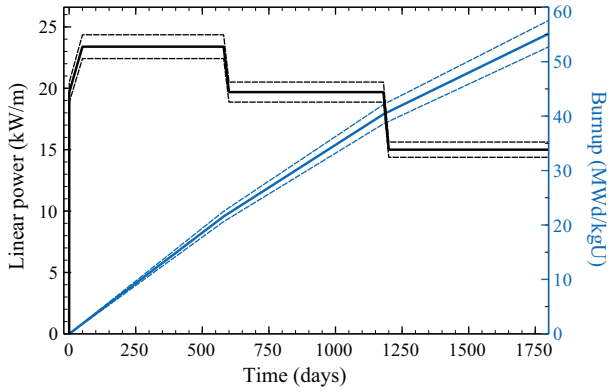

Fig. 1. Black lines, left axis: the power history (solid line) and its 95% confidence limits (dashed lines) used in the scenario. Blue lines, right axis: the resulting average burnup with the 95% confidence limits. (For interpretation of the references to color in this figure legend, the reader is referred to the web version of the article.)

3.5. Sampling of the input variables

The correlation coefficients and sensitivity indices can be calculated using pseudo-random numbers, quasi-random numbers or other methods to sample the input variable distributions. For quasi-random numbers, the input variable distributions can be calculated from the uniform distribution by numerical transform using the inverse cumulative distribution function (Press et al., 2002). In this work, the sampling was done with both pseudo-random and quasi-random numbers, using the Sobol' sequence (Sobol', 1967; Antonov and Saleev, 1979) to generate the latter, as recommended in the literature (Saltelli et al., 2008, 2010; Sobol', 1993). The quasi-random sampling showed slightly faster convergence, although no systematic study of the convergence rate was done. Hence, in the following Sections we show only the results obtained with the Sobol' sequence sampling of the input variables.

4. Scenario specifications and varied parameters

The analyzed scenario represents a hypothetical steady-state irradiation of a uranium oxide fuel rod in the Three Mile Island 1 (TMI-1) PWR reactor. The scenario is designed to bring the fuel rod to a relatively high burn-up of 50–60 MWd/kgU (depending on the input values), using a simplified power history shown in Fig. 1. The reactor power remains constant for several hundreds of days, with only two changes in the power level during the scenario. Since many of the measured quantities depend on the linear heat rate (LHR), such a simplification is in practice mandatory. The dependencies on the LHR can still be extracted by analyzing the uncertainty of the power history, and by looking at the changes that occur when the overall power level changes. The axial power profile is given in Table 1.

The relevant input parameters are reproduced in Table 2. The upper part of the table lists the fabrication and system parameters with their uncertainties, while the lower part lists the uncertainties in the material correlations, models and power history. For the fabrication parameters, the uncertainties reported in the OECD Benchmark for Uncertainty Analysis in Best-Estimate Modeling for Design, Operation and Safety Analysis of LWRs (UAM-LWR) (Blyth et al., 2012) have been used as a guideline. The uncertainties in the material correlations and computational models were determined

Table 1
The axial power profile of the scenario. Linear interpolation is used to obtain the power at the intermediate positions.

Position (mm)	0.0	304.8	609.6	914.4	2743.2	3048.0	3352.8	3657.6
Relative power	0.63	0.83	1.03	1.08	1.08	1.03	0.83	0.63

Table 2
The best estimate values of input parameters and their uncertainties (the 95% confidence interval) used in the analyzed scenario. If no uncertainties are indicated, the input was not varied. For the FRAPCON correlations and the power history (the bottom half of the table) only uncertainties are shown, since the best estimate value is a function of several variables or changes with time. The last column lists the abbreviation used for the varied input parameters in the figures of this paper.

Parameter	Value	Abbr.
Clad outer diameter	(10.92 ± 0.06) mm	clod
Clad thickness	(0.673 ± 0.025) mm	clth
Pellet outer diameter	(9.40 ± 0.02) mm	fuod
Total fuel height	3657.6 mm	–
Fuel pellet height	11.43 mm	–
Fuel enrichment (atom-%)	(4.85 ± 0.003)%	fuenrch
Density (% of theoretical)	(93.8 ± 1.6)%	fuden
Clad type	Zr-4	–
Fill gas type	Helium	–
Fill gas pressure	1207 kPa	–
Fuel rod pitch	14.43 mm	–
Coolant pressure	(15.51 ± 0.31) MPa	coolp
Coolant inlet temperature	(561 ± 3) K	coolt
Coolant mass flux	(3460 ± 69) kg/(m^{2}s)	coolmf
Fuel thermal conductivity	±10%	futc
Fuel thermal expansion	±15%	futex
FGR diffusion coefficient	+200%/-67%	Dfgr
Fuel swelling	±20%	fuswell
Clad creep	±30%	clcreep
Clad axial growth	±50%	clgrowth
Clad corrosion	±40%	clcor
Clad H concentration	±80 ppm	clhcon
Clad thermal conductivity	±5 W/mK	cltc
Clad thermal expansion	±30%	cltex
Gas thermal conductivity	±0.02 W/mK	gastc
Coolant heat transfer	±5%	coolhtc
Linear power	±5%	power

based on the data presented in a recent evaluation (Geelhood et al., 2009) and the recommendations given in the FRAPCON manual (Geelhood et al., 2011a,b). For all variables, the probability distribution is assumed Gaussian, with a cut-off at the lower and upper 2.5% percentiles. The input parameters are assumed mutually independent. For most inputs this assumption holds exactly, but for some only approximately. For instance, the rod's physical dimensions may become weakly correlated due to the manufacturing process. However, since data on such correlations is not available, the correlations are assumed negligible. For the power history, the same percentual deviation from the mean is used for each time step. Default FRAPCON-3.4 models are used in the code runs.

5. Results and discussion

5.1. General remarks

The scenario described in Section 4 was modeled with FRAPCON-3.4 using a Python script for sampling the input variable distributions and generating the FRAPCON input files. The distributions were sampled using the inverse cumulative distribution function method to transform the uniformly distributed Sobol' sequence quasi-random numbers into Gaussian numbers with the 2.5% upper and lower cut-offs. The sample size was $N = 50,000$ independent runs. In addition, for the Sobol' sensitivity indices, a re-sample of size $N = 50,000$ and 21 mixed samples of the same size (one for each input variable, as discussed in Section 3) were generated. The total number of performed FRAPCON runs was therefore 1.15×10^6, taking approximately 20 CPU-days on a Linux cluster.

The quantitative results of the analysis of course depend on the modeled scenario, parameter variations and the computational model. For example, increasing the variance of a single input parameter would increase its contribution in proportion to the others. Because of input interactions, simply scaling the results with the input's variance is not sufficient. Hence, the input variances should be chosen as realistic as possible for the analyzed scenario. In addition, the same analysis, repeated using a different fuel performance code, would give quantitatively different results due to the different underlying models. However, the trends discussed in this Section should be valid for steady state fuel behavior analysis in general.

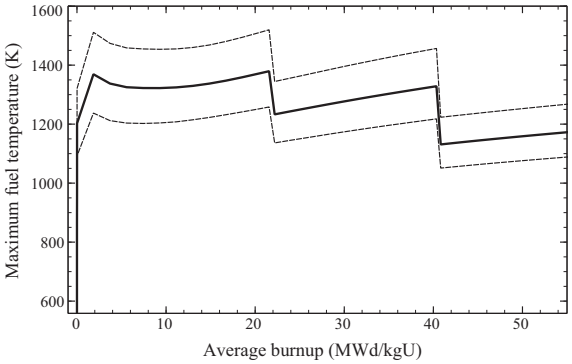

Fig. 2. The maximum fuel temperature (solid line) and its 95% confidence limits (dashed lines) as a function of burnup.

5.2. Average values and uncertainty analysis

Out of the sample of $N = 50,000$ independent runs, the average (mean) values were calculated for several outputs. The results for the maximum fuel temperature, average cladding temperature, rod internal pressure, axially averaged gap width and gap conductance, and the cladding radial displacement and hoop stress at the central axial node are shown in Figs. 2–9 . The uncertainties of the outputs were evaluated by calculating the upper and lower 2.5% percentiles (*i.e.*, the 95% confidence interval) from the modeled distribution. These are also shown in Figs. 2–9.

At the beginning of irradiation, the maximum fuel temperature climbs to almost 1370 K, as shown in Fig. 2. The temperature then goes down slightly as the conductivity of the fuel and the gap conductance improve as a result of pellet densification and reduction of the gap size. At slightly higher burnup, the temperature starts to increase as the accumulating fission products decrease the thermal conductivity of the fuel. The uncertainty of the temperature is significant, and remains roughly constant at ±130 K until the linear power is reduced, whereupon the uncertainty also decreases.

The mean cladding temperature behaves very similarly to the fuel temperature, slowly increasing with burnup and decreasing with decreasing power (see Fig. 3). The uncertainty remains quite

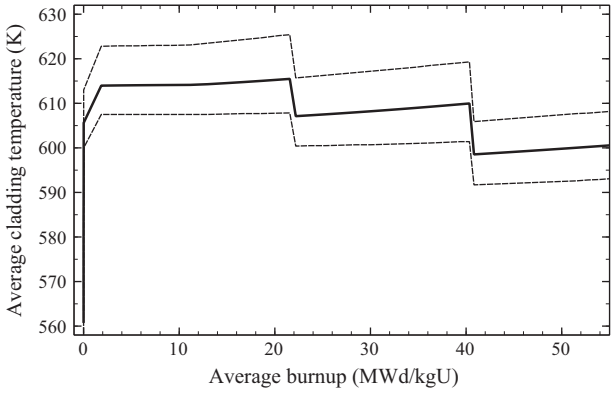

Fig. 3. The average cladding temperature (solid line) and its 95% confidence limits (dashed lines) as a function of burnup.

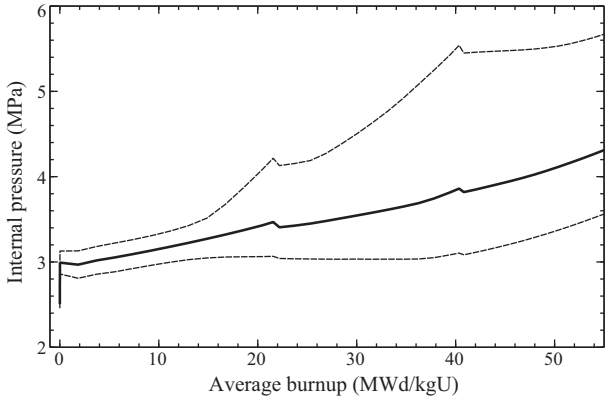

Fig. 4. The internal rod pressure (solid line) and its 95% confidence limits (dashed lines) as a function of burnup.

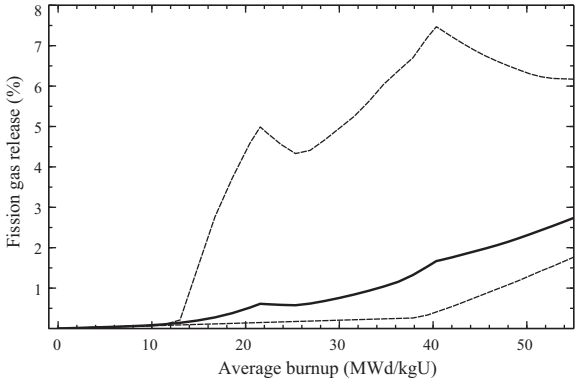

Fig. 5. The average amount of released fission gas (solid line) and its 95% confidence limits (dashed lines) as a function of burnup.

stable at ±8 K. However, even though the behavior looks very similar to the fuel temperature, the sensitivity analysis will reveal that the uncertainties in the fuel and cladding temperatures are dominated by completely different input uncertainties.

The internal pressure of the rod (Fig. 4) and the fission gas release (Fig. 5) behave very similarly, the time evolution of the FGR determining the evolution of the pressure to a large degree. With increasing amount of released fission gases, the pressure rises steadily with burnup. At the end of the irradiation, the average FGR amounts to roughly 2.7%, with the pressure reaching 4.3 MPa. The uncertainty in both is very high, and typically increases

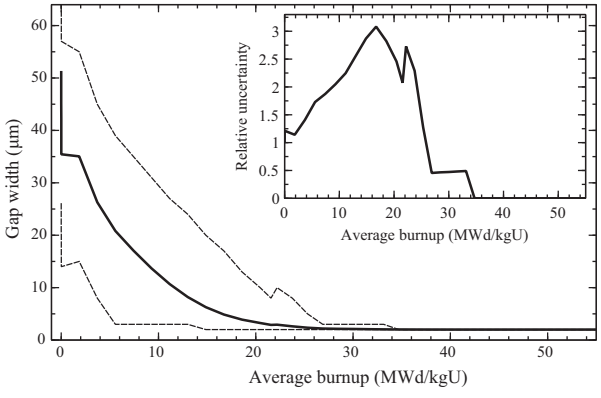

Fig. 6. Main plot: the average gap width (solid line) and its 95% confidence limits (dashed lines) as a function of burnup. Inset: the relative uncertainty of the gap width in proportion to the mean gap width.

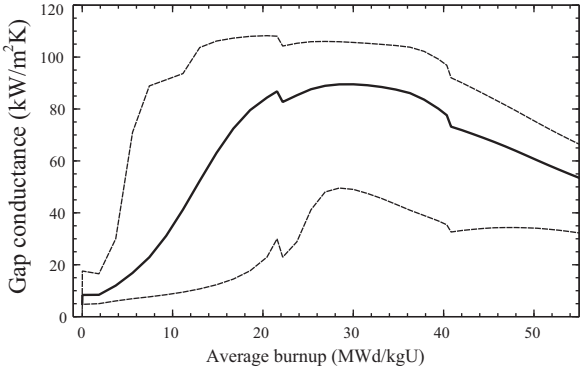

Fig. 7. The average gap conductance (solid line) and its 95% confidence limits (dashed lines) as a function of burnup.

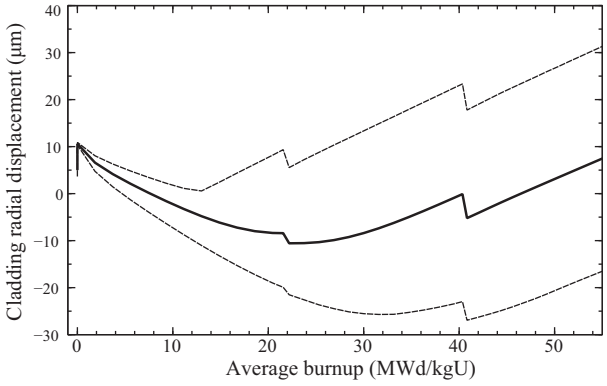

Fig. 8. The radial displacement of the cladding at the central axial node (solid line) and its 95% confidence limits (dashed lines) as a function of burnup.

with burnup. At the burnup of 40 MWd/kgU, the 95% confidence interval encompasses FGR amounts of 0.4% and 7.4%, and pressures between 3.1 MPa and 5.5 MPa.

The width of the pellet-cladding gap, shown in Fig. 6, is one the most important quantities to look at in the analysis of the fuel rod. At small burnup, the gap remains open, but eventually closes due to inward cladding creep and irradiation swelling of the fuel. This evolution of the gap width has a strong influence on the conductance of heat from the fuel to the cladding, and eventually leads to pellet-cladding interaction. In the present scenario, the gap remains almost completely open until the burnup of approximately 6 MWd/kgU, when it starts to close. Depending on the realization of the input variables, the gap has a fairly high probability of being open until about 25 MWd/kgU, and finally

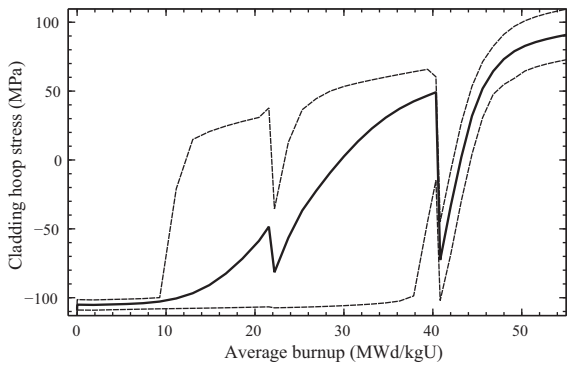

Fig. 9. The cladding hoop stress at the central axial node (solid line) and its 95% confidence limits (dashed lines) as a function of burnup.

closes in all the observed cases at approximately 40 MWd/kgU. The absolute uncertainty of the gap width decreases almost linearly with increasing burnup. However, the relative uncertainty (the width of the 95% confidence regime in proportion to mean gap width) behaves non-monotonically, first increasing with burnup and reaching its maximum of about 3 times the mean gap width at 16 MWd/kgU, then decreasing to zero as the gap closes.

The width of the gap and its uncertainty are reflected in the gap conductance (see Fig. 7). The conductance starts at a fairly modest mean value of 5 kW/m^{2}K, but increases beyond 80 kW/m^{2}K as the gap closes. The uncertainty also increases steeply, having its peak of about 94 kW/m^{2}K (between the lower and upper limits of the 95% tolerance) at the burnup of 15 MWd/kgU. It should be noted that this maximum uncertainty is much larger than is often assumed in non-fuel-specific modeling. From 20 to 35 MWd/kgU, the conductance remains close to 80 kW/m^{2}K. Towards higher burnups, the conductance again decreases due to the released fission gases into the gap, which decreases the overall conductance even when the pellet and the cladding are in mechanical contact. The effect of pellet-cladding interface pressure has also an effect on gap conductance when the gap is closed.

The radial displacement of the cladding is shown in Fig. 8. Initially, the cladding expands due to increasing temperature at rise to power. The cladding then begins to creep inwards because of the pressure difference. As the pellet comes into contact with the cladding, the direction changes and the cladding is pushed outward. This results in a bifurcation of the solutions into two groups. In one, the gap is closed and the cladding expands, while in the other the gap remains open and cladding continues to creep inward. As a result, the apparent uncertainty of the radial displacement increases strongly with burnup. The same is true for the cladding hoop stress, as shown in Fig. 9. Both the hoop stress and the radial displacement have very high uncertainties mid-scenario, at burnups of 20–40 MWd/kgU. As the gap closes after 40 MWd/kgU, the uncertainty in the hoop stress is dramatically reduced. For the radial displacement, which is accumulated over time, the large uncertainty remains even after gap closure.

5.3. Spearman correlation coefficients

As discussed in Section 3.3, a method that is often used to characterize the uncertainty and sensitivity of the output, is the calculation of correlation coefficients and, in particular, the Spearman rank correlation coefficient. Despite its inability to cope with non-additive terms, the Spearman correlation coefficient is still widely used because it is simple to implement in an analysis software and can be evaluated at relatively modest computational effort. It is also the sensitivity measure recommended by, for example, GRS (Glaeser, 2008).

We have used the sample of 50,000 independent runs to evaluate the Spearman correlation coefficients ρ between all the input-output pairs for different burnups. Since it would be cumbersome to present the data exhaustively, we focus only on the central findings. A snapshot of the correlation coefficients for the most important input variables at the burnup of 22 MWd/kgU is shown in Fig. 10. The same figure also visualizes the correlations between the input and output uncertainties in the form of scatter plots.

The first observation from the data is that the sensitivity to the input variables depends on the output. This is rather obvious, since the physical phenomena governing the response to the input are different for each output observable. Second, the thermal-mechanical behavior of the fuel rod is strongly influenced by the rod's burnup. Hence, the sensitivities to the input uncertainties also vary greatly with time and accumulated burnup. This important aspect will be discussed more closely in Section 5.4. Without going to specifics, we can however outline some general trends. For example, the coolant properties (temperature and pressure) tend to be most important for fresh rods, losing their relative importance as other factors come into play. Similarly, the pellet and cladding fabrication uncertainties tend to be most important for fresh and moderate-burnup rods (up to, say, 20 MWd/kgU). For higher burnups, the release of fission gases begins to dominate the uncertainties in many cases, along with the material properties such as the fuel thermal conductivity and expansion. However, because of the response to the inputs is different for each output, it is impossible to give any precise universal rules.

Table 3
The proportion of variance explained by additive contributions to the output variance, as given by $\sum_i^k \rho_i^2$ for different burnups (in MWd/kgU). The output abbreviations stand for (from left to right): gap conductance, internal pressure, maximum (fuel) temperature, average cladding temperature, cladding radial displacement at the central axial node, cladding hoop stress at the central axial node, and fission gas release.

Burnup	gapcon	intpr	tmax	tclav	cldr	hoopstrs	fgr
0.01	0.96	0.95	0.95	0.86	0.94	0.94	0.99
5.5	0.95	0.95	0.96	0.87	0.99	0.94	0.99
22	0.65	0.74	0.97	0.93	0.70	0.68	0.74
38	0.68	0.75	0.98	0.96	0.96	0.86	0.74
49	0.76	0.77	0.98	0.96	0.96	0.89	0.76

An important question is then, how well does the Spearman ρ explain the uncertainty of the output? As was discussed in Section 3.3, by construction the Spearman correlation coefficient can measure only the additive contributions to the output variance. However, we expect that the fuel behavior model will have complex non-additive interactions between various input parameters. To quantify the methods performance, we have calculated the sum $\sum_i^k \rho_i^2$ over the input variables X_i. For completely explained variance, the sum would be unity. A smaller value tells that part of the variance cannot be assigned to any of the input uncertainties. The results for different output observables at different times are gathered in Table 3. For low burnup, typically more than 95% of the variance is explained by the Spearman ρ.

With accumulated burnup, however, the sensitivity measure becomes significantly worse. Depending on the output, even as much as one third of the variance remains unexplained. For instance, at the burnup of 22 MWd/kgU, only 65% of the uncertainty in the gap conductance can be traced back to its source. For the remaining 35%, corresponding to the uncertainty of 28 kW/m^{2}K (cf. Fig. 7), the inputs responsible for the uncertainty cannot be identified. Thus, relying solely on the evaluation of ρ in sensitivity analysis can lead to serious lack of knowledge about the propagation of uncertainties.

5.4. Variance decomposition

5.4.1. General features and burnup dependence

To improve the results obtained with the Spearman correlation coefficients, the first order (S_i), second order (S_{ij}), and the total effect (T_i) sensitivity indices were evaluated from the sampled and re-sampled data of size $N = 50,000$. To calculate the averages, the sampling methods and estimators accounting for spurious correlations described in Section 3.4.3 were used. The statistical error was estimated by dividing the sample and the re-sample into 10 subgroups each, after which the averages were estimated independently for each subgroup. The estimate for the standard error was then calculated from the obtained averages. Such a bootstrapping method provides the averages as well as their error estimates without increasing the computational requirements (Archer et al., 1997).

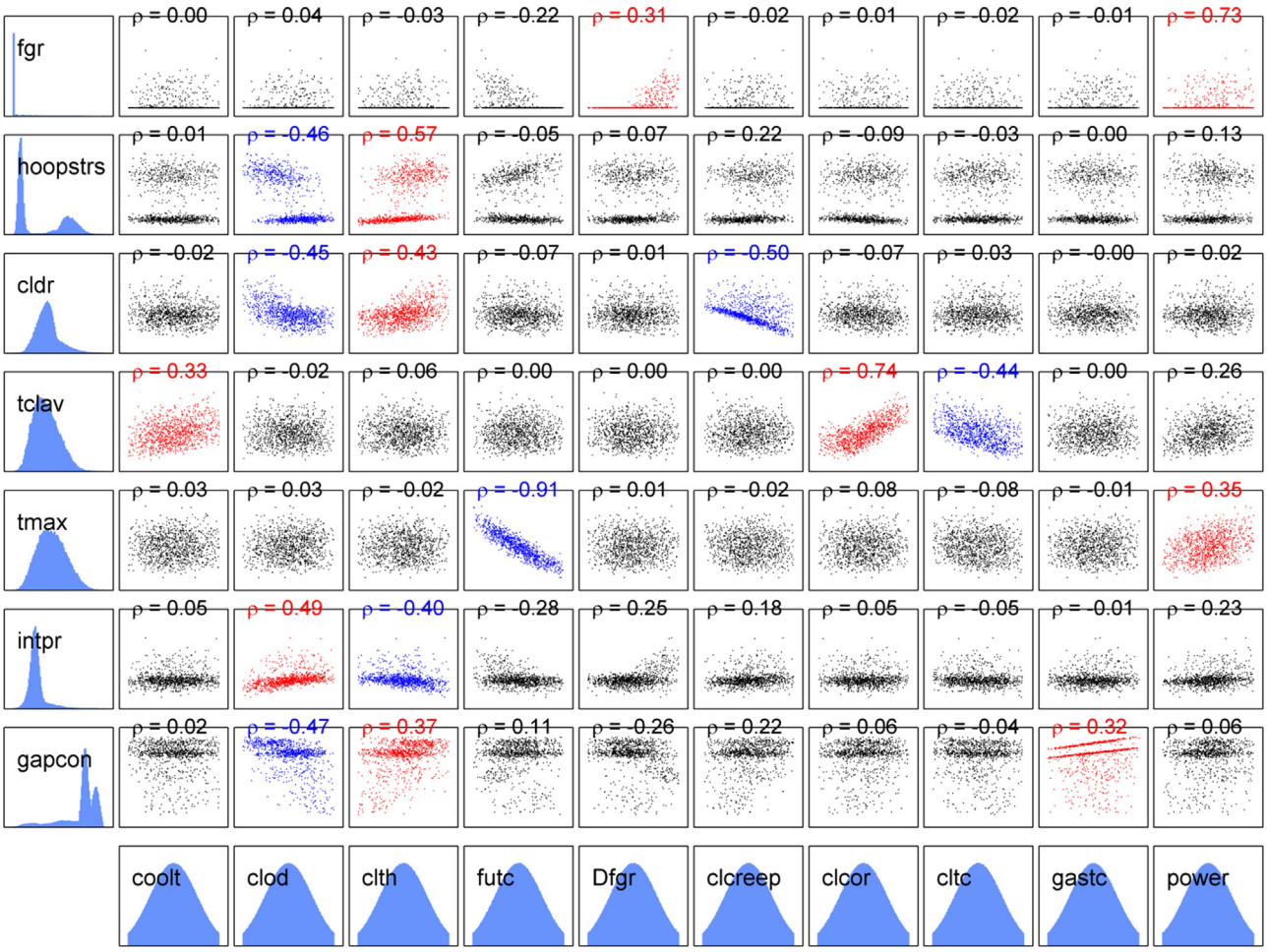

Fig. 10. Spearman correlation coefficients between the output and the most important input variables at the burnup of 22 MWd/kgU. The left column and the bottom row show the shape of the distribution of the output and input, respectively, while the middle part shows the scatter plots of the output as a function of the input variable. Here strong positive correlation is indicated with red color, and negative with blue color. For absolute values of the output and input, refer to Figs. 2–9 and Table 2. For the explanation of the inputs' abbreviations, refer to Table 2. The output abbreviations are the same as in Table 3. (For interpretation of the references to color in this figure legend, the reader is referred to the web version of the article.)

The first order and total effect indices evaluated for various output are shown in Figs. 11–18. The figures show the indices for the most important inputs as a function of burnup. In general, the importance of a given input depends not only on the considered output, but also on burnup. The results are consistent with the findings of the Spearman correlation coefficient analysis. Qualitatively, the ranking of the inputs by their importance is also very similar with both methods. However, important quantitative differences arise because of non-additive interactions between the inputs.

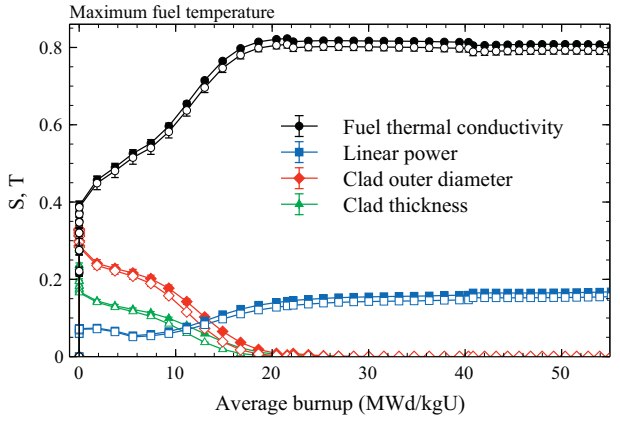

Fig. 11. Sobol' sensitivity indices for the maximum fuel temperature as a function of burnup. Open symbols correspond to the first order effects (S_i), while the closed symbols correspond to the total effect indices (T_i). Error bars indicate the 95% confidence limits.

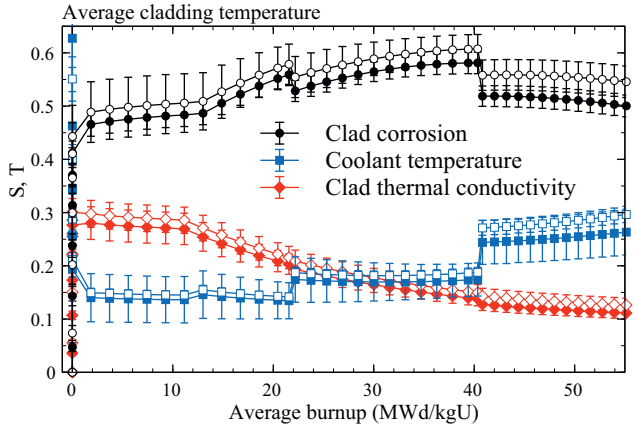

Fig. 12. Sobol' sensitivity indices for the cladding average temperature as a function of burnup. Conventions as in Fig. 11.

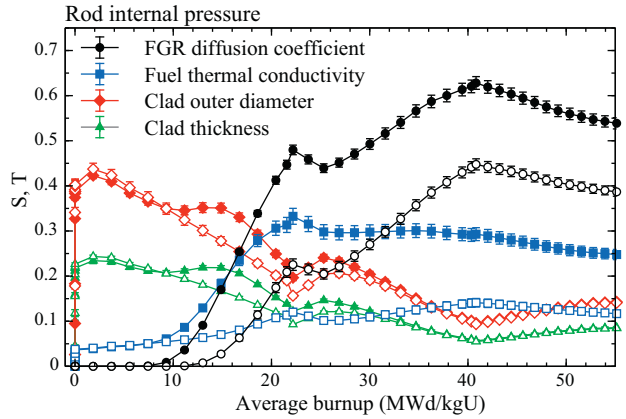

Fig. 13. Sobol' sensitivity indices for the rod internal pressure as a function of burnup. Conventions as in Fig. 11.

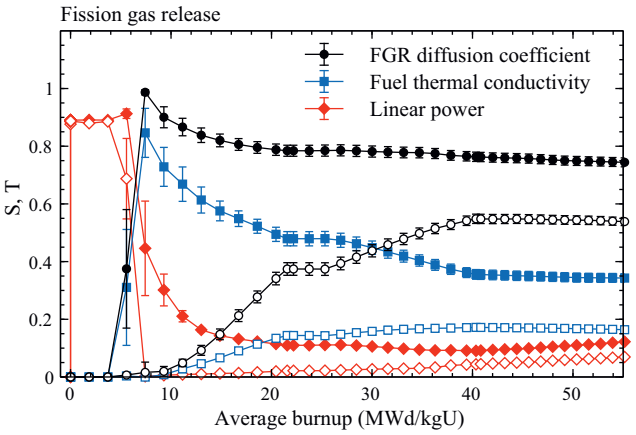

Fig. 14. Sobol' sensitivity indices for the fission gas release as a function of burnup. Conventions as in Fig. 11.

5.4.2. *Additivity of the outputs*

Based on the discussion of Section 5.3 and the results shown in Table 3, we expect that, for example, the maximum fuel temperature is an *additive* function of the inputs (irrespective of burnup). This means that, according to Eq. (9), the values of the indices S_i and T_i should be equal for any given i. As shown in Fig. 11, this is indeed the case. The figure shows the first order and total effect indices for the fuel thermal conductivity, average linear heat rate, and cladding outer diameter and thickness as a function of burnup. Independent of burnup, the indices agree within the statistical uncertainty, which shows that the maximum temperature is an additive function of the inputs and explains the good performance of the Spearman correlation coefficient.

As an opposite example, we may take the rod internal pressure. According to Table 3, for low burnup the Spearman correlation coefficient explains about 95% of the variance, which indicates

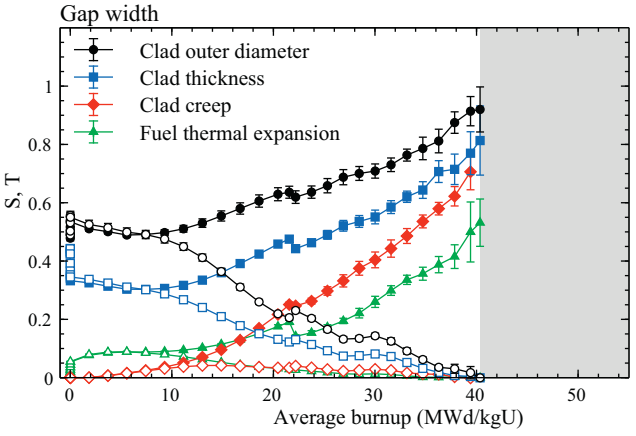

Fig. 15. Sobol' sensitivity indices for the gap width as a function of burnup. Evaluation of the indices beyond the burnup of approximately 40.4 MWd/kgU (indicated by the shaded area) is not possible because the gap is fully closed. Other conventions as in Fig. 11.

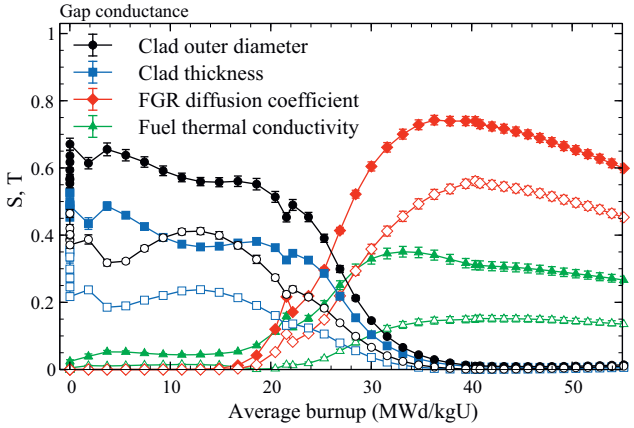

Fig. 16. Sobol' sensitivity indices for the gap conductance as a function of burnup. Conventions as in Fig. 11.

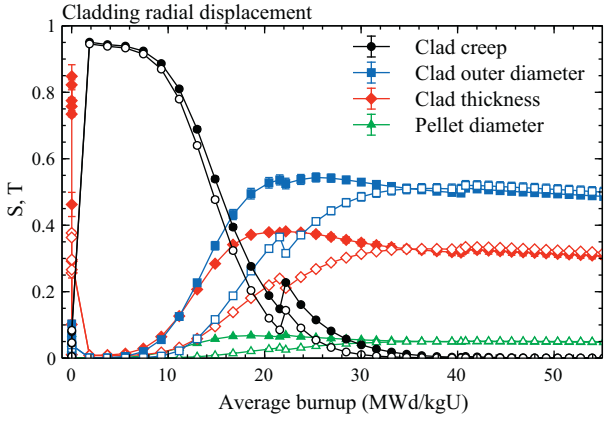

Fig. 17. Sobol' sensitivity indices for the cladding radial displacement at the center node as a function of burnup. Conventions as in Fig. 11.

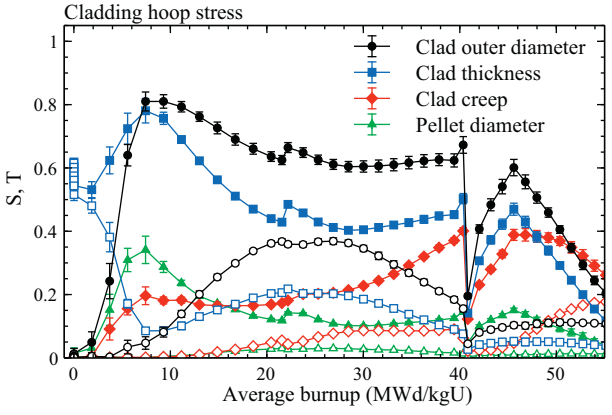

Fig. 18. Sobol' sensitivity indices for the cladding hoop stress at the center node as a function of burnup. Conventions as in Fig. 11.

near-additive behavior. However, at the burnup of 22 MWd/kgU and beyond, only about 75% of the variance is explained, suggesting non-additivity of the output. Looking at Fig. 13, the transition is clearly seen. Below 10 MWd/kgU, the first order and total effects indices are the same, diverging for higher burnup. Especially the indices linked to the FGR diffusion coefficient and fuel thermal conductivity display non-additivity, the total effects being about 0.15 higher than the first order effects.

Similar transitions between regions characterized by additive behavior and non-additive interactions can be seen for most of the outputs. The transition can also happen more than once, as for the cladding radial displacement (see Fig. 17), where the first order and total effect indices first diverge at the burnup of approximately 10 MWd/kgU, and then merge after 30 MWd/kgU.

Physically, at least two sources of the transitions can be identified. The first one is the introduction of new phenomena with increasing burnup. These phenomena can be either switched on by some criterion, or become gradually more important due to irradiation-induced mechanical and material changes. For example, the fission gas release (FGR) is unimportant at low burnup because the small amount of accumulated fission products in the fuel and their low fractional release into the gas gap. At moderate and high burnup, on the other hand, FGR has major influence on the rod internal pressure and gap conductivity. Since the FGR itself is strongly non-additive function of its inputs (especially the associated diffusion coefficient and the fuel thermal conductivity, as shown in Fig. 14), the non-additivity is transferred onward to other outputs. For example, the non-additivity of the internal pressure at burnups beyond 10 MWd/kgU is almost exclusively due to the coupling to FGR (see Fig 13).

The second major factor contributing to the transition between additivity and non-additivity is the evolution of the pellet-cladding gap. At low burnup the gap is open and the directly affected observables (internal pressure, cladding radial displacement and the gap width itself, see Figs. 13, 15 and 17) are additive. With accumulating burnup, the gap starts to close, with the exact moment depending statistically on the input values. The probability that the gap is closed quickly increases after 8 MWd/kgU, becoming almost certain around 30 MWd/kgU (see Fig. 6). In this intermediate regime, the statistical average of the outputs is taken over both the open and closed gap cases. The two cases are governed by completely different mechanical solutions, which gives rise to increased interaction between the inputs. This is reflected in Figs. 13, 15 and 17 by the difference between the first order indices and the total effect indices. For the cladding radial displacement and the internal pressure, the behavior becomes additive after the gap is completely closed at 34 MWd/kgU (apart from the contribution of the FGR). For the gap width, the simple additive behavior is never recovered. In fact, the behavior becomes progressively less additive, with 13 out of the 22 total effect indices having at least 10% influence on the variance of the gap width at 38 MWd/kgU. Although further analysis of uncertainty propagation in such a case would be extremely difficult, it is of little practical importance since the overall variance of gap width beyond 35 MWd/kgU is negligible.

As an important observation, we note that, according to Fig 16, the gap conductance is a non-additive function of the inputs throughout the scenario. At low to moderate burnups, the uncertainty is mostly attributed to the rod fabrication uncertainties, cladding outer diameter and thickness in particular. Because the gap conductance model itself is a non-additive function of the gap width (Geelhood et al., 2011a), the behavior is non-additive even for fresh fuel. After approximately 20 MWd/kgU, the dominant source of uncertainty is the FGR, with the model's diffusion coefficient being the most important source of uncertainty, followed by the uncertainty of the fuel thermal conductivity.

5.4.3. Performance of the variance decomposition

In Section 5.3, we evaluated the Spearman correlation coefficients for the gap conductance. At the burnup of 22 MWd/kgU, the sum of ρ_i^2 over all the inputs i was 0.65, as shown in Table 3. This result is very similar to what is obtained with the first order Sobol' indices. For the gap conductance at 22 MWd/kgU, the indices sum to $\sum_i S_i = 0.6$, which is of course no improvement over the Spearman coefficients.

However, the real advantage of the variance decomposition comes from the ability to quantify the interactions between input variables. For this purpose, the terms in the variance decomposition can be used in different combinations. For example, one may take the into account all the first order (S_i) and second order (S_{ij}) indices. For the gap conductance at 22 MWd/kgU, the sum

Table 4
The highest sensitivity of the output observables (top row) to the input variables (left column) during the scenario. The numbers in parentheses indicate the highest values of the total effect index T_i evaluated over the whole scenario for the particular input/output pair. The preceding number indicates the highest rank obtained during the scenario, with, *e.g.*, a "2." indicating that the particular variable has the second largest T_i at some point in the scenario, but never the largest one. The inputs are ordered by importance based on the ranking described above. For the abbreviations, refer to Tables 2 and 3.

Input	gapcon	intpr	tmax	tclav	cldr	hoopstrs	fgr
clod	1. (0.67)	1. (0.42)	1. (0.33)	8. (0.00)	1. (0.54)	1. (0.81)	3. (0.64)
Dfgr	1. (0.74)	1. (0.63)	6. (0.00)	12. (0.00)	11. (0.00)	10. (0.03)	1. (0.99)
clth	2. (0.53)	2. (0.23)	2. (0.28)	6. (0.00)	1. (0.85)	1. (0.78)	4. (0.52)
futex	3. (0.18)	1. (0.46)	5. (0.04)	10. (0.00)	4. (0.21)	1. (0.41)	4. (0.37)
clcreep	3. (0.21)	6. (0.05)	6. (0.02)	17. (0.00)	1. (0.95)	1. (0.40)	7. (0.06)
futc	2. (0.35)	2. (0.33)	1. (0.82)	11. (0.00	7. (0.06)	2. (0.36)	2. (0.85)
power	3. (0.14)	4. (0.11)	2. (0.17)	4. (0.07)	4. (0.13)	5. (0.16)	1. (0.91)
clcor	6. (0.03)	5. (0.12)	4. (0.01)	1. (0.58)	2. (0.39)	3. (0.12)	7. (0.01)
fuswell	8. (0.05)	11. (0.01)	11. (0.00)	16. (0.00)	3. (0.08)	1. (0.38)	11. (0.00)
coolt	7. (0.02)	5. (0.06)	5. (0.05)	1. (0.86)	3. (0.47)	6. (0.06)	6. (0.00)
coolp	5. (0.05)	2. (0.24)	7. (0.01)	9. (0.00)	2. (0.81)	2. (0.32)	7. (0.00)
cltc	8. (0.01)	9. (0.01)	5. (0.01)	2. (0.28)	2. (0.34)	9. (0.03)	5. (0.03)
fuden	5. (0.02)	7. (0.02)	3. (0.02)	9. (0.00)	8. (0.03)	9. (0.03)	2. (0.15)
fuod	3. (0.13)	4. (0.05)	5. (0.03)	10. (0.00)	3. (0.07)	3. (0.34)	3. (0.19)
gastc	4. (0.14)	9. (0.00)	7. (0.01)	21. (0.00)	13. (0.02)	10. (0.01)	9. (0.04)
fuenrch	16. (0.00)	16. (0.00)	15. (0.00)	12. (0.00)	17. (0.00)	16. (0.00)	4. (0.00)
coolmf	12. (0.00)	13. (0.00)	9. (0.00)	6. (0.00)	11. (0.05)	13. (0.01)	5. (0.00)
coolhtc	12. (0.00)	12. (0.00)	8. (0.00)	5. (0.01)	8. (0.08)	12. (0.01)	14. (0.00)
clgrowth	15. (0.00)	7. (0.02)	15. (0.00)	18. (0.00)	16. (0.00)	14. (0.01)	12. (0.00)
clhcon	20. (0.00)	20. (0.00)	20. (0.00)	19. (0.00)	20. (0.00)	20. (0.00)	17. (0.00)
cltex	21. (0.00)	21. (0.00)	21. (0.00)	20. (0.00)	21. (0.00)	21. (0.00)	19. (0.00)

of the second order indices is $\sum_i \sum_{j<i} S_{ij} = 0.28$, giving a total of 0.88 with the S_i's. Another way is to take the total effect of one variable X_i, and the first order effects of all other variables. This takes into account the first order effects of all variables and the interactions terms that involve the variable X_i. For example, one may choose the total effect of the cladding outer diameter, $T_{\mathrm{clod}} = 0.50$, and the first order effects $\sum_i S_i - S_{\mathrm{clod}} = 0.36$. This partition would bring the total to 0.86. In addition, one can take into account the second order effects *not* involving the cladding outer diameter (since these are already accounted for in T_{clod}). In this case, the most significant second order indices are $S_{\mathrm{futc,Dfgr}} = 0.057$, $S_{\mathrm{clth,clcreep}} = 0.0175$, $S_{\mathrm{Dfgr,power}} = 0.011$, $S_{\mathrm{futc,power}} = 0.0074$, $S_{\mathrm{clth,futex}} = 0.0074$ and $S_{\mathrm{clth,power}} = 0.0072$. Including these in the calculation takes the sum to 0.97.

This is a remarkable improvement from the Spearman ρ: instead of 35%, only 3% of the variance remains unaccounted for. Even the missing 3% can be tracked down by including the remaining second order terms in the calculation, which brings the overall sum to 1.00.

5.4.4. Ranking of the input variables

Finally, we should assess the question of the relative importance of the input uncertainties. As discussed above and shown in Figs. 11–18, the importance depends on the considered output and burnup. Therefore it is not possible to specify an input that universally ranks as the most important. However, some of the inputs appear to have significant impact on more than one output, and thus should rank high in importance, while others have virtually no influence on any of the outputs at all.

To simplify the matter, we have done the following. For each input and output, we have looked at the total effect indices (T_i) over the whole simulated scenario, collecting two sets of statistics. First, we have taken the maximum rank the input has for the given output. For example, if the input has the highest T_i for any nonzero burnup, the maximum rank will be one. Because the inputs' importances change with burnup, more than one input may have the same maximum rank. In addition, we have gathered the maximum values of T_i for nonzero burnup in the scenario.

The maximum ranks and values are shown in Table 4 for each varied input and for the most important outputs. The inputs are ordered so that on the top is the one with most number one ranks, followed by the one with second to most number one ranks, and so on. Although the ordering is somewhat arbitrary, it allows to quickly distinguish those inputs with significant contributions to the uncertainty of *some output at some point in the scenario* from the insignificant ones. In particular, since the total effect index is used for the evaluation, one can quickly discard the bottom ones as having almost no effect on the output. For example, in future analyses, it would be quite safe to consider the cladding thermal expansion (cltex in Table 4) as precise input, since its total effect to the overall variance of any of the considered outputs at any burnup between 0 and 55 MWd/kgU is less than 1%.

On the basis of Table 4, the input variables with the most broad impact on the uncertainties of the model's results are the cladding outer diameter, the diffusion coefficient of the fission gas release model, cladding thickness, fuel thermal expansion, cladding creep correlation, fuel thermal conductivity and the average linear heat rate. However, 15 out of the 21 inputs contribute significantly (by more than 10%) to the total variance of some output at some value of burnup. This result highlights the complexity of the system and demonstrates its sensitivity to the input values.

6. Conclusions

A hypothetical scenario of steady state irradiation of a TMI-1 fuel rod has been modeled with the FRAPCON-3.4 code. The uncertainties in input variables have been taken into account by Monte Carlo sampling from probability distributions, and extensive modeling of the different realizations has been done. The propagation of uncertainties has been analyzed using both the Spearman correlation coefficient method, which is conventionally used in the field, and by evaluating the first order, second order and total effect Sobol' sensitivity indices. The Sobol' variance decomposition is shown to perform significantly better in cases where non-additive interactions between input variables are present. This includes practically all the analyzed cases, with the exception of maximum fuel temperature and average cladding temperature. For example, in identifying the sources of uncertainty for the gap conductance at moderate burnup (22 MWd/kgU), the variance decomposition method can identify practically 100% of the input's contributions, while the Spearman correlation method only explains 65% of the output variance in the analyzed scenario.

The results suggests that first order sensitivity analysis methods should be used with caution in fuel performance modeling. With the possible exception of fuel centerline and cladding temperatures, the analysis should be complemented with higher order methods that take into account input interactions.

The interactions of the inputs and the necessity for higher order methods stem from the complexity of the system. For the same reason, identifying a single dominant source of uncertainty is not possible. The relative importance of the inputs depends not only on the considered output, but also on burnup. For instance, out of the 21 considered inputs, 15 have a contribution larger than 10% to the uncertainty of some output at some point in the scenario. In addition to complicating the analysis, this fact also makes it difficult to rule out inputs as a source of output uncertainty.

However, some fairly consistent trends can be identified. The inputs affecting the gap width, and thus gap conductance, rank among the most important ones. These are the as-fabricated cladding dimensions, cladding creep, fuel thermal expansion and, to some degree, the as-fabricated pellet diameter. Mostly the fabrication parameters influence the uncertainties at low burnup, with the other inputs becoming more important later in the rod's life, although for the cladding radial displacement the situation is reversed. Other important uncertainty sources are the diffusion coefficient in the FGR model, fuel thermal conductivity and linear power. The ranking of the inputs is very similar to that obtained in other sensitivity studies of the fuel rod (Christensen et al., 1981; Wilderman and Was, 1984; Boulore et al., 2012), although the present study identifies the FGR-related uncertainties among the most important ones. However, because FGR is a highly non-additive function of its inputs, it is easy to underestimate its contribution with first-order methods.

In addition to FGR, the evolution of the pellet-cladding gap with changing burnup is identified as one of the main sources involved in the burnup dependency of the sensitivity indices. Since the open gap and closed gap cases are governed by different physical models, the closure of the gap has a big influence on many of the sensitivity indices. In addition, the burnup regime where the gap is in the process of closing (*i.e.*, has a significant probability for both the open and closed states) is observed to have increased interaction between the inputs, caused by the mixing of the two states of the gap. Since the intermediate burnup regime is also an important regime of operation of nuclear reactors, this highlights the importance of using appropriate, higher order methods in the sensitivity analysis of the nuclear fuel rod.

Acknowledgements

This work was funded by SAFIR2014, the Finnish Research Programme on Nuclear Power Plant Safety 2011–2014.

References

Antonov, I., Saleev, V., 1979. An economic method of computing LP_T-sequences. USSR Comput. Math. Math. Phys. 19, 252–256.

Archer, G., Saltelli, A., Sobol, I., 1997. Sensitivity measures, ANOVA-like techniques and the use of bootstrap. J. Stat. Comput. Simulat. 58, 99–120.

Bailly, H., Menessier, D., Prunier, C. (Eds.), 1999. The Nuclear Fuel of Pressurized Water Reactors and Fast Neutron Reactors. Lavoisier Publishing.

Blyth, T., Avramova, M., Ivanov, K., Royer, E., Sartori, E., Cabellos, O., 2012. Benchmark of uncertainty analysis in modeling (UAM) for design, operation and safety analysis of LWRs, Volume II: Specification and support data for the core cases (Phase II) [draft version 1.0]. Technical Report NEA/NSC/DOC(2012)? Nuclear Energy Agency.

Boulore, A., Struzik, C., Gaudier, F., 2012. Uncertainty and sensitivity analysis of the nuclear fuel thermal behavior. Nucl. Eng. Des. 253, 200–210.

Cacuci, D., 2010. Handbook of Nuclear Engineering. Springer.

Cacuci, D., Ionescu-Bujor, M., 2004. A comparative review of sensitivity and uncertainty analysis of large-scale systems – II: Statistical methods. Nucl. Sci. Eng. 147, 204–217.

Christensen, R., Eilbert, R., Rohrer, R., Was, G., 1981. Adjoint sensitivity analysis in nuclear reactor fuel behavior modeling. Nucl. Eng. Des. 66, 125–139.

Draper, N., Smith, H., 1998. Applied Regression Analysis. John Wiley & Sons.

Geelhood, K., Luscher, W., Beyer, C., 2011a. FRAPCON-3.4: A computer code for the calculation of steady-state thermal-mechanical behavior of oxide fuel rods for high burnup. Technical Report NUREG-CR-7022, Vol. 1. Pacific Northwest National Laboratory.

Geelhood, K., Luscher, W., Beyer, C., 2011b. FRAPCON-3.4: Integral assessment. Technical Report NUREG-CR-7022, vol. 2. Pacific Northwest National Laboratory.

Geelhood, K., Luscher, W., Beyer, C., Senor, D., Cunningham, M., Lanning, D., Adkins, H., 2009. Predictive bias and sensitivity in NRC fuel performance codes. Technical Report NUREG-CR-7001. Pacific Northwest National Laboratory.

Glaeser, H., 2008. GRS method for uncertainty and sensitivity evaluation of code results and applications. Sci. Technol. Nucl. Installations 2008, 798901.

Glen, G., Isaacs, K., 2012. Estimating sobol sensitivity indices using correlations. Environ. Model. Softw. 37, 157–166.

Homma, T., Saltelli, A., 1996. Importance measures in global sensitivity analysis of model output. Reliability Eng. Syst. Safety 52, 1–17.

Ikonen, T., 2012. Variance decomposition as a method of statistical uncertainty and sensitivity analysis of the fuel performance code FRAPCON-3.4. Technical Report VTT-R07723-12. VTT Technical Research Center of Finland.

Ionescu-Bujor, M., Cacuci, D., 2004. A comparative review of sensitivity and uncertainty analysis of large-scale systems – I: Deterministic methods. Nucl. Sci. Eng. 147, 189–203.

Jansen, M., 1999. Analysis on variance designs for model output. Comput. Phys. Commun. 117, 35–42.

Kvam, P.H., Vidakovic, B., 2007. Nonparametric Statistics with Applications to Science and Engineering. John Wiley & Sons.

Lilburne, L., Tarantola, S., 2009. Sensitivity analysis of models with spatially-distributed input. Int. J. Geogr. Inform. Sci. 23, 151–168.

Press, W., Teukolsky, S., Vetterling, W., Flannery, B., 2002. Numerical Recipes in C, 2nd edition. Cambridge University Press.

Rashid, J., Yagnik, S., Montgomery, R., 2011. Light water reactor fuel performance modeling and multi-dimensional simulation. J. Miner. Met. Mater. Soc. 63 (8), 81–88.

Sallaberry, C.J., Helton, J.C., 2006. An introduction to complete variance decomposition. In: IMAC-XXIV: Conference & Exposition on Structural Dynamics.

Saltelli, A., 2002. Making best use of model evaluations to compute sensitivity indices. Comput. Phys. Commun. 145, 280–297.

Saltelli, A., Annoni, P., 2010. How to avoid a perfunctory sensitivity analysis. Environ. Model. Softw. 25, 1508–1517.

Saltelli, A., Annoni, P., Azzini, I., Campolongo, F., Ratto, M., Tarantola, S., 2010. Variance based sensitivity analysis on model output. Design and estimator for the total sensitivity index. Comput. Phys. Commun. 181, 259–270.

Saltelli, A., Ratto, M., Andres, T., Campolongo, F., Cariboni, J., Gatelli, D., Saisana, M., Tarantola, S., 2008. Global Sensitivity Analysis. The Primer. John Wiley & Sons.

Sobol', I., 1967. Distribution of points in a cube and approximate evaluation of integrals. USSR Comput. Math. Math. Phys. 7, 86–112.

Sobol', I., 1993. Sensitivity analysis for non-linear mathematical models. Math. Model. Comput. Exp. 1, 407–414.

Syrjälahti, E., 2006. New sensitivity analysis tool for VTT's reactor dynamic codes. In: IYNC 2006, International Youth Nuclear Congress.

Wilderman, S., Was, G., 1984. Application of adjoint sensitivity analysis to nuclear reactor fuel rod performance. Nucl. Eng. Des. 80, 27–38.

PUBLICATION II

Module for thermomechanical modeling of LWR fuel in multiphysics simulations

Annals of Nuclear Energy, **84**, 111–121.

Annals of Nuclear Energy 84 (2015) 111–121

Contents lists available at ScienceDirect

Annals of Nuclear Energy

journal homepage: www.elsevier.com/locate/anucene

Module for thermomechanical modeling of LWR fuel in multiphysics simulations

Timo Ikonen *, Henri Loukusa, Elina Syrjälahti, Ville Valtavirta, Jaakko Leppänen, Ville Tulkki

VTT Technical Research Centre of Finland, P.O. Box 1000, FI-02044 VTT, Finland

ARTICLE INFO

Article history:
Received 31 March 2014
Received in revised form 25 September 2014
Accepted 2 November 2014
Available online 24 November 2014

Keywords:
Fuel rod behavior
Nuclear fuel modeling
Multiphysics
FINIX

ABSTRACT

We have developed a new light-weight fuel behavior code FINIX, specifically designed for modeling of LWR fuel rods in multiphysics simulations. A thermomechanical description of the rod is required especially in transient conditions, where the heat transfer and changes in the rod's physical dimensions are strongly coupled. In addition to the mechanical deformations, FINIX solves the temperature distribution in the rod and the heat flux from the cladding to the coolant, allowing two-way coupling of the fuel behavior simulation with both neutronics and thermal hydraulics simulations. In this paper, we describe the FINIX module and compare its performance with experimental data and FRAPTRAN-1.4, a widely used fuel behavior code. The comparison reveals good agreement in both cases. We also demonstrate how FINIX can be integrated into multiphysics simulations. Coupled with the Monte Carlo reactor physics code Serpent, we simulate a fast reactivity transient with the fuel temperature and fission power solved self-consistently. With the reactor dynamics codes TRAB-1D and TRAB3D/SMABRE, we simulate a fast power transient and a PWR main steam line break. The latter serves as an example of coupled fuel behavior, neutronics and system-level thermal hydraulics simulation.

1. Introduction

In a light water reactor (LWR), the thermal and mechanical behavior of the fuel rods strongly influences the behavior of the whole reactor in both steady state and transient conditions. For example, the power of the reactor is sharply affected by the fuel temperature due to the absorption of neutrons by Doppler-broadened cross sections (Lamarsh, 1966). This coupling is important both in the steady state and, even more so, in transients, where the negative feedback between the fuel temperature and reactivity constitutes one of the most important safety features of LWR's. Similarly, transient heat transfer to the coolant and avoiding departure from nucleate boiling is dependent on the rate of heat transfer from the pellet to the cladding and, consequently, to the coolant. This again depends on both the rod's thermal and mechanical states (Cacuci, 2010). Both the neutron absorption and coolant boiling are typically modeled by dedicated computer codes – the first one by reactor physics codes, and the second one by thermal hydraulics codes. However, in both cases the code needs an advanced description of the fuel rod's thermomechanical behavior to capture the essential physics. A thermal element model, simple correlations, or user-given temperatures are vastly insufficient due to the intricate coupling of the rod's mechanical deformations and heat transfer properties (Bailly et al., 1999). Furthermore, effects of long-term irradiation compound the problem.

To address the challenge of simulating the thermomechanical behavior of the fuel rod within different contexts, we have developed a new LWR fuel behavior code, FINIX (Ikonen et al., 2013; Ikonen, 2013). The purpose of FINIX is to provide a universal fuel module for multiphysics simulations done with, for example, coupled neutronics, thermal hydraulics and reactor dynamics codes. For this purpose, FINIX has been developed to be as simple as possible, while still being able to realistically describe the physics in the regime of its intended use.

The current modeling capabilities of FINIX are aimed towards calculating the fuel rod's thermal behavior in fast transient simulations, although more limited capabilities to model also steady state behavior exist. At present, FINIX solves the time-dependent heat transfer across the pellet, gas gap and the cladding, taking into account elastic and thermal deformations and their coupling to the gap conductance. Material correlations are taken from public literature. Initialization for accumulated burnup can be done using a FRAPCON simulation for the steady state irradiation. For a more easy-to-use initialization, a parameterization method for burnup-dependent quantities is also under development.

* Corresponding author. Tel.: +358 40 659 2130; fax: +358 20 722 5000.
E-mail address: timo.ikonen@vtt.fi (T. Ikonen).

http://dx.doi.org/10.1016/j.anucene.2014.11.004
0306-4549/

For the stand-alone FINIX, we present validation results against experimental Halden temperature data and FRAPTRAN-1.4 simulations of reactivity initiated accidents. The comparisons show good performance of the FINIX module. In addition, we integrate FINIX with the Monte Carlo reactor physics code Serpent, allowing simultaneous and self-consistent solution of the fuel temperature and power. We also show results for the integration of FINIX into the reactor dynamics codes TRAB3D and TRAB-1D, and demonstrate its use in the simulation of a PWR main steam line break and a fast power peak. Finally, we summarize our results and discuss possible directions for future work.

2. The FINIX module

2.1. General description

FINIX is a fuel behavior module designed to be integrated as a subprogram into a larger simulation code, where FINIX replaces the existing fuel model. The main design philosophy of FINIX is to provide a simple but sufficient model of the fuel rod that can be used in different types of simulation codes, including neutronics, reactor dynamics, thermal hydraulics, and system codes. While multiphysics capabilities can also be achieved with direct code-to-code coupling (see, e.g., Hämäläinen et al., 2001; Rossiter, 2011), such approach is often laborious when highly specialized software is involved. Thus, in the design of the FINIX code, flexibility of the interface between FINIX and the main simulation code has been prioritized. This facilitates integration into a wide range of different simulation codes.

FINIX is integrated with the main simulation code, which we shall refer to as the *host code*, at the source code level. This has the benefits of reduced data transfer between the codes, and allows the host code to have direct access to FINIX's functions and data structures. However, FINIX also has a high-level interface, through which the most common functionalities can be used without detailed knowledge of the FINIX data structures. In addition, to reduce the user's need for fuel-specific knowledge, FINIX has an internal database for different fuel types, from which the required fuel simulation parameters can be loaded in by just specifying the desired fuel rod type.

The interface also includes an error message system that FINIX uses to communicate with the host code. FINIX checks the simulation parameters and calculated results against its models' ranges of validity and informs the host code if the range has been violated by passing an error message. Other types of errors can also be passed to the host code. Short of encountering a fatal error, FINIX will not halt the simulation's execution, but will signal of potentially unreliable results by using the error message system.

2.2. FINIX models overview

FINIX is primarily designed as a transient simulation code. Compared full-fledged fuel performance codes such as FRAPTRAN (Geelhood et al., 2011b), TRANSURANUS (Lassmann, 1992) and BISON (Williamson et al., 2012), FINIX emphasizes flexibility and the needs of the host code in favor of the fuel performance modeling. For example for neutronics simulations of fast transients, the most important quantity to solve is the time-dependent temperature distribution. On the other hand, many of the phenomena modeled in fuel performance codes such as cladding irradiation growth are less important in this case and are currently not considered in FINIX. However, similar to the work of Rohde (2001) and for example the fuel model of RELAP (ISL Inc., 2010), the coupling between the mechanical behavior of the gap and the radial heat transfer is modeled. Here FINIX takes an approach similar to FRAPTRAN, although some simplifications are done as described below.

The FINIX model itself involves solving both the thermal and mechanical behavior of the fuel rod, allowing not only thermal effects but also changes in rod geometry to be taken into account in the host code. The thermal and mechanical models are coupled by the gap pressure and conductance, which are functions of both the rod temperature and mechanical dimensions. Both the heat equation and the mechanical behavior are solved radially in one dimensional, cylindrical and axisymmetric geometry, independently for several axial nodes. The solutions of the different axial nodes are coupled via the gap pressure, which is solved simultaneously for the whole rod. This scheme constitutes what is generally referred to as the 1.5-dimensional model. The main modules of FINIX and their interrelationships are shown in Fig. 1, with the thermal and mechanical models described in more detail in Sections 2.3 and 2.4. Properties such as thermal conductivity, thermal expansion, Young's moduli, coolant heat transfer, etc., are solved using publicly available correlations. These are discussed in Sections 2.5 and 2.6.

Currently FINIX is not equipped with modules to describe long-term evolution of phenomena such as cladding creep and oxidation, fuel swelling, and accumulation of fission products. FINIX thus lacks most of the models needed for simulating the effects of burnup accumulation over a long steady state irradiation. Therefore, for non-fresh fuel, the initial state of the fuel rod prior to the

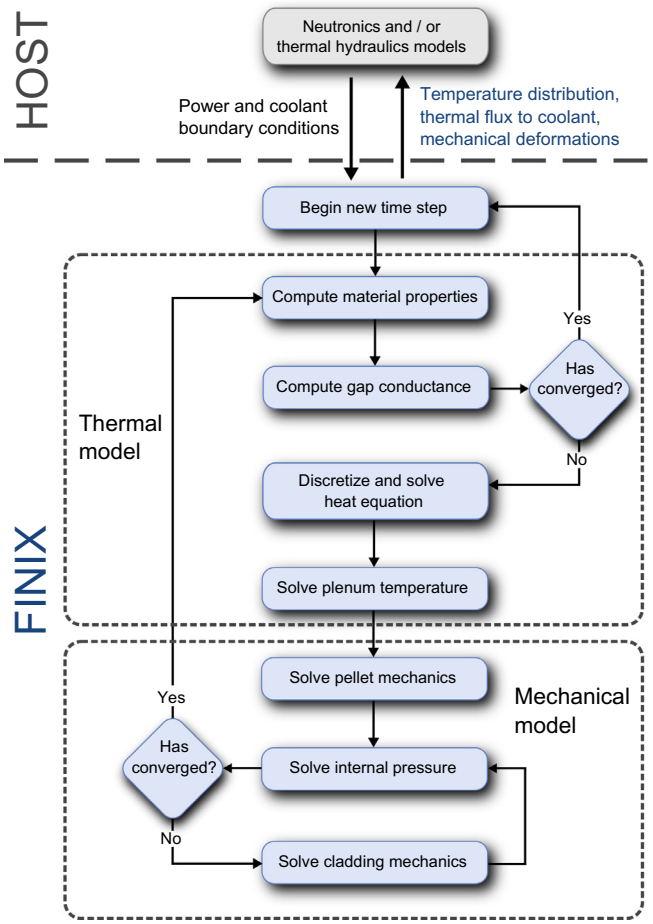

Fig. 1. Schematic illustration of the FINIX module and its role in a multiphysics simulation. The iteration of the thermal and mechanical solutions is indicated by the flowchart. The convergence checks are assumed to automatically fail on the first iteration.

transient should be obtained in a different way. This is discussed in Section 2.7.

In the interest of readability, the following model description is kept brief, with the focus on the models' assumptions, approximations, and the limitations they imply. The detailed formulae can be found in the provided references, or in the FINIX code description (Ikonen, 2013).

2.3. Thermal model

The temperature distribution inside the pellet and in the cladding is obtained by solving the one dimensional radial heat equation,

$$C_V(T)\frac{\partial T}{\partial r} - \frac{1}{r}\frac{\partial}{\partial r}\left[\lambda(T) r \frac{\partial T}{\partial r}\right] = s(r), \tag{1}$$

independently for each axial node. Here C_V is the volumetric heat capacity, λ is the heat conductivity and s is the thermal power density. The temperature $T = T(r,t)$ is solved using linear finite element discretization in space and implicit finite difference discretization in time, along with appropriate boundary conditions at the pellet-cladding gap and at the cladding outer surface. The former is formulated via the gap conductance calculated by FINIX. For the latter, the user can select the desired form of the boundary condition from (i) the cladding surface temperature, (ii) outward heat flux, or the bulk coolant temperature with the heat transfer coefficient either (iii) as a user-given value or, (iv) calculated from internal FINIX correlations (cf. Section 2.6).

The gap conductance model of FINIX includes contributions from radiative heat transfer, the conductivity of the fill gas and the (possible) solid–solid contact: $h_{\mathrm{gap}} = h_{\mathrm{rad}} + h_{\mathrm{cond}} + h_{\mathrm{contact}}$. The individual terms are calculated from correlations similar to the FRAPTRAN code (Geelhood et al., 2011b), with the exception of the cladding emissivity correlation that is similar to the implementation of FEMAXI (Suzuki and Saitou, 2006). In addition, the conductivity term h_{cond} can be calculated by either the FRAPCON or FRAPTRAN correlation, with the FRAPTRAN correlation as the default option. In contrast to FRAPTRAN, the radial pellet relocation is calculated at each time step as given in Section 2.5. The effect of gas composition on the conductivity is taken into account. Finally, the contact term h_{contact} is coupled with the cladding mechanical solution.

The plenum temperature is calculated by assuming steady state heat transfer between the fill gas and the plenum walls. For the plenum, correlations for pure helium are used (Petersen, 1970). In the steady state this simplification affects the balance between the cladding and pellet radiative transfer in only a minor way.

Because the material parameters in Eq. (1) and the gap conductance depend on the temperature, the heat equation has to be solved iteratively. A combination of the bisection and secant method similar to the Dekker method is used for this iteration (Press et al., 2002). For each iteration the mechanical model, described below, is also solved, to give the pressure and the heat conductance in the gap. The iteration procedure is illustrated in Fig. 1.

2.4. Mechanical model

The mechanical module of FINIX consists of models for the rod internal pressure, pellet deformations and cladding deformations.

The internal pressure is calculated by assuming equal gas pressure throughout the rod, taking into account the volumes and temperatures of the plenum, pellet-cladding gap and the optional pellet central hole for each axial node. The pressure calculation also couples together the otherwise independent mechanical and thermal solutions at the various axial locations.

The fuel pellet is modeled as a rigid axisymmetric pellet that is undeformable by external stresses, similar to the FRACAS-I model in FRAPCON and FRAPTRAN (Geelhood et al., 2011a,b). Strains due to thermal expansion and radial relocation are taken into account. The cladding is modeled as an axisymmetric, thin-walled cylinder, assuming negligible bending in the axial direction. FINIX calculates elastic and thermal deformations by assuming mechanical equilibrium, iterating the solution until the rod internal pressure converges (see Fig. 1). Plastic and creep deformations can be given as input, but their values are not updated in the current model. Upon sufficiently strong solid contact, the deformations of the cladding are determined by deformations of the (rigid) pellet.

2.5. Material correlations

FINIX uses publicly available correlations to describe the dependence of various material properties on quantities such as temperature, burn-up, chemical composition, etc. Since the number of different correlations is large and they are publicly available, the formulae are not reproduced here. The detailed descriptions are available in the FINIX code description (Ikonen, 2013).

The fuel properties described by correlations are the specific heat, thermal conductivity and thermal strain. These are modeled using FRAPTRAN correlations (Geelhood et al., 2011a; Geelhood et al., 2011b; Luscher and Geelhood, 2011). The correlations are applicable to UOX and MOX fuels. Similarly for the cladding, the thermal properties as well as the mechanical correlations for Meyer's hardness, Young's modulus and Poisson's ratio are given by (Geelhood et al., 2011a; Geelhood et al., 2011b; Luscher and Geelhood, 2011). The current correlations are only applicable to Zircaloy claddings, but correlations for other materials are simple to implement.

Pellet radial relocation is given as the fractional closure of the gap in relation to the as-fabricated gap G as

$$\frac{\Delta G}{G} = \begin{cases} 0.15 + 0.05f, & LHR \leqslant 20\ \frac{\mathrm{kW}}{\mathrm{m}}, \\ 0.14 + 0.06f + 0.5(1+g)f, & 20\ \frac{\mathrm{kW}}{\mathrm{m}} < LHR < 40\ \frac{\mathrm{kW}}{\mathrm{m}}, \\ 0.16 + 0.09f, & LHR \geqslant 40\ \frac{\mathrm{kW}}{\mathrm{m}}, \end{cases} \tag{2}$$

where $f \equiv f(Bu) = Bu/5$ for $Bu < 5$ MWd/kgU and $f(Bu) = 1$ otherwise, and $g \equiv g(LHR) = 0.0025(LHR - 20)$, with the linear hear rate LHR given in kW/m and the burnup Bu in MWd/kgU. The difference between the FINIX correlation and the model presented by Geelhood et al. (2011a) is that by default, only the mechanical (hard) relocation is taken into account in FINIX. This results in better agreement with experimental data (Loukusa, 2013). The calculation of the reduction in thermal gap width (soft relocation) is optional in FINIX.

2.6. Coolant model

FINIX also has a simple model to calculate the heat transfer coefficients between the cladding and the coolant. In the model, the coolant bulk temperature is assumed given at the location of each axial node. The heat transfer coefficients are calculated using the Dittus-Boelter correlation for single-phase convection and Thom correlation for nucleate boiling, after Geelhood et al. (2011a,b). The range of validity is checked by calculating the critical heat flux from the EPRI correlation (Reddy and Fighetti, 1983). Required coolant properties such as bulk fluid enthalpy, saturated liquid enthalpy, and vaporization enthalpy are also calculated using simple internal correlations (Ikonen, 2013). The current version of FINIX does not have stand-alone capabilities for analyses beyond the film boiling regime. Integration with a thermal

hydraulic code is intended for more advanced modeling of the thermal hydraulic properties.

2.7. Burnup effects

As prolonged irradiation takes place, the nuclear fuel rod experiences significant changes in fuel composition, the dimensions of the pellet and the cladding, and gap conductance. Simulating a transient occurring with a non-fresh fuel requires knowledge of the effects that have occurred post fabrication. A conventional way of taking them into account is to simulate the preceding irradiation history with a fuel performance code. This kind of simulation requires dedicated models on fuel swelling, fission gas release, cladding creep, and so on. The present version of FINIX does not have the capability to simulate these phenomena by itself. However, the results can be given to FINIX as an input. For example, with the FRAPCON code one can simulate the steady state irradiation and write the post irradiation state of the fuel rod into a restart file, which FINIX can read in directly using one of its input modules.

Sometimes it is not possible to use a fuel performance code to calculate the initial state for the transient. This may be due to computation time constraints, lack of detailed irradiation history, or simply because a steady-state fuel performance code is not available for the user. For these situations, it is convenient to acquire an approximation of the initial state by using simple correlations based on approximate irradiation history. For FINIX, such an initialization method using correlations fitted to a statistically sampled steady state irradiation data is under development (Ikonen et al., 2013; Syrjälahti, 2011, 2012), and will be reported in its entirety in future work.

3. Verification and validation of stand-alone FINIX

Arguably the most important quantity that a fuel performance module calculates in a coupled multiphysics simulation is the time-dependent temperature distribution in the pellet and in the cladding. This is especially true in coupled neutronics simulations, where the fuel temperature determines the reactivity change due to Doppler broadening. Also in thermal hydraulics simulations, the temperature distribution directly affects the heat flux from the cladding to the coolant.

The temperature calculation of FINIX has been compared against both the FRAPTRAN-1.4 fuel performance code and experimental data from Halden IFA-429 and IFA-432 test series (IFPE database, 1997, 1996). The former involves code-to-code comparisons with similar inputs, and is useful in verifying FINIX's overall behavior in the tested scenarios. In these comparisons, one can look at any calculated quantities, including gap conductance, pressure, mechanical deformations, and so on. The comparison with experimental data, on the other hand, is limited to quantities that have been measured in the experiment. However, the comparison is truly quantitative and reveals the model's accuracy with respect to real-world data. In this work, we constrain our comparison to the centerline temperature data measured in IFA-429 and IFA-432 experiments.

3.1. Comparison with experimental Halden data

The FINIX code has been compared against experimental centerline temperature data from five rods: rod BC of experiment IFA-429 and rods 1, 2, 3, and 5 from IFA-432. These are steady-state irradiation experiments, where, depending on the test, the rod was irradiated up to a burnup of more than 50 MWd/kgUO_2. Simulating the irradiation with FINIX is technically possible, but the accuracy of the results diminishes at increasing burnup because several phenomena are neglected. However, restricted to moderate burnups the comparison is still a good check of FINIX's integral performance and, at higher burnups gives an approximate measure of the expected error due to the lacking steady-state models.

A comparison between centerline temperatures measured in the test IFA-429 and calculated by FINIX is shown in Fig. 2. At low burnup, up to approximately 10 MWd/kgUO_2, the match between the experimental and simulated values is extremely good. At increasing burnup, the accuracy decreases due to fuel swelling, inward cladding creep and fission gas release. Even for high burnups, the error is still quite manageable at approximately ±100 K.

The results for all the considered rods in tests IFA-429 and IFA-432 are collected in Fig. 3. The experimental results are fairly well predicted, with most of the data predicted within ±200 K. The spread is also quite symmetric, although there are clear differences between individual rods. Among the used data set, FINIX does have a small bias towards underpredicting the temperatures. However, considering the experimental uncertainties, the match is quite good.

3.2. Comparison with FRAPTRAN

In the FINIX code verification effort, several RIA scenarios were simulated and compared with FRAPTRAN-1.4 simulations (Loukusa, 2013). Here we present results from two such scenarios. In both cases, the initial state of the transient was determined by a simulation with FRAPCON-3.4. The code inputs were obtained from the FRAPCON/FRAPTRAN User Group (FRAPCON/FRAPTRAN Users Group, 2011). The comparison of FINIX and FRAPTRAN with fresh fuel has already been discussed by Ikonen et al. (2013). Thus the present work only considers irradiated fuel.

FINIX and FRAPTRAN are compared both in cases where the cladding deforms only elastically and in cases where there are significant plastic deformations. For the first case, we have calculated the CABRI REP-Na4 scenario (Papin et al., 2003), in which a reconditioned rodlet from EDF with Zircalloy-4 cladding, base irradiated at Gravelines-5, underwent a power transient with a pulse width of 76.4 ms in sodium coolant at 0.5 MPa and 280 °C. The rod did not fail during the test. For this scenario, FRAPTRAN calculates negligible plastic deformation.

The calculated temperatures are shown in Fig. 4. The codes match each others' results very closely, with a maximum difference of some tens of degrees in the fuel centerline temperature, and considerably less elsewhere. The gap conductance is also closely matched, as shown in Fig. 5. The internal pressure calculated by FINIX is consistently higher by 10–20% (see right panel of Fig. 5). The difference is due to different initialization of the

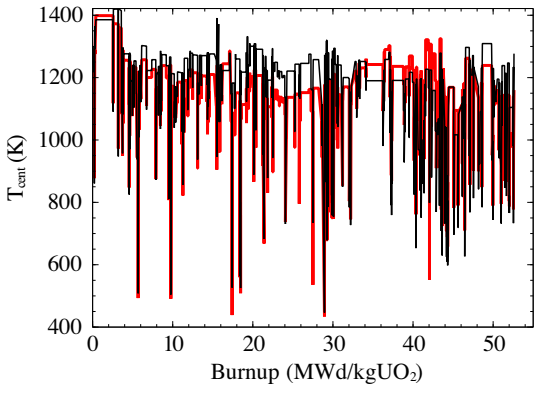

Fig. 2. Fuel centerline temperatures as a function of burnup for the IFA-429 experiment rod BC as calculated by FINIX (black line) and as measured in the experiment (thick red line). (For interpretation of the references to color in this figure legend, the reader is referred to the web version of this article.)

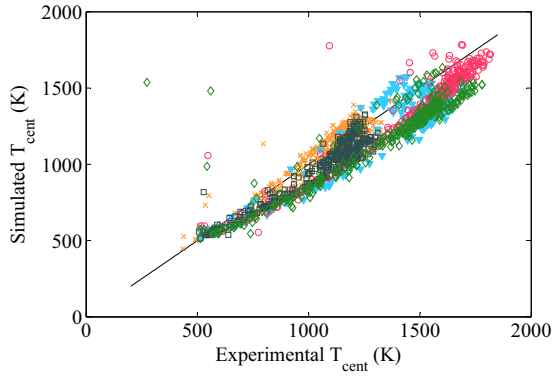

Fig. 3. Measured vs. calculated fuel centerline temperatures from the IFA-429 and IFA-432 test series. Different symbols correspond to different rods. ▼: IFA-432 rod 1, ◯: IFA-432 rod 2, □: IFA-432 rod 3, ◇: IFA-432 rod 5, ×: IFA-429 rod BC.

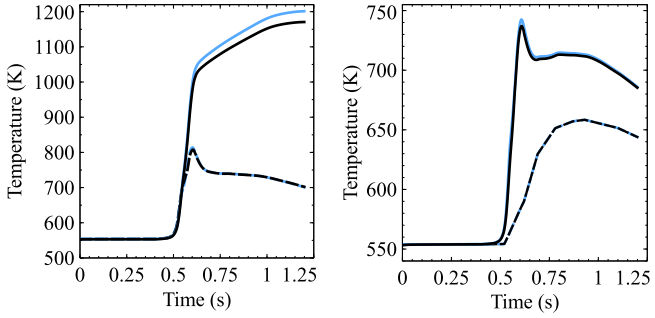

Fig. 4. Temperatures in the fuel (left panel) and cladding (right panel) for the CABRI REP-Na4 scenario as a function of time calculated by FINIX (black lines) and FRAPTRAN (blue curves). Left panel: Fuel centerline temperatures (solid lines) and outer surface temperatures (dashed line). Right panel: Clad inner surface temperatures (solid lines) and outer surface temperatures (dashed lines). (For interpretation of the references to color in this figure legend, the reader is referred to the web version of this article.)

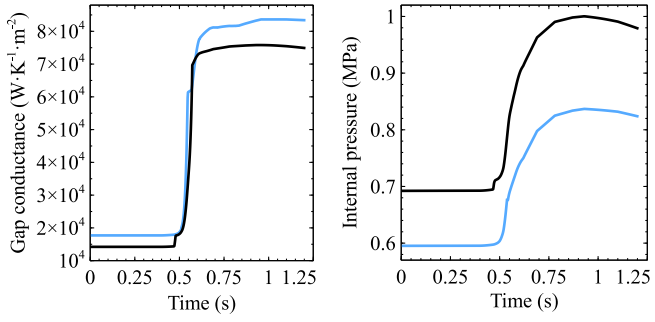

Fig. 5. Gap conductance (left panel) and rod internal pressure (right panel) for the CABRI REP-Na4 scenario as a function of time calculated by FINIX (black lines) and FRAPTRAN (blue curves). (For interpretation of the references to color in this figure legend, the reader is referred to the web version of this article.)

plenum volume for irradiated fuel in FINIX and FRAPTRAN (Loukusa, 2013).

The scenario CABRI REP-Na3 (Papin et al., 2003) was also studied. This scenario was otherwise similar to the CABRI REP-Na4 scenario, except that the rod was a segment from EDF with low tin Zircalloy-4 cladding and the power pulse width was 9.5 ms. In this case, FRAPTRAN calculates significant plastic deformation for the cladding, which influences the gap width and conductivity.

The temperatures for FINIX and FRAPTRAN simulations of the CABRI REP-Na3 scenario are shown in Fig. 6. Also in this case, the results are very similar. This is despite the differences in the gap

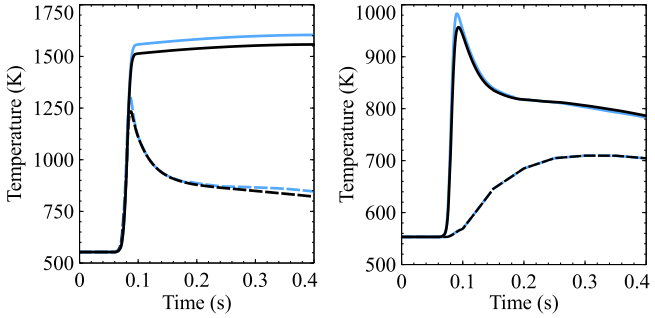

Fig. 6. Temperatures in the fuel (left panel) and cladding (right panel) for the CABRI REP-Na3 scenario as a function of time calculated by FINIX and FRAPTRAN. Conventions as in Fig. 4.

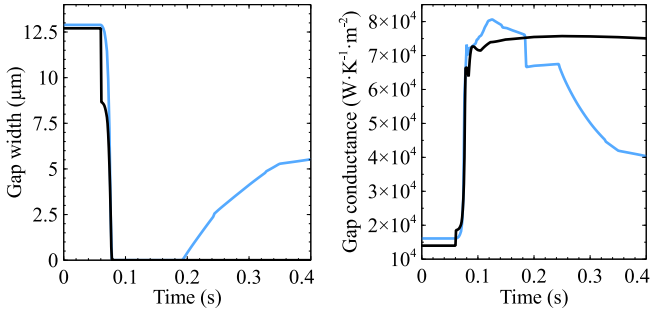

Fig. 7. Gap width (left panel) and conductance (right panel) for the CABRI REP-Na3 scenario as a function of time calculated by FINIX (black lines) and FRAPTRAN (blue curves). (For interpretation of the references to color in this figure legend, the reader is referred to the web version of this article.)

width and gap conductance solutions (see Fig. 7), which are due to plastic deformations. FINIX does not model plastic evolution of the cladding and the gap remains closed, whereas FRAPTRAN predicts gap opening after 190 ms. Re-opening of the gap is also reflected in the gap conductance. The overall effect on the temperature distribution is small, although towards the end of the scenario, a slightly larger temperature difference across the gap is seen in the FRAPTRAN solution (see Fig. 6).

In addition to the two scenarios described above, several other reactivity transients have been simulated and compared by Loukusa (2013). In some of the scenarios FRAPTRAN predicts rod failure. Currently FINIX does not have criteria for rod failure and therefore these scenarios cannot be directly compared. However, up until the time of failure, the codes perform very similarly for all quantities. After the failure, quantities such as pressure are of course very different, but temperature distributions are remarkably alike. Although the rod failure is not predicted, the agreement is encouraging for the use of the fuel module even in more extreme scenarios.

Apart from reactivity initiated accidents, another major application of transient fuel performance codes is the simulation of loss-of-coolant accidents (LOCAs). LOCA simulations require advanced descriptions of phenomena occurring at large overpressure and high cladding temperature, including plastic deformations, creep, and oxidation. For FINIX, implementation of these models is part of work to be reported separately in the future.

4. Integration with Serpent 2

4.1. Background

FINIX has been integrated to Serpent 2, a 3D continuous-energy Monte Carlo reactor physics burnup calculation code developed at

VTT Technical Research Centre of Finland (Leppänen, 2007). The development of Serpent 2 has a major focus on multi-physics applications. A universal multi-physics interface for code coupling is complemented with new methodology for the treatment of continuous temperature (Viitanen and Leppänen, 2012; Viitanen and Leppänen, 2014a; Viitanen and Leppänen, 2014b) and density (Leppänen, 2013b) distributions. The recently implemented time dependent simulation mode (Leppänen, 2013a) extends the applications of Serpent 2 even further. For further information on recent multi-physics advances in Serpent 2 see (Leppänen et al., 2014).

4.2. Implementation

Serpent 2 and FINIX are coupled at the source code level. Serpent is responsible for solving the power distribution in the system while FINIX models the thermal and mechanical response of the fuel rod. The solution transfer between FINIX and the neutron transport part of Serpent are handled by a set of internal routines that form the fuel behavior multi-physics interface in Serpent 2. The fission power in fuel rod is tallied by Serpent and provided to FINIX nodes while conserving the total power generation as well as the local power generation in the node volume. The temperature solution calculated by FINIX can be used in Serpent as is with linear interpolation between the node points, without any mesh transformation. The changes in geometry obtained by FINIX can also be used in the neutron tracking without any transformation.

The multi-physics routines in Serpent 2 provide the neutron transport routines with the correct temperature and density distributions at different points in time and space so that the effect of the realistic temperature and density distributions can be accounted for in the interaction physics. The data transfer between Serpent and FINIX is done internally without disk operations.

The time-dependent coupled solution is obtained by a sequential and iterative solving of the fission power distribution by Serpent and the temperature and strain distributions by FINIX. At the beginning of the dynamic simulation a steady state solution of the fuel behavior is calculated to be used on the first time step. At the first iteration of a time step the temperature and strain distributions are taken from the previous step and at the later iterations they are interpolated between the beginning of step (BOS) and end of step (EOS) distributions yielding a semi-implicit scheme. First the neutronics solution is obtained for the new time interval, after which the temperature distribution at the end of the interval is calculated by FINIX. A convergence criterion is applied after this and if the convergence of the coupled solution is not deemed sufficient, the neutronics solution for the next iteration is obtained.

4.3. Effect on Serpent 2 calculations

Combining Serpent 2 with FINIX allows the simultaneous and self consistent solving of the fission power and the fuel behavior of the system. This makes it possible to account for and quantitatively estimate coupled problems such as the effects of thermal–mechanical feedbacks in steady-state criticality calculations as well as their effect on nuclide production and transmutation during fuel life. Another important topic is the analysis of transient scenarios with coupled tools. The coupled multi-physics solution offers a method for improving the best-estimate solutions in many cases.

The recently developed dynamic simulation mode in Serpent 2 allows time dependent simulation of neutrons in sub-critical, critical as well as super-critical configurations. Time dependent modeling of super-critical configurations allows Serpent 2 to calculate the neutronics in reactivity insertion transients. However, a solo Serpent simulation does not consider any feedback effects, causing the neutron population and power in super-critical systems to increase without a limit. Combining time dependent fuel behavior analysis provided by FINIX to the time dependent simulation mode in Serpent, a prompt critical reactivity insertion accident can be modeled from the initial perturbation to the shutdown of the transient by the fuel temperature effects (mainly increased resonance absorption due to Doppler broadening of the resonance cross sections) as described in the following sections.

4.4. Simulation of a coupled fast transient

4.4.1. Description

Steady state simulations with coupled Serpent and FINIX have been discussed previously by Ikonen et al. (2013). To demonstrate the fast transient capabilities of coupled FINIX and Serpent, we simulate a test case where the reactivity of the system is suddenly increased by reduction in boron concentration. This leads to exponential increase in power until it is terminated by the negative reactivity feedback from the increasing fuel temperature.

The test geometry is a two dimensional PWR pin-cell with Three Mile Island Unit 1 (TMI-1) parameters (Blyth et al., 2012). The pellet radius was 0.4695 cm, the cladding inner radius was 0.4791 cm and the outer radius was 0.5464 cm. Coolant temperature was set to a constant 500 K with a coolant density of 748 kg/m^3. The axial length of the rod in the FINIX model was 1 m.

The fuel pellet had a realistic radial burnup profile for 8.84 MWd/kgU (Fig. 8 left) that was calculated beforehand with Serpent. The initial conditions are hot full power (233 W/cm) with the radial power profile shown in Fig. 8. (right). The system is held critical by soluble absorber in the coolant. To onset the transient, the boron concentration in the coolant is suddenly reduced from 970 ppm to 860 ppm yielding an instantaneous reactivity insertion of 1865 pcm. From this moment on, the response of the system is calculated solely by Serpent 2 and FINIX, i.e., the size and the shape of the power pulse is not known beforehand.

The simulation consisted of 1000 time-intervals of 20 μs resulting in a total of 20 ms of simulated time. The fuel behavior was solved after each time interval, and the transport solution was repeated if the temperature solution failed a pointwise convergence test of 3.0 K. The temperatures at interaction points were interpolated between the beginning of interval and the predicted end of interval distributions. If a timestep had to be iterated more than once, the calculated power distribution was averaged between the iterations. The FINIX geometry model consisted of one fuel rod with a single axial zone, 101 nodes in the pellet and 51 in the cladding. The fission power was tallied in Serpent in 20 radial zones of equal volume. Equal timestep size of 20 μs was used in FINIX and Serpent, although different timestep sizes can also be used. Delayed neutron emission was switched off in Serpent. Since

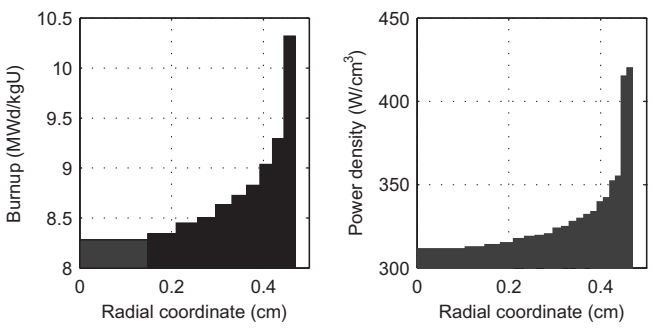

Fig. 8. Radial burnup distribution (left panel) for the fuel pellet in the Serpent-FINIX calculation and the resulting radial power density distribution (right panel) at the onset of the transient.

the shortest precursor half-lives are in the range of 50–100 ms, this approximation is not believed to have significant effect on the results.

4.4.2. Results

The calculation was run on 12 Intel Xeon X5690 cores with one OMP-thread per core. The calculation took 12 wall-clock-days. Modeling super prompt critical systems with Monte Carlo neutronics is computationally intensive and practically all of the time was spent by neutron tracking in Serpent.

The evolution of the system linear power is shown in Fig. 9 (left panel). Without the feedback from FINIX the power calculated by Serpent would increase exponentially without limit (red line). However, due to the two-way coupling between Serpent 2 and FINIX a finite power peak is obtained from the coupled calculation (black line). The fuel temperature calculated by FINIX based on the power calculated by Serpent is supplied back to Serpent. This means that increase in power increases the fuel temperature, which in turn increases the loss of neutrons to resonance absorption. This slows down the increase of fission power at first, and finally makes the system sub-critical again resulting in the decrease of the linear power and shutting down of the transient as expected.

While the quantitative modeling of the power pulse based on only the initial conditions of the system is a novel feature for Serpent in itself, the coupled calculation also provides information on parameters important for safety considerations such as maximum cladding and fuel temperatures during the transient. Some of the parameters of interest are shown in the Figs. 9–11. The parameters shown include the fuel pellet surface and centerline temperatures, gas gap width and cladding temperature. The exact values of these parameters are not very relevant due to the simplistic nature of the calculation scenario, but the fact that their time evolution can be obtained from these calculations is interesting.

The rate of heat transfer from the pellet to coolant is another interesting aspect of the solution. The fuel rod's gas gap closes at 6.82 ms. After the closing of the gap, the expanding pellet starts to push the cladding further outwards. The closing of the gap also increases heat transfer from the pellet to the cladding, which can be seen in the pellet surface temperature (right panel of Fig. 9). During the next part of the transient, the heat starts to arrive to the cladding surface raising its temperature (right panel of Fig. 10). The heat flux to coolant increases with the increasing temperature difference between the cladding and coolant as well as the increasing heat transfer area. The last phase of the transient sees the cladding outer temperature passing the critical temperature of the coolant and thus the beginning of nucleate boiling leading to a steeper increase in the heat flux to coolant.

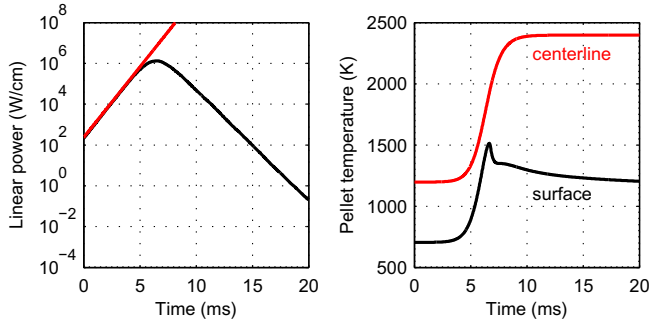

Fig. 9. System linear power (left panel) with no-feedback prediction (red line) and pellet surface temperature (right panel) as a function of time for the coupled transient calculated by Serpent 2 and FINIX. (For interpretation of the references to color in this figure legend, the reader is referred to the web version of this article.)

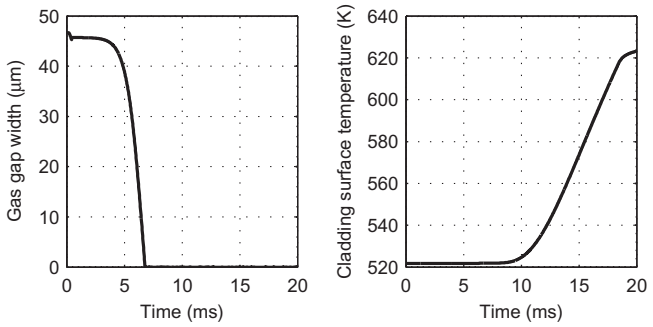

Fig. 10. Gas gap width (left panel) and cladding surface temperature (right panel) as a function of time for the coupled transient calculated by Serpent 2 and FINIX.

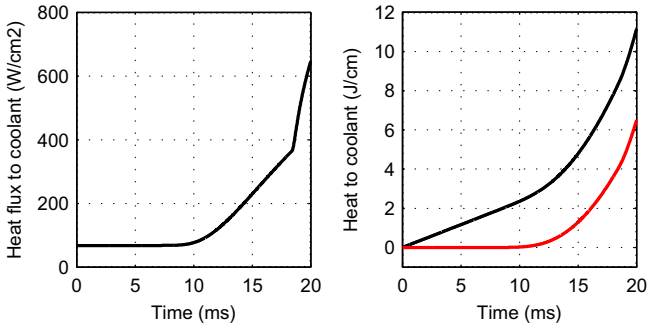

Fig. 11. Heat flux to coolant (left panel) and in the right panel the cumulative total heat transferred to coolant (black line) and the cumulative extra heat transferred to the coolant (red line) as a function of time for the coupled transient calculated by Serpent 2 and FINIX. (For interpretation of the references to color in this figure legend, the reader is referred to the web version of this article.)

Multiplying the heat flux with the heat transfer surface area and integrating with respect to time yields the cumulative amount of the heat transferred to coolant during the transient (black line in the right panel of Fig. 11). Subtracting the baseline steady-state heat transfer of 233 W/cm one can obtain the amount of *additional* heat transferred to the coolant during the transient (red line). The additional heating of 6.58 J/cm is not expected to have a large enough effect on the coolant temperature to be significant for the neutronics. However, the simulation of longer transients requires calculating and updating the coolant temperature distribution as well.

This simple test case shows, on the methodology level, that the coupling with FINIX extends the capabilities of Serpent 2 to calculating the power pulse shape and magnitude from known initial conditions in reactivity insertion accidents. The calculation also yields information on important safety parameters such as maximum fuel and cladding temperatures as well as the heat flux to coolant. Application of the code system to real safety analysis, of course, requires considerable validation, verification and testing in more realistic scenarios.

5. Integration with TRAB3D and TRAB-1D

5.1. TRAB3D, TRAB-1D and SMABRE codes

FINIX has also been integrated with the reactor dynamics code TRAB3D (Kaloinen and Kyrki-Rajamäki, 1997) that is a coupled neutronics-thermal–hydraulics code developed at VTT for transient and accident analysis of boiling water reactors (BWRs) and pressurized water reactors (PWRs). In addition to the core, the code includes models for the cooling circuit of BWRs.

TRAB3D solves the two-group neutron diffusion equations with a nodal expansion method in a rectangular fuel assembly geometry. Thermal–hydraulics of the reactor core is solved in separate one-dimensional hydraulic channels, which can be further divided into axial sub-regions. Usually each channel is coupled with one fuel assembly. Parallel to the heated channels, several unheated by-pass channels can be modeled. Channel hydraulics is based on conservation equations for steam and water mass, total enthalpy and total momentum, and on a selection of optional correlations. During the hydraulics iterations, a one-dimensional heat transfer calculation is done for an average fuel rod of each assembly. TRAB3D solves heat transfer in a fuel rod from one-dimensional axially uncoupled equations using theta method for time discretization. Heat capacity of pellet and cladding and conductivity of the cladding are given in input with temperature dependent correlations, whereas heat conductivity of a pellet depends also on burnup. Conductance of the gas gap is in practice always modeled using linear interpolation from simple temperature dependent table. It is possible to define several fuel rod types in TRAB3D and provide separate values for each fuel rod type. In practice lack of proper data diminish reliability and feasibility of this kind of approach.

The PWR circuit can be modeled with the thermal–hydraulic code SMABRE (Miettinen and Hämäläinen, 2000), which models 3D thermal hydraulic effects using parallel channel nodalization combined with the turbulent mixing model. SMABRE contains a five-equation two-phase thermal hydraulic model, using the drift flux model. There is a parallel coupling between the circuit model SMABRE and TRAB3D (Daavittila et al., 2000). SMABRE calculates the whole thermal hydraulics of the loops and the core in a sparse geometry. TRAB3D performs the detailed thermal hydraulics and fuel heat transfer calculation in every fuel assembly of the core to get the nodal fuel and coolant conditions for the calculation of three-dimensional neutron kinetics and reactivity feedback effects. In the combined code, the interchanged variables between modules are the nodewise power to coolant from TRAB3D to SMABRE, and core inlet and outlet pressure, mass flow, fluid enthalpy and inlet boron concentration for each core sector from SMABRE to TRAB3D.

TRAB-1D (Rajamäki, 1976) is the one-dimensional predecessor of TRAB3D. Nowadays it is used mainly for separate hot channel analyses without coupling with neutronics. In hot channel analyses, node powers and thermal hydraulics conditions calculated e.g. by TRAB3D in advance are used as boundary conditions for TRAB-1D. TRAB-1D's own fuel rod models are identical to TRAB3D's models.

5.2. Implementation of the FINIX coupling

In the new coupling with FINIX, TRAB3D's own fuel heat transfer solution can be replaced with the FINIX module. The choice between FINIX and TRAB3D's own models is done in the TRAB3D input.

TRAB3D solves power distribution in the reactor core and distribution is transferred to the FINIX module. Also the bulk coolant temperature and the heat transfer coefficient between the cladding outer surface and the coolant are calculated in TRAB3D and are used as boundary conditions for the FINIX module. FINIX calculation is done for one average fuel rod of each fuel assembly, in total 150–500 fuel rods depending on the reactor type. TRAB3D controls the data for each fuel rod and calls FINIX consecutively with the current state parameters of one fuel rod. FINIX returns the temperature distribution of the fuel rod for neutronics calculation and other data that has to be stored for the next time step. Deformation of a fuel rod is taken into account in the heat transfer solution but at the moment deformation is ignored in the flow channel modeling. Same axial discretization is used in FINIX and in TRAB3D. Typically number of axial levels is from 20 to 40. Radially typically from 6 to 10 nodes are used for the pellet and one node for the cladding. The same time step is used in FINIX and TRAB3D.

FINIX is coupled to TRAB-1D in the same way as to TRAB3D. Fuel rod discretization is defined in the same way as in TRAB3D, but in TRAB-1D only one fuel rod is modeled.

5.3. TRAB-1D results

Coupling of FINIX and TRAB-1D has been used for separate core channel calculations with given boundary conditions to test heat transfer in the fuel rod without feedback to neutronics. Here we present TRAB-1D results from the artificial power peak transient in a PWR fuel rod.

In the power peak transient a PWR fuel rod has been modeled using 40 axial nodes. Radially 7 mesh points were used in the fuel pellet and 2 in the cladding. FINIX calculations were done assuming fresh fuel and a burnup of 50 MWd/kgU. For high burn-up, two cases were assumed for radial heat generation in the fuel pellet: uniform heat generation and non-uniform, in which heat generation increases outwards in the pellet as shown in Fig. 12. TRAB-1D and TRAB3D have burnup-dependent models for radial heat generation, and used model parameters are based on an earlier study (Syrjälahti, 2000). In this calculation, burnup only affects the heat conductivity of the fuel, with other effects to be considered in future work. Reference calculations were done using TRAB-1D's own heat transfer model with heat capacities and conductivities used in TMI MSLB benchmark. These correlations do not have burnup dependence.

At the initial state the rod has very low power, 1.5 W/cm^3. After 1 s, power generation in the fuel rod increases for 0.1 s, and after that drops in 0.1 s to the original value. Axial power distribution and thermal hydraulic boundary conditions at the channel inlet do not change during the transient. Maximum fuel centerline temperature and the average node powers are shown in Fig. 12. It should be noted that due to the non-uniform radial power distribution, at the beginning of the transient the rod maximum temperatures are in fact obtained near the pellet surface instead of the centerline, as can be seen in Fig. 13. Temperature during the power transient is higher with stand-alone TRAB3D correlations. The flat radial power distribution increases maximum centerline temperatures with both models. With FINIX the temperature decreases more slowly, and even more so if burnup is taken into account in the FINIX calculation due to the reduced thermal conductivity of the fuel.

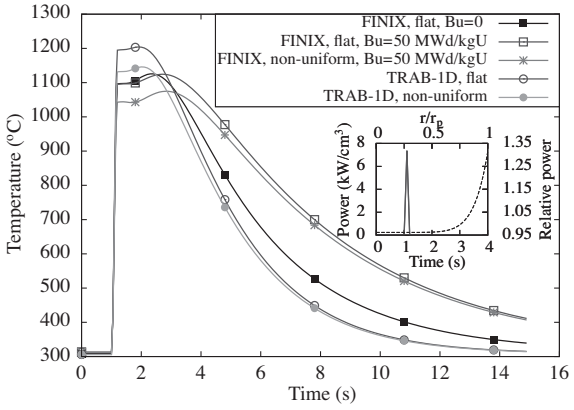

Fig. 12. Maximum fuel centerline temperature during power peak transient with TRAB-1D. Inset: the average power density during the transient (solid) and radial heat generation in the fuel pellet as a function of radius (dashed), r = radius, r_p = pellet outer radius.

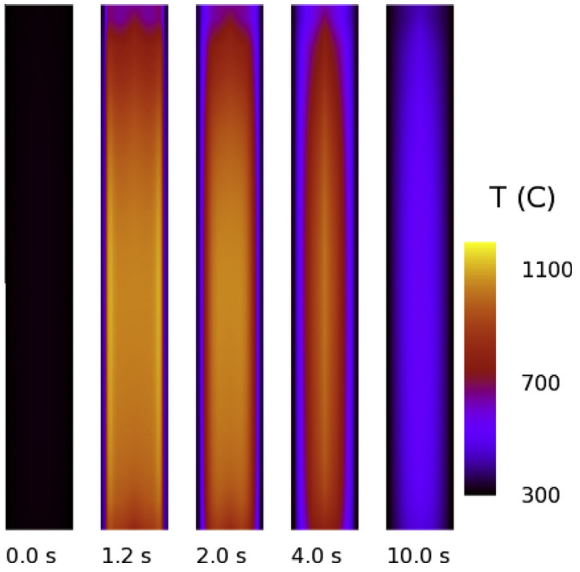

Fig. 13. Temperature distribution in the fuel rod during the power peak transient using FINIX with TRAB-1D. Non-uniform radial heat generation, burnup 50 MWd/kgU.

5.4. TRAB3D/SMABRE results

Several types of transients and plants have been simulated with TRAB3D using the FINIX module (Syrjälahti, 2013). Here we present TRAB3D/SMABRE results from PWR main steam line break (MSLB) benchmark transient using TMI-1 as the reference plant (Ivanov et al., 1999). OECD/NEA organized this benchmark in 1999–2000 and VTT participated in the benchmark with TRAB3D-SMABRE code (Daavittila et al., 2003).

In the MSLB benchmark problem, the TMI-1 PWR plant with two coolant loops was modeled. In the initial state, the reactor is assumed to be at the end-of-cycle and at full power. The initiating event of the transient is the steam-line break in one loop, which results in a rapid drop of steam line pressure, leading to the decrease of the water temperature in the primary side. This temperature decrease causes reactor power to increase. When the core reaches 114% flux level, the reactor is automatically tripped. The characterizing feature of MSLB event is the asymmetric cooling in the primary side. The asymmetry is further enhanced by assuming one stuck control rod situated in the colder core half. In the benchmark two scenarios were specified: one with realistic cross sections and other with reduced control rod worths to achieve a return-to-power situation. Here results with the latter cross section set are presented.

The transient was calculated with TRAB3D/SMABRE using the FINIX module. All 177 fuel assemblies were modeled, each of them in its own flow channel. Burnup was not taken into account in the heat transfer calculation. Time-step length varied during the simulation from 0.02 s to 0.1 s. Needed calculation time was less than 1700 s on one Intel Xeon X5450 processor. As a reference, the event was calculated using the original temperature-dependent pellet and cladding heat capacities and conductivities specified for the benchmark. Gas gap conductance was specified to have the constant value $h_{gap} = 11.356\ \mathrm{kW/m^2K}$. For comparison, the event was also calculated using 20% variations for the gas gap conductance. Calculation was repeated also with FINIX coupling using that constant gas gap conductance.

The fission power during the scenario is shown in Fig. 14. Although the difference in power between the TRAB3D and the coupled TRAB3D-FINIX solutions is small, the effect of more

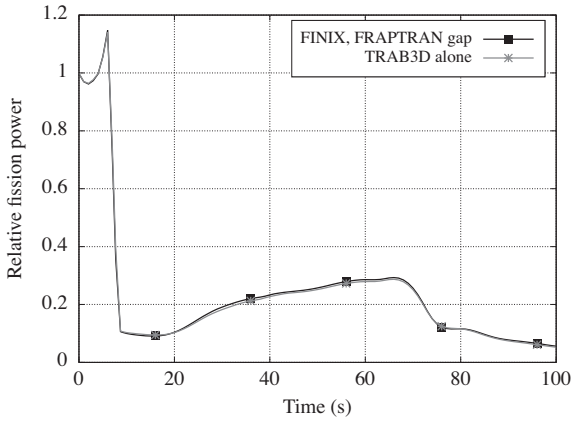

Fig. 14. Fission power in TMI MSLB benchmark as a function of time.

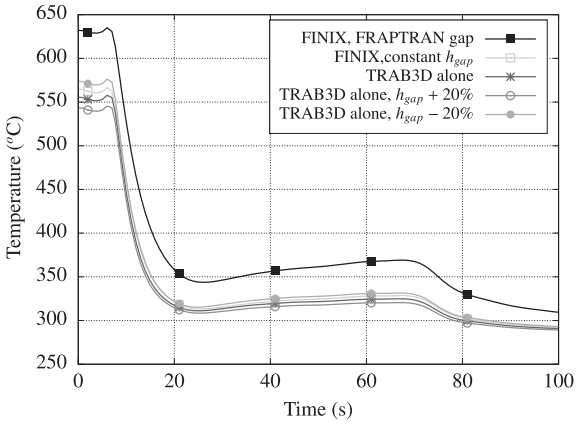

Fig. 15. Average fuel temperature with different fuel rod models in the TMI MSLB benchmark.

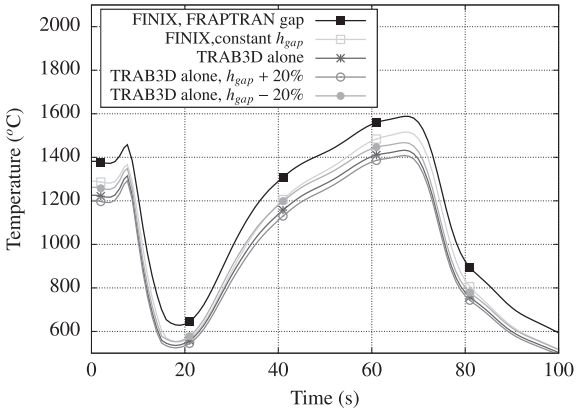

Fig. 16. Maximum fuel centerline temperature with different fuel rod models in the TMI MSLB benchmark.

detailed modeling of the fuel rod can be seen in the temperature distributions. Initial fuel temperatures computed by FINIX are higher than with the benchmark correlations (cf. Figs. 15 and 16) mainly due to the different gas gap conductance, and the difference in temperatures remains during the transient. Due to the slow transient there are no remarkable differences in the temperature distributions inside the fuel rod (cf. Fig. 17). Gas gap conductance,

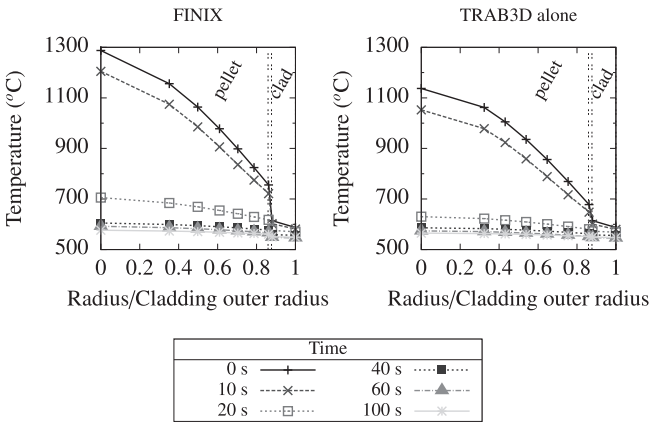

Fig. 17. Radial temperature distribution at axial level 20/24 of the fuel rod at certain time steps in TMI MSLB benchmark.

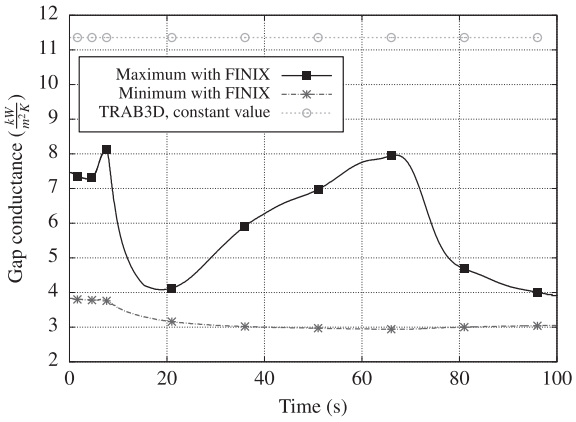

Fig. 18. Gap conductance with different fuel rod models in the TMI MSLB benchmark.

h_{gap}, computed by FINIX with the FRAPTRAN gap model, varied during the transient from 2.9 kW/m^{2}K to 8.1 kW/m^{2}K (see Fig. 18). Gas gap remains open in all fuel rods during the whole transient, as illustrated in Fig. 19.

In this case only the submitted simulation results were available as reference, and they were all calculated with same specified fuel properties (Todorova et al., 2003). Also in other simulations with different types of transients FINIX gives higher temperatures than these public benchmark correlations, but results in a, for example, EPR control rod ejection transient indicate that FINIX results are closer to fuel specific correlations (Syrjälahti, 2013). This TMI MSLB benchmark shows that FINIX can be used as a thermo-mechanical model in whole core transient calculations, in which a large number of fuel rods with different properties and different dynamical behavior are modeled.

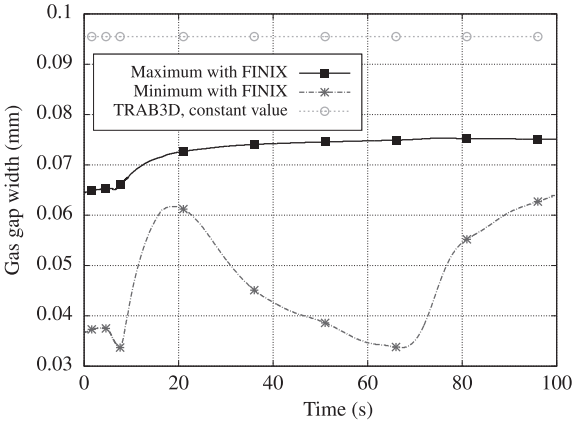

Fig. 19. Width of the gas gap with different fuel rod models in the TMI MSLB benchmark.

6. Conclusions and outlook

A light-weight fuel behavior module FINIX has been developed. FINIX is aimed especially for multiphysics simulations, where it takes the role of the simulation's fuel behavior model. FINIX has been designed to be integrated into a wide array of simulation codes, and to provide an identical description of the fuel thermal behavior across different disciplines such as reactor physics and thermal hydraulics. In cases where the role of fuel performance simulations has been taken by simple correlations and thermal elements, calculation of the thermal response can be significantly improved by including mechanical feedback and power history dependence. Towards such a goal, we use FINIX to simulate the transient thermal and mechanical behavior of the rod, and show that FINIX can be used to provide improved estimates for the rod's thermal behavior in multiphysics simulations.

FINIX models have been validated against experimental centerline temperature data and verified against FRAPTRAN-1.4 simulations of several RIA experiments. The comparison shows good performance, especially for the calculation of the temperature distribution. For the temperatures, the agreement with FRAPTRAN remain good even when significant plastic deformations are predicted by FRAPTRAN, despite FINIX's lack of nonelastic models for the cladding. However, to extend FINIX's validity to simulation of steady state irradiation or loss of coolant accidents (LOCA), improvements such as fission gas modeling, cladding creep, and plastic deformations are required.

To demonstrate the applicability of FINIX to multiphysics simulations, we have integrated FINIX to Serpent 2, a Monte Carlo reactor physics code, and to TRAB3D and TRAB-1D, VTT's in-house reactor dynamics codes. With Serpent, we model a test case of an initially supercritical PWR pin-cell, where the exponential increase of power is terminated by the negative reactivity feedback from the increasing fuel temperature. With TRAB-1D, an artificial power peak without neutronics feedback is modeled, revealing the difference between the temperatures calculated by FINIX and simple benchmark correlations. With TRAB3D, a main steam line break of the Three Mile Island Unit 1 is simulated, combining neutronics, thermal hydraulics and fuel performance simulations. The case involves running multiple (several hundred) instances of FINIX in one simulation, and showcases how FINIX can be used to model the fuel thermal behavior of a whole reactor.

Development of the FINIX module is an on-going work. Future work follows two parallel paths, with the first focusing on improving the fuel performance capabilities in LOCAs and in steady state, and the second concentrating on developing methods for uncertainty propagation and system initialization with incomplete information. The aim of both is in keeping with FINIX's general goal to enhance the accessibility and reliability of fuel performance modeling in multiphysics simulations.

Acknowledgments

This work was funded by SAFIR2014, the Finnish Research Programme on Nuclear Power Plant Safety 2011–2014.

References

Bailly, H., Menessier, D., Prunier, C. (Eds.), 1999. The Nuclear Fuel of Pressurized Water Reactors and Fast Neutron Reactors. Lavoisier Publishing.

Blyth, T., Avramova, M., Ivanov, K., Royer, E., Sartori, E., Cabellos, O., 2012. Benchmark of Uncertainty Analysis in Modeling (UAM) for Design, Operation and Safety Analysis of LWRs, Volume II: Specification and Support Data for the Core Cases (Phase II) [draft version 1.0], Technical Report NEA/NSC/DOC(2012)?, Nuclear Energy Agency.

Cacuci, D. (Ed.), 2010. Handbook of Nuclear Engineering. Springer.

Daavittila, A., Hämäläinen, A., Kyrki-Rajamäki, R., 2000. Application of TRAB-3D to BWR and PWR transient calculations. In: FINNUS Interim Report 1999–2000, Technical Research Centre of Finland VTT, pp. 150–160.

Daavittila, A., Hämäläinen, A., Kyrki-Rajamäki, R., 2003. Effects of secondary circuit modeling on results of PWR MSLB benchmark calculations with new coupled code TRAB-3D/SMABRE. Nucl. Technol. 142 (2), 116–123.

FRAPCON/FRAPTRAN Users Group, 2011. FRAPTRAN RIA Assessment Cases. http://frapcon.labworks.org/fraptran_assess/RIA.html. Updated 18-AUG-2011.

Geelhood, K., Luscher, W., Beyer, C, 2011a. FRAPCON-3.4: A Computer Code for the Calculation of Steady-state Thermal–Mechanical Behavior of Oxide Fuel Rods for High Burnup. Technical Report NUREG-CR-7022, vol. 1, Pacific Northwest National Laboratory.

Geelhood, K., Luscher, W., Beyer, C., Cuta, J., 2011b. FRAPTRAN 1.4: A Computer Code for the Transient Analysis of Oxide Fuel Rods, Technical Report NUREG-CR-7023, vol. 1, Pacific Northwest National Laboratory.

Hämäläinen, A., Stengård, J.O., Miettinen, J., Kyrki-Rajamäki, R., Valtonen, K., 2001. Coupled Code FRAPTRAN-GENFLO for analysing fuel behaviour during PWR and BWR transients and accidents. In: IAEA Technical Committee Meeting on Fuel Behavior under Transient and LOCA Conditions (IAEA-TECDOC-1320). Halden, Norway 10–14 September 2001, p. 43.

IFPE database, 1996. NEA IFPE/IFA-432 Experimental Data, Updated 29-JAN-1996.

IFPE database, 1997. NEA IFPE/IFA-429 Experimental Data. 1997. Updated 12-NOV-1997.

Ikonen, T., 2013. FINIX Fuel Behavior Model and Interface for Multiphysics Applications. Code Documentation for Version 0.13.9. Technical Report VTT-R-06563-13; VTT Technical Research Centre of Finland.

Ikonen, T., Tulkki, V., Syrjälahti, E., Valtavirta, V., Leppänen, J., 2013. FINIX – fuel behavior model and interface for multiphysics applications. In: 2013 Fuel Performance Meeting/TopFuel, Charlotte, USA.

ISL Inc., 2010. RELAP5/MOD3.3 Code Manual Volume I: Code Structure, System Models, and Solution Methods, Technical Report NUREG-CR-5535 Rev 4, vol. 1, Information Systems Laboratories, Inc.

Ivanov, K., Beam, T., Baratta, A., Irani, A., Trikorous, N., 1999. PWR MSLB Benchmark: Volume 1: Final Specifications. Technical Report NEA/NSC/DOC/(99)8; OECD/NEA.

Kaloinen, E., Kyrki-Rajamäki, R. TRAB-3D, 1997. A new code for three-dimensional reactor dynamics. In: CD-ROM Proceedings of ICONE-5, 5th International Conference on Nuclear Engineering. Nuclear Advances through Global Cooperation, Nice, France.

Lamarsh, J.R., 1966. Introduction to Nuclear Reactor Theory. Addison-Wesley.

Lassmann, K., 1992. Transuranus: a fuel rod analysis code ready for use. J. Nucl. Mater. 188, 295.

Leppänen, J., 2007. Development of a New Monte Carlo Reactor Physics Code. Ph.D. Thesis. Helsinki University of Technology.

Leppänen, J., 2013a. Development of a dynamic simulation mode in serpent 2 Monte Carlo code. In: M&C 2013, Sun Valley, ID.

Leppänen, J., 2013b. Modeling of nonuniform density distributions in the serpent 2 Monte Carlo code. Nucl. Sci. Eng. 174, 318.

Leppänen, J., Hovi, V., Ikonen, T., Kurki, J., Pusa, M., Valtavirta, V., Viitanen, T., 2014. The Numerical Multi-physics Project (NUMPS) at VTT Technical Research Centre of Finland, Annals of Nuclear Energy 2014, Submitted to this Volume.

Loukusa, H, 2013. Validation of the FINIX Fuel Behavior Code Version 0.13.9. Technical Report VTT-R-06565-13, VTT Technical Research Centre of Finland.

Luscher, W., Geelhood, K., 2011. Material Property Correlations: Comparisons Between FRAPCON-3.4, FRAPTRAN 1.4, and MATPRO. Technical Report NUREG-CR-7024, Pacific Northwest National Laboratory.

Miettinen, J., Hämäläinen, A., 2000. Development and validation of the fast running thermohydraulic model smabre for simulator purposes. ICONE-8: Eight International Conference on Nuclear Engineering Baltimore, USA, 2–6 April, 2000 [CD-ROM] New York: American Society of Mechanical Engineers Paper ICONE8-8188, 12 p ISBN 0791819922 2000.

Papin, J., Cazalis, B., Frizonnet, J.M., Fédérici, E., Lemoine, F., 2003. Synthesis of CABRI-RIA tests interpretation. In: The Eurosafe Forum, Paris, France.

Petersen, H., 1970. The Properties of Helium: Density, Specific Heats, Viscosity, and Thermal Conductivity at Pressures from 1 to 100 bar and From Room Temperature to About 1800 K, Technical Report RISO-224, Danish Atomic Energy Commission Research Establishment Risö.

Press, W., Teukolsky, S., Vetterling, W., Flannery, B., 2002. Numerical Recipes in C, 2nd Edition. Cambridge University Press.

Rajamäki, M., 1976. TRAB, A Transient Analysis Program for BWR. Technical Report 24, Technical Research Centre of Finland, Nuclear Engineering Laboratory.

Reddy, D., Fighetti, C., 1983. Parametric Study of CHF Data. Volume 2. A Generalized Subchannel CHF Correlation for PWR and BWR Fuel Assemblies. Final Report. Technical Report EPRI-NP-2069-Vol. 2, Columbia Univ., New York (USA). Dept. of Chemical Engineering.

Rohde, U., 2001. The modeling of fuel rod behaviour under RIA conditions in the code DYN3D. Ann. Nucl. Energy 28, 1343.

Rossiter, G., 2011. Development of the ENIGMA fuel performance code for whole core analysis and dry storage assessments. Nucl. Eng. Technol. 43, 489.

Suzuki, M., Saitou, H., 2006. Light Water Reactor Fuel Analysis Code FEMAXI-6 (Ver.1) – Detailed Structure and User's Manual. Japan Atomic Energy Agency.

Syrjälahti, E., 2000. Modelling of the Gas Gap and Radial Heat Generation in the Fuel Pellet in the Reactor Dynamics Code TRAB, Technical Report VTT Energy Reports 16/2000, VTT Technical Research Center of Finland.

Syrjälahti, E., 2011. Characterization of a Representative VVER-440 Fuel Rod with the Statistical ENIGMA, Technical Report VTT-R-08464-11, VTT Technical Research Center of Finland.

Syrjälahti, E., 2012. Characterization of a representative VVER-440 fuel rod with the statistical ENIGMA. In: 22nd Symposium of AER, Prunonice, Czech Republic, Oct. 1–5, 2012, Atomic Energy Research (AER).

Syrjälahti, E., 2013. Coupling of the FINIX Fuel Module to the Reactor Dynamics Codes TRAB3D and TRAB-CORE, Technical Report VTT-R-08967-13, VTT Technical Research Center of Finland.

Todorova, N., Ivanov, K., Taylor, B., 2003. PWR MSLB Benchmark: Volume IV Results of Phase III on Coupled Core-plant Transient Modelling, Technical Report NEA/NSC/DOC/(2003)21; OECD/NEA.

Viitanen, T., Leppänen, J., 2012. Explicit treatment of thermal motion in continuous-energy Monte Carlo tracking routines. Nucl. Sci. Eng. 171, 165–173.

Viitanen, T., Leppänen, J., 2014a. Target motion sampling temperature treatment technique with elevated basis cross section temperatures. Nucl. Sci. Eng. 177, 77–89.

Viitanen, T., Leppänen, J., 2014b. Temperature majorant cross sections in Monte Carlo neutron tracking. Nucl. Sci. Eng. (in press).

Williamson, R.L., Hales, J.D., Novascone, S.R., Tonks, M.R., Gaston, D.R., Permann, C.J., Andrs, D., Martineau, R.C., 2012. Multidimensional multiphysics simulation of nuclear fuel behavior. J. Nucl. Mater. 423, 149.

PUBLICATION III

Modeling of Zircaloy cladding primary creep during load drop and reversal

Journal of Nuclear Materials, **445**, 98–103.

Journal of Nuclear Materials 445 (2014) 98–103

Contents lists available at ScienceDirect

Journal of Nuclear Materials

journal homepage: www.elsevier.com/locate/jnucmat

Modeling of Zircaloy cladding primary creep during load drop and reversal

V. Tulkki *, T. Ikonen

VTT Technical Research Centre of Finland, P.O. Box 1000, 02044 VTT, Finland

ARTICLE INFO

Article history:
Received 6 September 2013
Accepted 26 October 2013
Available online 5 November 2013

ABSTRACT

Modeling fuel behavior requires an accurate description of the cladding stress response for both operational and safety considerations. The transient creep response of Zirconium alloys is commonly modeled using a strain hardening rule which is known to hold in cases with monotonously increasing stresses. However, the strain hardening rule is experimentally known to fail in scenarios such as load drop or reversal.

In this paper we derive a simple and easily implementable set of rules for primary creep based on experimental results which contradict the strain hardening rule. The primary creep predicted by these rules is compared with data from published thermal creep experiments and Halden in-pile creep experiment IFA-585. The model thus created is shown to perform well in describing both transient stress scenarios with monotonously increasing stress and scenarios involving load drops and reversals.

1. Introduction

The cladding of a fuel rod contains the radioactive fission products produced during the time the rod is in the reactor. During its reactor life the cladding tube is under a pressure differential at elevated temperatures and under irradiation. These conditions cause the cladding to creep, first inwards as the reactor system pressure exceeds the fuel internal pressure, and then outwards as the expanding pellet pushes the cladding. The reactor operation causes additional alternating stresses, to which the cladding must conform. At high burnup the rod internal overpressure may even push the cladding to creep faster than the fuel pellet swells, potentially creating a self-reinforcing cladding lift-off effect [1] which may lead to fuel failure. It is therefore important to be able to describe the creep behavior of the cladding adequately.

Conventionally creep is described by having three regions: the primary (or transient) region, the secondary steady state region and the third leading to failure. As the fuel rods stay in the reactor only for limited time, most of the models used describe the first two regions. The extension to the rupture becomes important in studies such as spent fuel behavior in interim dry storage conditions, which is outside the scope of this work. The correlations are matched to experiments with a single stress increase, and the change of stress encountered in fuel behavior analysis is handled by hardening laws. Typically the creep in metals follows either a time or a strain hardening law, and the latter is usually assumed to hold for Zirconium alloys in usual operating conditions [2].

Various creep correlations have been formulated over the years that take both thermal and irradiation creep into account. It is well known that the hardening laws used to take the transient conditions into account are simplifications and do not apply universally. Stress reversal and stress reduction are special situations where the hardening laws fail. These situations have been successfully described with complex formulations of cladding material thermodynamic states [3,4] and by assuming additional deformation terms such as reversible anelastic deformation [5,6]. While these formulations appear to provide correct prediction of the cladding creep behavior they are not commonly implemented in fuel behavior codes due to their complexity. Fuel behavior analysis is commonly performed with integral codes utilizing separate models to describe various phenomena, and the number of required simulations may rise to hundreds of thousands of fuel rod simulations depending on the application [7,8]. For this purpose, a simple and more practical approach is needed.

In this paper we present a simple primary creep formulation to describe cladding creep response to transient stresses based on previously published experimental data [9,10]. The resulting model is both able to handle the situations where strain hardening law fails as well as to closely replicate strain hardening in situations where it has been experimentally shown to hold.

The structure of the paper is as follows. In Section 2, we discuss the experimental basis for the current creep modeling and derive the new model based on the experimental results. The model is verified against experimental data in Section 3 and the results of the paper are summarized in Section 4.

* Corresponding author. Tel.: +358 20 722 6114; fax: +358 20 722 7001.
E-mail address: ville.tulkki@vtt.fi (V. Tulkki).

0022-3115/$ - see front matter © 2013 Elsevier B.V. All rights reserved.
http://dx.doi.org/10.1016/j.jnucmat.2013.10.053

2. Theory

2.1. Background

While the creep of Zircaloy alloys has been studied extensively (e.g. Refs. [11–20]), only a few published experiments have concentrated on the response to complex transients. According to investigations of Lucas and Pelloux [2] the thermal creep deformation at temperatures below 375 °C can be described by a strain hardening rule. In strain hardening it is assumed that the creep response always follows a curve as seen in single stress level experiments and the changing stress state is taken into account by moving to the new stress/strain curve to the point where accumulated strain is retained. This work is used as a justification for the use of the strain hardening rule in most of the models [10,15,21]. Matsuo investigated thermal creep of Zircaloy-4 [12] and formulated a correlation, which Limbäck and Andersson extended to reactor conditions [21].

Murty and Yoon investigated strain transients following stress changes [5] and proposed a creep model which assumes an anelastic strain component in addition to the traditional elastic and plastic contributions. This aneslastic component is used to succesfully explain the observed accumulation of reverse strain at load drop, while the traditional plastic contribution from creep is assumed to follow the strain hardening rule. Matsuo also investigated the creep behavior of Zircaloy under variable conditions [10] and formulated a set of rules for stress reversal situations based on reversible creep hardening surfaces.

A common assumption in the creep models utilized in the integral fuel behavior codes is that the creep strain ϵ can be divided into two parts, primary ϵ_p and secondary ϵ_s:

$$\epsilon = \epsilon_p + \epsilon_s. \tag{1}$$

The secondary steady state part usually consists of thermal and irradiation creep contributions ($\dot{\epsilon}_s = \dot{\epsilon}_{th} + \dot{\epsilon}_{irr}$), such as in the fuel performance code FRAPCON-3.4's correlation [22–24] which is effectively the model by Limbäck and Andersson [21] modified to use effective stress σ_{eff} instead of hoop stress:

$$\dot{\epsilon}_{th} = A\frac{E}{T}\left(\sinh\frac{a_i\sigma_{\text{eff}}}{E}\right)^n e^{-\frac{Q}{RT}} \quad \text{and} \tag{2}$$

$$\dot{\epsilon}_{irr} = C_0 \cdot \phi^{C_1} \cdot \sigma_{\text{eff}}^{C_2} \cdot f(T), \tag{3}$$

where E is the elastic modulus, T is temperature in K, R is the universal gas constant, Q the activation energy of the creep, ϕ the fast neutron flux (n/m^2 s^{-1}). The variables $A,\ a_i,\ n,\ C_i$ and the function $f(T)$ have different values depending on the cladding type and the environment as described in Ref. [24]. The use of σ_{eff}

$$\sigma_{\text{eff}} = \sqrt{0.5((\sigma_a - \sigma_h)^2 + (\sigma_h - \sigma_r)^2 + (\sigma_r - \sigma_a)^2)}, \tag{4}$$

is justified by an improved modeling of tensile and compressive creeps [24]. Here $\sigma_{a,h,r}$ denote stresses in axial, hoop and radial directions and isotropic behavior is assumed for simplicity.

Limbäck and Andersson assume that the form of the primary creep is similar to the one proposed by Matsuo [12], in particular of the form

$$\epsilon_p = \epsilon_p^S(1 - e^{f(\dot{\epsilon}_s t)}), \quad \text{and} \tag{5}$$

$$\epsilon_p^S = B \cdot \dot{\epsilon}_s^b, \tag{6}$$

where the saturated primary creep ϵ_p^S is related to secondary creep rate with constants B and b, and the time for primary creep to saturate is a function $f(\dot{\epsilon}_s t)$ of the secondary creep rate. The transient stress is taken into account by assuming a strain hardening rule.

However, these models are contradicted by the results of the Halden in-pile creep experiment IFA-585 [9]. According to the experiment it would appear that the primary creep depends on the direction of stress change while the secondary creep rate depends on the stress level. This is in contrast to the model of Eq. (6) which assumes that the magnitude of saturated primary creep is proportional to the secondary creep rate.

2.2. Formulation of new creep correlation

In this work we focus on the response to transient stresses. The model for the primary creep $\epsilon_p(t)$ is derived on a phenomenological basis, most importantly requiring consistency with the experimental results reported for IFA-585 [9,25]. According to the experiment, the total saturated primary creep is proportional to the change in the applied stress. The primary creep strain due to one stress change can then be approximately described by a function of the form

$$\epsilon_p(t) = C(\sigma_1 - \sigma_0)\left(1 - e^{-\frac{t-t_0}{\tau}}\right), \tag{7}$$

where C is a constant, σ_0 and σ_1 are the initial and final externally applied stresses, respectively, t_0 is the time when the change of stress from its initial to final value occurs, and τ is the characteristic time scale of the primary creep.

To utilize the experimental results (Eq. (7)) in a practical scenario with several sequential stress changes, one needs a way to keep record of the stress history of the system. In response to the changing stress, the material evolves through a complex set of internal states, with $\epsilon_p(t)$ slowly approaching the saturation value. We propose that to reproduce the behavior of Eq. (7), it is sufficient to characterize the internal state of the system by a single time-dependent stress-like variable, $\sigma_{int}(t)$. The time evolution of σ_{int} describes the relaxation of the internal state of the system towards the steady state determined by the externally applied stress. We choose the scale of σ_{int} so that for an initial state with zero primary creep rate and the applied stress is equal to $\sigma_0, \sigma_{int}(t = t_0) = \sigma_0$. As the applied stress is changed to σ_1, the variable σ_{int} starts to evolve in time, approaching the new steady state value $\sigma_{int}(t \to \infty) = \sigma_1$, which is reached when the primary creep has fully saturated.

In order to find the time evolution of $\sigma_{int}(t)$ at intermediate times, we make an *ansatz* of a simple linear response, so that the strain rate is given by

$$\frac{d\epsilon_p(t)}{dt} = D(\sigma_1 - \sigma_{int}(t)). \tag{8}$$

Thus, the relaxation of σ_{int} towards the saturation value σ_1 ultimately determines the rate of primary creep. In the conventional approach, one would determine $\sigma_{int}(t)$ using thermodynamics or microscopic arguments, and use a relation such as Eq. (8) to derive the primary creep strain as a function of time. However, in deriving the phenomenological model, we take the reverse approach. We require that the experimental result of Eq. (7) holds for $\epsilon_p(t)$ and use Eq. (8) to derive $\sigma_{int}(t)$. The result is

$$\sigma_{int}(t) = \sigma_1 - (\sigma_1 - \sigma_0)e^{-\frac{t-t_0}{\tau}}, \tag{9}$$

also fixing the constant $D = C/\tau$ in Eq. (8).

Eqs. (7) and (9) can be cast in a form that has no explicit dependence on the initial values σ_0 and t_0. If the strain and internal stress have known values $\epsilon_p(t)$ and $\sigma_{int}(t)$ at time t, the corresponding values at time $t + \Delta t$ are given by

$$\epsilon_p(t + \Delta t) = \epsilon_p(t) + C(\sigma_{ext} - \sigma_{int}(t))(1 - e^{-\frac{\Delta t}{\tau}}), \tag{10}$$

$$\sigma_{int}(t + \Delta t) = (\sigma_{int}(t) - \sigma_{ext})e^{-\frac{\Delta t}{\tau}} + \sigma_{ext}, \tag{11}$$

where the notation σ_{ext} has been used for the externally applied stress (σ_1). Eqs. (10) and (11), together with the initial conditions $\sigma_{int}(t_0) = \sigma_0$ and $\epsilon_p(t_0) = 0$, constitute the phenomenological creep model.

By keeping record of the time evolution of the system's internal state via σ_{int}, the model can take into account fast consecutive stress changes, even when the primary creep does not saturate between them. It is also easy to verify that Eq. (7) is recovered in the limit of a single stress change from σ_0 to σ_1. From the practical point of view, it is important that written in the form of Eqs. (10) and (11), the model only requires knowledge of σ_{int} at the previous time step to calculate the incremental ϵ_p, making its implementation into a fuel performance code straightforward. Also note that Eqs. (10) and (11) are exact, although they have the appearance of a finite difference approximation.

The variables C and τ of Eqs. (10) and (11) depend on both manufacturing properties of the cladding materials and the environment (temperature, neutron flux, etc.). A complete creep correlation would require determination of these dependencies with well characterized materials [12,21]. However, this is out of the scope of this paper, where our aim is to demonstrate the applicability of the new hardening rule in principle. As it is, we consider both C and τ as parameters to be determined from experimental data.

2.3. Mechanical analogue

In addition to creep, a system has an elastic response to external stress. Including the elastic strain ϵ_{el} in Eq. (1), the total strain due to external stress can be written as

$$\epsilon = \epsilon_{el} + \epsilon_p + \epsilon_s. \tag{12}$$

In Eq. (12), the primary creep ϵ_p has a saturation value, while the secondary creep is assumed to grow without limit under applied stress. Such a system can be approximately described by a mechanical analogue displayed in Fig. 1. The springs A and B are elastic components whose displacement $\epsilon_{\text{spring}} = \sigma/\kappa_i$, where κ_i is the elastic modulus of spring i and σ is the external stress affecting the given component, while the dashpots C, D and E represent viscous elements with a rate of displacement of $\dot{\epsilon}_{\text{dashpot}} = \sigma/\eta_i$, where η_i is the viscosity of the dashpot i. The nodes A, B and C create a model known as standard linear solid (SLS) model which is commonly used in viscoelastic studies due to its ability to describing both creep and relaxation behavior of many materials [26]. The SLS part in this analoge models the elastic response and the primary creep, and the twin dashpots D and E the thermal and irradiation steady state creep.

The solution to SLS is well known [26], and the solution of the whole system with the dashpots D and E in a series is obtained by simple addition. The solution to the strain as a function of applied stress $\sigma(t)$ is of the form

$$\epsilon(t) - \epsilon(0) = \frac{\sigma(t) - \sigma(0)}{\kappa} + \int_0^t C\left(1 - e^{-\xi/\tau}\right)\frac{d\sigma(\xi)}{d\xi}d\xi + \left(\frac{1}{\eta_D} + \frac{1}{\eta_E}\right)\int_0^t \sigma(\xi)d\xi, \tag{13}$$

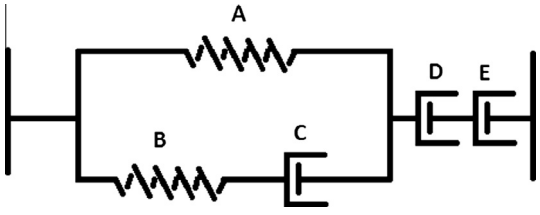

Fig. 1. Mechanical analogue for the proposed creep model.

with the constants κ, C and τ being functions of κ_i and η_C. The first term corresponds to the elastic strain, the second to primary creep, and the last one to secondary creep (both thermal and irradiation induced).

In the case of an instantaneous stress change from σ_0 to σ_1 at time $t = t_0$, the derivative $d\sigma(t)/dt = (\sigma_1 - \sigma_0)\delta(t - t_0)$, with δ the Dirac delta distribution, Eq. (13) reduces to Eq. (7) for the primary creep. For several stepwise changes, Eqs. (10) and (11) can be recovered. In addition, the response to a more general change in stress can be solved from Eq. (13). Thus, while the primary creep model was derived from an experimental basis, it also has a direct mechanical analogue that is easy to interpret and whose mathematical properties are well known.

3. Experimental verification

The primary creep formulation was tested against published sets of variable stress data. First, we show the model behavior against the Zircaloy-2 BWR rod of IFA-585 Halden experiment [9] whose results were the basis of the model formulation. The amount of published in-pile creep experiments with on-line monitoring is scarce, and therefore the second set was chosen to be the experiments on Zircaloy-4 samples by Matsuo [12]. Due to the different experimental setups (different materials, in-pile and out-of-pile experiment) different creep correlations were used for the two sets. For analysis of the Matsuo's out-of-pile tests the secondary creep part was modeled after the correlation by Matsuo [12]:

$$\epsilon_s = 1.57 \times 10^{13}\frac{E}{T}\left(\sinh\frac{1.13 \times 10^3 \sigma_h}{E}\right)^{2.1} e^{-\frac{2.72\times10^5}{RT}}, \tag{14}$$

where elastic modulus $E = 1.148 \times 10^5 - 59.9T$ MPa. For the in-pile IFA-585 the secondary creep was modeled as per FRAPCON-3.4's modified Limbäck and Andersson model of Eqs. (2) and (3) with the variables set as described in Ref. [24] for RXA cladding. Eqs. (10) and (11) were used for primary creep with values of σ_{int}, C and τ described in the following subsections.

3.1. Halden in-pile experiment IFA-585

The OECD/NEA IFPE data for IFA-585 experiment [27] was used for the in-pile experiment. In the IFA-585 experiment a pre-irradiated BWR cladding tube was pressurized to several stress states, both compressive and tensile, while under irradiation in the Halden research reactor. The cladding deformation was measured with on-line diameter gauges which were calibrated to unpressurized reference diameters on the end plugs. There was also a composite PWR rod in the test but as the diameter measurements were reported [28] to be anomalous relatively early on in the experiment we focus on the BWR sample in this paper.

The BWR rod sample was irradiated prior to the Halden experiment in a commercial reactor to a fast neutron dose of 6×10^{21} n/cm^2. Also, during the first experimental cycle there were issues with rod pressurization which are not included in the analysis. For the simulations shown here it has been assumed that $\sigma_{int} = -52$ MPa at $t = 0$, which was the planned effective stress on the cladding in the initial cycle. The value of $C = 1.92 \times 10^{-6}$ m^2/N is as per Ref. [9] and $\tau = 100$ h was chosen by fitting to the data.

There are uncertainties in the test results [29], especially related to the effect of the different rates of oxide layer growth between the sample and the end plugs and experimentally derived secondary creep rate [25]. In the following the simulated secondary creep rate is altered by the same amount as the experimental measurement is reported to be affected by the differential in the oxide layer growth rates [25]. For secondary creep it has been

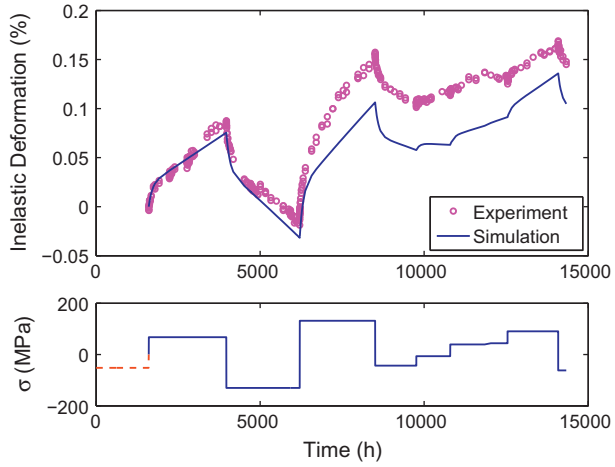

Fig. 2. IFA-585 BWR experiment (circles) and simulated behavior (line). The applied stress history is displayed in the bottom plot.

noted that IFA-585 experiment features very high secondary creep rates [25] compared to other creep experiments such as those of Ref. [15]. This was also seen in the initial analysis. The FRAPCON correlation used for secondary creep rate was multiplied by a factor of 2 in order to better match the experimental results. Neither of these two uncertainties should change the interpretation of the behavior of the primary creep.

The comparison between the simulated and measured inelastic deformation, along with the applied effective stress for IFA-585 experiment, is shown in Fig. 2. The mid-wall effective stress with positive values signifying tension and negative values compression is also shown in Fig. 2. The match between the experiment and the simulation is good, especially at the beginning of the experiment. However, errors mostly due to the uncertainties in the secondary creep rate compound during the simulation. In Fig. 3 only the initial inelastic deformation after each stress step is shown and the plotting of the deformation at the beginning of each stress step is shifted to zero. The results show excellent agreement between the simulated and measured behavior. Thus it can be argued that the error seen in Fig. 2 is mostly due to the uncertainty in the secondary creep rate, and that the creep response to stress reversal can be modeled using the Eqs. (10) and (11).

3.2. Matsuo's out-of-pile experiments

For examining the Matsuo's out-of-pile tests the experimental data points were extracted from Figs. 3, 4, 7 and 9 of Ref. [10]. The data details creep behavior during load increase from 77.9 MPa to 148.1 MPa of tensile hoop stress, load drop from 156.9 MPa to 74.3 MPa of tensile hoop stress and two series of load reversal steps alternating between tensile hoop stress of 148 MPa and compressive hoop stress of 78 MPa. Cladding temperature during these tests was 662.9–664.0 K. Matsuo uses cladding tube hoop stress in his analysis and correlations, and thus hoop stress instead of effective stress is used when analyzing these experiments. The tests are pressurized tube tests with biaxial stress condition $\sigma_a/\sigma_h = 1/2$ [10] yielding $\sigma_{\text{eff}} = \sqrt{3}/2\sigma_h$ according to Eq. (4). The difference between using hoop and effective stress in analyzing the primary creep behavior in this experimental arrangement is seen only in the value of the parameter C.

For Matsuo's experiments the fitting parameters were set as $C = 3.8 \times 10^{-5}$ m^2/N and $\tau = 40$ h. For the simulations shown here it has been assumed that $\sigma_{int} = 0$ at $t = 0$. Also, an improved match to the results was gained by multiplying Eq. (14) by a factor of 1.25. The results are shown in Figs. 4–7 as the *baseline* line. While for

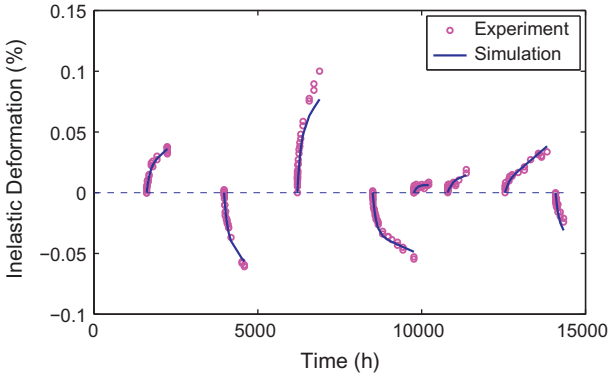

Fig. 3. The model behavior against measurements for the beginning of each stress step. The plots start at $\epsilon = 0$ at the beginning of each pressure step.

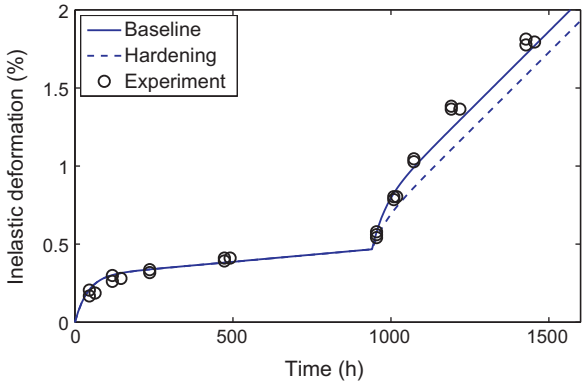

Fig. 4. Simulated (lines) and experimental (circles) cladding response to stress increase. Experimental data from Fig. 3 of Ref. [10].

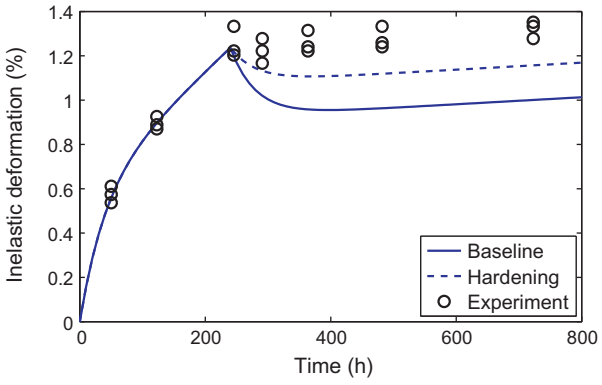

Fig. 5. Simulated (lines) and experimental (circles) cladding response to load drop. Experimental data from Fig. 4 of Ref. [10].

Fig. 4 the match is good, the experiments with load reversals, depicted in Figs. 6 and 7, demonstrate the need for additional assumptions. The primary creep during the subsequent stress steps was clearly smaller than during the initial primary creep stage. Matsuo uses in his work a concept of creep hardening surface [10]. In our model, similar improvement can be achieved by assuming that there are hardening processes which decrease the saturated primary creep by half during primary creep re-initiation. With such an assumption, simulation results according to the *hardening* line in Figs. 4–7 were achieved.

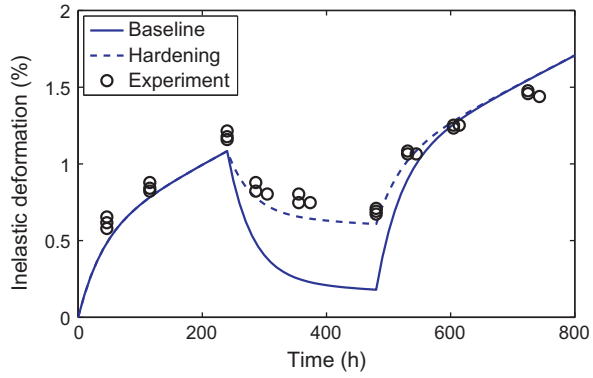

Fig. 6. Simulated (lines) and experimental (circles) cladding response to stress reversal. Experimental data from Fig. 7 of Ref. [10].

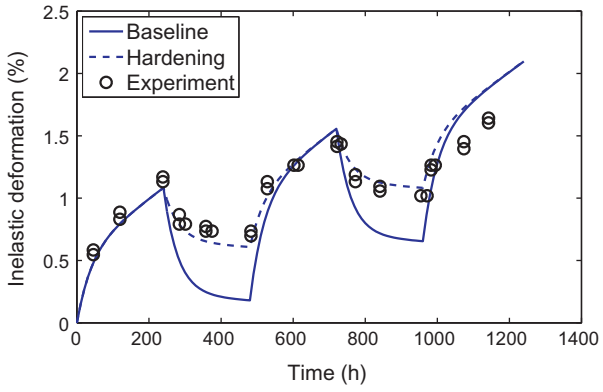

Fig. 7. Simulated (lines) and experimental (circles) cladding response to stress reversal. Experimental data from Fig. 9 of Ref. [10].

Fig. 4 shows the results of a test where the hoop stress was first set at $\sigma_h = 77.9$ MPa and then increased to $\sigma_h = 148.1$ MPa. The match between the experiment and simulation is good, and here the effect of the hardening is not overly clear. It should be noted that this kind of experiment, where the stress is increased, is where the strain hardening rule provides good results. As seen here, the model proposed in this paper provides similar behavior to strain hardening rule in cases where stress is increased in subsequent steps.

Fig. 5 shows the results of a test where the hoop stress was first set $\sigma_h = 156.9$ MPa and then decreased to $\sigma_h = 74.3$ MPa. Matsuo noted that a certain amount of strain recovery was observed just after the load drop [10], which is also shown by the new model. The strain recovery phenomenon is documented also by Murty [5]. The discrepancy between the simulation and the experiment can be mostly attributed to a slightly too low secondary creep rate.

Figs. 6 and 7 show results of two experiments where the load was alternated between tension ($\sigma_h = 148.1$ MPa) and compression ($\sigma_h = -78.0$ MPa). Here the need for assuming some hardening behavior in primary creep is evident. The other alternative would be to assume initial σ_{int} to be of the order of -150 MPa due to manufacturing or test setup effects which would increase the initial primary creep relative to subsequent stress steps. However, such a large value for the initial σ_{int} is considered improbable. The match between the experiment and simulation is good, therefore demonstrating the applicability of the proposed model in load reversal situations. The need for a hardening assumptio,n which was not needed in the IFA-585 analysis, raises a question whether the Zircaloy primary creep behavior during in-pile and out-of-pile experiments are equivalent.

4. Conclusions

In this paper simple and easily implementable rules, Eqs. (10) and (11), for the primary creep behavior of Zircaloy cladding were derived based on in-pile results from Halden IFA-585 creep experiment. A creep model using these rules is capable of replicating observed behavior during stress reversal and load drop situations required in fuel behavior codes. In scenarios where a commonly used strain hardening rule is known to work, such as stress increases, the current model behaves similarly to other strain hardening models. However, instead of hardening to strain, the new model effectively relaxes to current externally imposed stress state.

Most of the stresses imposed to the cladding in IFA-585 were low enough for the creep rate to depend linearly on the stress. Therefore the model is most applicable to low stress situations such as the normal reactor operation. The applicability to thermal creep experiments was also demonstrated. Different model parameters were required for the tests. For the parameter C describing the stress/strain-relation, the ratio of used values is approximately 20. This can be argued to be due to differences in test temperatures, which were 575–595 K for IFA-585 and 662.9–664.0 K for Matsuo's experiments. The characteristic times, τ, for the primary creeps differed also, 40 h for Matsuo experiments and 100 h for IFA-585. The faster kinetics could be attributed to higher temperature. Different materials and experimental conditions do affect the results also. These relationships should be investigated further in order to create a full creep model implementable to a fuel behavior code.

The comparisons between the thermal creep experiments show a difference in the primary creep re-initiation behavior between in-pile and out-of-pile experiments. This is significant as most variable stress experiments are performed out-of-pile whereas the application, the modeling of nuclear fuel in reactor, requires a correct description of the in-pile behavior. Unfortunately, there are few published in-pile creep experiments with transient stress states.

The cladding of the nuclear fuel experiences varying conditions during its reactor life, from compressive stresses during initial reactor cycles to tensile stress imposed by the expanding fuel pellets and increasing rod internal pressure. Accurate modeling of the cladding stress response to transient stresses is important for both operational and safety considerations. The rules derived in this paper provide new insight into how the stress transients can be treated.

Acknowledgements

This work was partially funded by SAFIR2014, the Finnish Research Programme on Nuclear Power Plant Safety 2011–2014, and Academy of Finland funded IDEA project. The model development was carried out in co-operation with Halden Reactor Project.

Appendix A. Supplementary material

Supplementary data associated with this article can be found, in the online version, at http://dx.doi.org/10.1016/j.jnucmat.2013.10.053.

References

[1] W. Wiesenack, T. Tverberg, M. McGrath, E. Kolstad, S. Beguin, Journal of Nuclear Science and Technology 43 (2006) 1037–1044.
[2] G. Lucas, R. Pelloux, Nuclear Technology 53 (1981) 46–57.
[3] D. Lee, F. Zaverl, E. Plaza-Meyer, Journal of Nuclear Materials 88 (1980) 104–110.

[4] L. Jernkvist, in: Transactions of the 15th International Conference on Structural Mechanics in Reactor Technology (SMiRT-15) C04/3, 1999, pp. 477–484.
[5] K. Murty, K. Yoon, in: Transactions of the 5th International Conference on Structural Mechanics in Reactor Technology (SMiRT-5) C3/6, 1979.
[6] K. Murty, JOM 51 (1999) 32–39.
[7] T. Ikonen, V. Tulkki, Nuclear Engineering and Design, submitted for publication.
[8] G. Rossiter, Nuclear Engineering and Technology 43 (2011) 489–498.
[9] M. McGrath, HWR-471, 1996.
[10] Y. Matsuo, ASTM STP 1023, 1989, pp. 678–691.
[11] D. Franklin, G. Lucas, A. Bement, ASTM STP 815, 1983.
[12] Y. Matsuo, Journal of Nuclear Science and Technology 24 (1987) 111–119.
[13] F. Garzarolli, H. Stehle, E. Steinberg, ASTM STP 1295, 1996, pp. 12–32.
[14] Y.S. Kim, Journal of Nuclear Materials 250 (1997) 164–170.
[15] A. Soniak, N. L'Hullier, J.-P. Mardon, V. Rebeyrolle, P. Bouffioux, C. Bernaudat, ASTM STP 1423, 2002, pp. 837–862.
[16] K. Ito, K. Kamimura, Y. Tsukuda, in: Proceedings of the 2004 International Meeting on LWR Fuel Performance, 2004, pp. 440–451.
[17] M. Griffiths, N. Christodoulou, S. Donohue, ASTM STP 1467, 2005, p. 686.
[18] J. Moon, P. Cantonwine, K. Anderson, S. Karthikeyan, M. Mills, Journal of Nuclear Materials 353 (2006) 177–189.
[19] R. Holt, Journal of Nuclear Materials 372 (2008) 182–214.
[20] H. Wang, Z. Hu, W. Lu, M. Thouless, Journal of Nuclear Materials 433 (2013) 188–198.
[21] M. Limback, T. Andersson, ASTM STP 1295, 1996, pp. 448–468.
[22] K. Geelhood, Nuclear Engineering and Technology 43 (2011) 509–522.
[23] K. Geelhood, W. Luscher, C. Beyer, NUREG/CR-7022, vol. 1, 2011.
[24] W. Luscher, K. Geelhood, NUREG/CR-7024, 2011.
[25] J. Foster, M. McGrath, in: Proceedings of the 2007 LWR Fuel Performance Meeting, 2007.
[26] H. Banks, S. Hu, Z. Kenz, Advances in Applied Mathematics and Mechanics 3 (2011) 1–51.
[27] IFPE database NEA IFPE/IFA-585 experimental data, Last modified 13-MAR-2008.
[28] A. Donaldson, HWR-413, 1994.
[29] M. McGrath, in: Proceedings of the 2000 International Topical Meeting on LWR Fuel Performance, 2000.

PUBLICATION IV

Viscoelastic modeling of Zircaloy cladding in-pile transient creep

Journal of Nuclear Materials, **457**, 324–329.

Journal of Nuclear Materials 457 (2015) 324–329

Contents lists available at ScienceDirect

Journal of Nuclear Materials

journal homepage: www.elsevier.com/locate/jnucmat

Viscoelastic modelling of Zircaloy cladding in-pile transient creep

Ville Tulkki *, Timo Ikonen

VTT Technical Research Centre of Finland, P.O. Box 1000, 02044 VTT, Finland

ARTICLE INFO

Article history:
Received 25 September 2014
Accepted 24 November 2014
Available online 3 December 2014

ABSTRACT

In fuel behaviour modelling accurate description of the cladding stress response is important for both operational and safety considerations. The cladding creep determines in part the width of the gas gap, the duration to pellet-cladding contact and the stresses to the cladding due to the pellet expansion. Conventionally the strain hardening rule has been used to describe the creep response to transient loads in engineering applications. However, it has been well documented that the strain hardening rule does not describe well results of tests with load drops or reversals.

In our earlier work we have developed a model for primary creep which can be used to simulate the in- and out-of-pile creep tests. Since then several creep experiments have entered into public domain. In this paper we develop the model formulation based on the theory of viscoelasticity, and show that this model can reproduce the new experimental results. We also show that the creep strain recovery encountered in experimental measurements can be explained by viscoelastic behaviour.

1. Introduction

The cladding tube of nuclear fuel rod protects the urania pellets from the corrosive environment as well as contains the radioactive fission products. Early on during the rod reactor life the cladding creeps inwards due to pressure differential between the reactor system pressure and the rod fill gas. The inward creep of the cladding and swelling of the fuel pellet eventually lead to closing of the gas gap and mechanical interaction between pellets and cladding wall. And with very high burnup there is the possibility of high rod internal pressure exceeding the system pressure, potentially causing the cladding creep outwards faster than the pellets swell and re-opening the gas gap. All these affect the fuel performance and some have potential to cause fuel failures. It is therefore very important to properly understand and describe the various phenomena affecting the fuel rod. While numerous studies have been done on the creep properties of various cladding materials [1–13], the creep response to transient stresses is investigated only in a small subset of the work [1,2,5,8,10,12]. However it should be noted that the transient response governs the cladding behaviour during situations where most damage can happen, i.e. transients.

Conventionally fuel cladding deformation is assumed to have elastic and viscoplastic components. Viscoplastic creep is described by having three regions: the primary (or transient) region, the secondary steady state region and the third leading to failure. The correlations are matched to experiments with a single stress increase, and the change of stress encountered in fuel behaviour analysis is handled by hardening laws. The creep in metals is assumed to follow either a time or a strain hardening law, and the latter is believed to hold for Zirconium alloys in usual operating conditions [2].

Various creep correlations have been formulated over the years that take both thermal and irradiation creep into account. It is well known that the hardening laws used to take the transient conditions into account are simplifications and do not apply universally. Stress reversal and stress reduction are special situations where the hardening law fails and requires additional assumptions to model the observed behaviour [1,2,5]. These situations have been successfully described with complex formulations of cladding material thermodynamic states [14,15] and by assuming additional deformation terms such as reversible anelastic deformation [1,16]. Also anisotropy of the cladding tubes can be described with high precision with advanced methods [7,17].

While these formulations appear to provide correct prediction of the cladding creep behaviour they are not commonly implemented in fuel behaviour codes due to their complexity and computational limitations [18]. Fuel behaviour analysis is commonly performed with integral codes utilizing separate models to describe various phenomena, and the number of required simulations may rise to hundreds of thousands of fuel rod simulations depending on the application [19]. For this purpose, a simple and more practical approach is needed. Previously we have shown that the cladding behaviour during stress reversal and reduction can be roughly modelled using simple internal variable approach [20].

* Corresponding author. Tel.: +358 20 722 6114; fax: +358 20 722 7001.
E-mail address: ville.tulkki@vtt.fi (V. Tulkki).

http://dx.doi.org/10.1016/j.jnucmat.2014.11.100
0022-3115/

In this paper we develop the primary creep model further starting from Standard Linear Solid model which is commonly used in studies of viscoelasticity of a wide range of materials and as such provides a solid theoretical foundation for the model. We compare the primary creep model to experimental data that has recently entered the public domain. The model with primary creep based on viscoelastic behaviour is derived in Section 2. Halden experiments IFA-699 and IFA-696 are used to assess the validity of the model in Section 3 and the results are discussed in Section 4. Conclusions are given in Section 5.

2. Creep model

2.1. Viscoelastic model

In studies of viscoelastic properties of solids, a common method of describing models is via so-called mechanical analogs [21]. These combine springs representing the elastic component of the material to dashpots representing the viscous components. The springs' displacement is $\epsilon_{\text{spring}} = \sigma/\kappa_i$, where κ_i is the elastic modulus of spring i and σ is the external stress affecting the given component, while the dashpots' rate of displacement is of $\dot{\epsilon}_{\text{dashpot}} = \sigma/\eta_i$, where η_i is the viscosity of the dashpot i. Other components are also possible in order to describe more complex interactions.

A mechanical analog of our creep model is shown in Fig. 1. There is a separate node describing the secondary thermal and irradiation creep in series to a Standard Linear Solid (SLS) model. Secondary creep is nonlinear [4,7,6,22] yet it interacts with rest of the system similarly to dashpot as it is decoupled from the elastic and primary creep deformations in creep experiments. Therefore the dashpot symbol D is used as a stand-in for a more complex function describing the secondary creep. SLS consists of two parallel arms, a spring and a serial combination of a spring and a dashpot. The SLS is the simplest mechanical analog capable of qualitatively describing material behaviour during both imposed stress (so-called creep tests) and imposed elongation (stress relaxation test) [21].

Conventionally the stress response of the cladding is separated into elastic response ϵ_{el} and creep, which in turn has both primary (ϵ_p) and secondary (ϵ_s) components:

$$\epsilon = \epsilon_{el} + \epsilon_p + \epsilon_s. \tag{1}$$

SLS part of the model shown in Fig. 1 simulates the elastic and primary creep components of Eq. (1) and replaces the need for strain hardening rule. It should be evident from Fig. 1 that the elastic response and primary creep are intrinsically linked in this formulation and the secondary creep is separate, in contrast to most formulations [4,7,6] which consider primary and secondary creep linked and elastic response separate from the creep.

The solution to SLS is well known [21]. The general relationship is given by

$$\sigma(t) + \frac{\eta_C}{\kappa_B}\frac{d\sigma(t)}{dt} = \kappa_A\left(\epsilon(t) + \eta_C\frac{\kappa_A+\kappa_B}{\kappa_A\kappa_B}\frac{d\epsilon(t)}{dt}\right), \tag{2}$$

where either the strain ϵ or stress σ can be solved when the other is given as well as the initial condition is known.

In the context of fuel behaviour modelling we are interested in solving the strain as a function of piece-wise constant stress that can be implemented into the time-stepping scheme of the fuel performance code. For simplicity, we assume that the stress in the beginning is zero, $\sigma(t_0) \equiv \sigma_0 = 0$, and the strain correspondingly $\epsilon_0 \equiv \epsilon(t_0) = 0$. Further, we assume that the stress changes occur instantaneously at times t_i so that for $t_i \leqslant t < t_{i+1}$ the stress is constant $\sigma(t) = \sigma(t_i) \equiv \sigma_i$. Then the stress can be written as

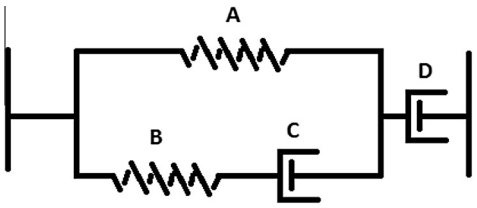

Fig. 1. Mechanical analog for the Standard Linear Solid model (nodes A, B and C) in series with a node D representing secondary creep contribution.

$$\sigma(t) = \sum_{i=1}^{N}\Delta\sigma_i\Theta(t-t_i), \tag{3}$$

where $\Delta\sigma_i = \sigma_i - \sigma_{i-1}$, Θ is the Heaviside step function and the sum is taken over all the N stress changes.

The solution of the SLS model is derived in Appendix A. The resulting strain including the elastic, primary creep and secondary creep contributions is of the form

$$\epsilon(t) = \frac{\sigma(t)}{\kappa} + C\sum_{i=1}^{N}\Delta\sigma_i\left(1-e^{-\frac{t-t_i}{\tau}}\right)\Theta(t-t_i) + \int_{t_0}^{t} f(\sigma(\xi))d\xi, \tag{4}$$

with the constants given by

$$\kappa = \kappa_A + \kappa_B, \tag{5}$$

$$C = \frac{\kappa_B}{\kappa_A(\kappa_A+\kappa_B)}, \tag{6}$$

$$\tau = \eta_C\frac{\kappa_A+\kappa_B}{\kappa_A\kappa_B}. \tag{7}$$

The first term in Eq. (4) corresponds to the elastic strain, the second to primary creep and the last one to secondary creep (both thermal and irradiation induced).

2.2. Implementation of model for primary creep

The primary creep term,

$$\epsilon_p(t) = C\sum_{i=1}^{N}\Delta\sigma_i\left(1-e^{-\frac{t-t_i}{\tau}}\right)\Theta(t-t_i), \tag{8}$$

involves a sum over the whole stress history with exponentially decaying contributions from all the previous stress changes. In such a non-Markovian form the model is difficult to implement into a fuel performance code. However, it is possible to write the model in a form where the future evolution of the system depends only on the present state of the system. This can be done by introducing an additional variable describing the internal state of the system where the memory effects can be embedded.

We describe the internal state of the cladding with a single time-dependent stress-like variable $\sigma_{\text{int}}(t)$. The time evolution $\sigma_{\text{int}}(t)$ describes the relaxation of the internal state of the system towards the steady state determined by the applied stress $\sigma(t)$. The scale of $\sigma_{\text{int}}(t)$ is chosen so that for an initial state with zero primary creep rate and the applied stress equal to σ_0, $\sigma_{\text{int}}(t_0) = \sigma_0$. As the applied stress is changed to σ_1, the variable $\sigma_{\text{int}}(t)$ starts to evolve in time, approaching the new steady state value $\sigma_{\text{int}}(t\to\infty) = \sigma_1$, which is reached when the primary creep has fully saturated. For several stepwise changes as in Eq. (3), the model takes the form (see Appendix A and Ref. [20])

$$\epsilon_p(t+\Delta t) = \epsilon_p(t) + C[\sigma(t) - \sigma_{\text{int}}(t)]\left(1-e^{-\frac{\Delta t}{\tau}}\right), \tag{9}$$

$$\sigma_{\text{int}}(t+\Delta t) = \sigma(t) - [\sigma(t) - \sigma_{\text{int}}(t)]e^{-\frac{\Delta t}{\tau}}. \tag{10}$$

The model yields a primary creep that is reinitiated at each stress change and whose saturated value is proportional to the change in stress. These are in line with observations from experiments conducted at Halden Reactor [12,23]. The evolution in time is a simple exponential function which would correspond to a single relaxation mechanism. While this is probably not the case for Zirconium based alloys used in cladding tubes [1,4], we consider the simplicity of the model and presentation to be important at this point. Previously we have shown the creep model using Eqs. (9) and (10) to be able to describe the creep behaviour during step stress transients [20] in experiments conducted by Matsuo [5] and in IFA-585 experiment performed in Halden research reactor [12,24,25]. More complex variations of SLS exist [21] and these should be utilized to model the exact time evolution of the primary creep.

2.3. Implementation of model for secondary creep

The secondary creep is a complex phenomenon and much research has been dedicated to determining the factors affecting it, see e.g. Refs. [3,4,6,13,12,22]. Fortunately in our model the secondary creep is fully decoupled from the elastic and primary creep contributions in creep experiment conditions. For simulating the secondary steady state contribution to creep we use fuel performance code FRAPCON-3.4's correlation [26–28] which is effectively the model by Limback and Andersson [6] modified to use effective stress σ_{eff} instead of hoop stress:

$$\dot{\epsilon}_{th} = A\frac{E}{T}\left(\sinh\frac{a_i\sigma_{\text{eff}}}{E}\right)^n e^{-\frac{Q}{RT}} \quad \text{and} \tag{11}$$

$$\dot{\epsilon}_{irr} = C_0 \cdot \phi^{C_1} \cdot \sigma_{\text{eff}}^{C_2} \cdot f(T), \tag{12}$$

where E is the elastic modulus, T is temperature in K, R is the universal gas constant, Q the activation energy of the creep, ϕ the fast neutron flux (n/m^2 s^{-1}) and variables A, a_i, n, C_i and the function $f(T)$ have different values depending on the cladding type and the environment as described in Ref. [28]. The use of σ_{eff}

$$\sigma_{\text{eff}} = \sqrt{0.5((\sigma_a-\sigma_h)^2+(\sigma_h-\sigma_r)^2+(\sigma_r-\sigma_a)^2)} \tag{13}$$

is justified by an improved modelling of tensile and compressive creeps [28]. Here $\sigma_{a,h,r}$ denote stresses in axial, hoop and radial directions and isotropic behaviour is assumed for simplicity.

3. Experimental verification

3.1. IFA-699

Recently Halden Work Report HWR-882 [23] was declassified. It describes the experiment IFA-699 featuring on-line measurements of the creep of Zircaloy-4, E110, M5 and M-MDA cladding tube segments containing fuel pellets for realistic temperature gradient. The experiment was still on-going but at the time it had lasted for nearly 3000 full power hours and had subjected the cladding samples to hoop stress levels of 0, −75, −50 and +30 MPa of hoop stress, with negative values indicating compression and positive values tension. This was achieved by alternating the segment internal pressure (to 18.2, 8.5, 11.6 and 22.7 MPa) while the external pressure was at steady 16.2 MPa simulating PWR conditions.

We compare the model with the measurements of Zircaloy-4 segment as the secondary creep model is tuned for it. In order to simulate the experiment, the effective mid-wall stress σ_{eff} was calculated from

$$\sigma_{\text{eff}} = \sqrt{3}\frac{(p_{\text{int}}-p_{\text{ext}})r_i^2 r_o^2}{((r_i+r_o)/2)^2(r_o^2-r_i^2)} \tag{14}$$

where r_i and r_o are the cladding tube inner and outer radii and p_{int} and p_{ext} the pressures internal and external to the tube. The fast flux was reported to be $1.5\cdot10^{13}$ n/cm^2/s and cladding temperature approximately 625 K [23]. Primary creep coefficients $C = 5\times10^{-6}$ m^2/N and $\tau = 40$ h were fitted to match the experimental data. The measured values are shown as dots and the base simulation as the solid line in Fig. 2.

The measured values in Fig. 2 consistently trend toward the positive (or tensile, outward) direction. One possible explanation would be that the general stress is not the correct driving force for creep. It should be noted that the original correlation [6] using hoop stress as a driving force yields a worse match between creep in tension and compression. Third contender for the driving force is the deviatoric hoop stress as suggested by Foster and Baranwal [29]. Other possibility is the growth of oxide layer which did complicate the interpretation of the earlier Halden experiment [12]. We included a oxide growth contribution to the simulations according to Eq. (15) [30].

$$\delta = Ke^{-\frac{E}{RT}}t^n \tag{15}$$

where δ is the oxide layer thickness in μm assuming a constant temperature, $K = 23663.76$ μm h^{-1}, $E/R = 8645.4$ K, $T = 625$ K is the interaction layer temperature, t is time in hours and $n = 1.02474$. As the oxidation replaces metal with less dense oxide, the net effect is the increase of the apparent diameter by a fraction of one third of the oxide layer thickness. The creep with oxide layer contribution is shown with dashed line in Fig. 2. This case would represent a situation where the Zircaloy-4 segment is heated by the fuel inside and thus oxidises faster than the measurement calibration piece which we assume would be at coolant temperature (approximately 50 K lower than the test sample). The used oxide layer equation is a simple formula fitted to publicly available post-irradiation data for PWR fuels with Zircaloy-4 cladding, and as such caution should be used when utilizing it for samples in Halden flask conditions.

While there are uncertainties regarding the secondary creep and the effect of oxidation on the measurements it should be noted that these do not affect the primary creep part of the model which performs well in describing the experimental results.

3.2. IFA-696

A creep experiment with Zircaloy-2 specimens was conducted at Halden reactor and reported by Kozar et al. [22]. They reported

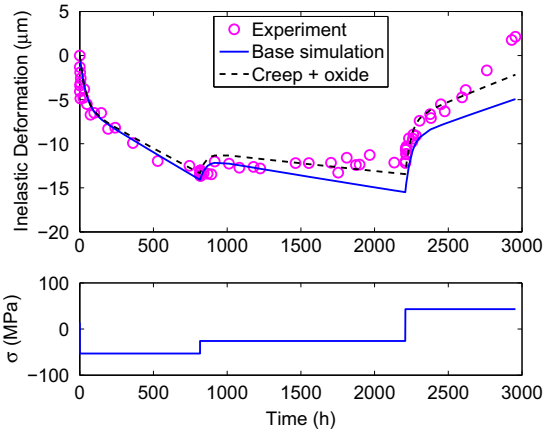

Fig. 2. Creep of Zircaloy-4 segment in IFA-699 experiment, with measurements shown in circles and simulated values with lines.

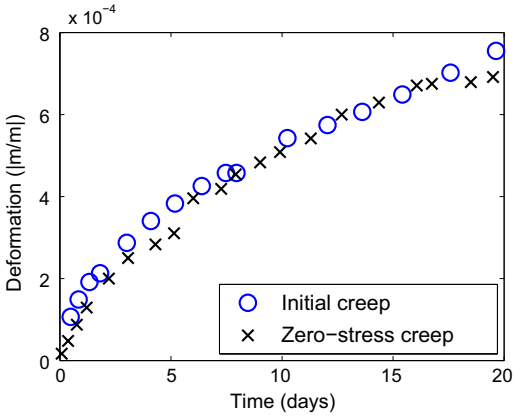

Fig. 3. Magnitude of deformation during the initial creep and the zero-stress period for Zircaloy-2 sample in IFA-696 experiment [22].

witnessing a contraction of a sample during a period of very low stress at reactor operational temperatures and flux. Models following the traditional strain hardening rule do not predict such a behaviour. This contraction is well known, as for instance Limbäck and Andersson describe the need to quickly cool the test samples after depressurization in order to avoid the recovery of creep strain in their experiments [6]. However, according to our model this contraction is to be expected and can be explained by viscoelastic behaviour. In the case of the behaviour corresponding to our proposed model the rate of the elongation would be similar in both cases, just in opposite directions.

Data points were taken from Figs. 4 and 5 of Ref. [22] representing the measured deformation during the initial creep and during the zero-stress period. The absolute values of deformation for both cases are shown in Fig. 3 clearly demonstrating that both the rate and the scale of the creep are the same, therefore supporting the assumption that the viscoelastic behaviour is responsible for the sample contraction.

4. Discussion

The major difference of the model presented in this paper to the conventional approach is that we separate the deformation into viscoelastic and viscoplastic components instead of using the usual approach to separate elastic and viscoplastic (creep) components. The viscoelastic component is modelled with Standard Linear Solid model which is known to be able to model the behaviour of various substances for small deformations. As this limitation is also inherent in the 1D approach for cladding modelling in engineering level codes, it should not decrease the usability domain of the fuel performance codes.

Similar approaches to cladding creep have been proposed by Murty [1] and Geelhood [31]. Murty adds an anelastic component to the usual elastic and creep components [1], thus indicating that a part of the transient deformation is due to delayed elasticity (or viscoelasticity). In contrast to this our model describes the whole of transient deformation by viscoelasticity. The reason to this difference might be the difference in in- and ex-pile behaviour. Murty investigates cladding creep in out-of-pile experiments and as we saw in our previous work [20] it would appear that the in-pile creep differs quantitatively from out-of-pile creep. Geelhood presents a model with a stress threshold for re-initiation of the primary creep [31] to explain the observations of IFA-699. While our approach provides similar results with stress steps that are long enough for the primary creep to fully develop, the viscoelastic model is more consistent in situations with rapid stress changes.

The SLS-based model is able to replicate the creep behaviour of IFA-699 creep experiment's Zircaloy-4 segment. In earlier work [20] the similar approach was shown to be able to describe the behaviour of earlier IFA-585 experiment [12,24,25] as well as out-of-pile Zircaloy-4 creep experiment with load drops and reversals by Matsuo [5]. The used time constant $\tau = 40$ h was the same as the one describing out-of-pile Zircaloy-4 primary creep whereas the $C = 5 \times 10^{-6}$ m^2/N is lower than for the out-of-pile tests. This might be due to the higher temperature (by approximately 30 K) or significantly higher stress levels (potentially leaving linear stress response regime) used in Matsuo's experiments. While the experimental conditions do not exactly match each other, there are similarities in the time evolution and stress dependency of primary creep. This would indicate that the irradiation would not have a strong effect on primary creep. There are challenges in modelling the steady state creep behaviour with the chosen model for secondary creep. There may be several explanations: the usual variation in creep behaviour between different Zircaloy tubes, the general stress not being the proper driving force for the creep or the effect of differing oxide formation rates.

The observed contraction during the stress-free period at operating temperatures of IFA-696 [22] is similar in magnitude to the initial primary creep. This is as expected should the viscoelastic behaviour accurately describe the Zircaloy stress response, whereas traditional strain hardening law requires additional assumptions to be made. The match between creep at the beginning of the experiment and during the stress-free period is surprisingly good as one would expect secondary creep to show during the tensile creep. This feature may stem from several sources. For instance, temperature fluctuated between 530 and 550 K during the zero-stress creep period, thus potentially influencing the measurements. Also, as the data is provided only as a relative deformation the elastic deformation may affect the reference level. This would slightly increase the apparent magnitude of inwards creep.

Kozar et al. investigate the reason to observed contraction based on calculated reaction rates [22]. According to their analysis, irradiation-induced transient creep would be too rapid to account for the observed contraction, and therefore they deduce that the relaxation of strain-hardening of the microstructure is the likely reason to the observations. We would claim instead that the observed contraction is due to the viscoelastic properties of the material. It could be argued that these two interpretations are just different expressions for the same phenomenon, however the difference becomes evident when behaviour during change in stress direction is considered. Under such conditions our model based on SLS behaves in a way that is supported by the observations of earlier Halden experiments [8,12,23].

5. Conclusions

The cladding tube creep response to transient stresses is traditionally modelled according to strain hardening law in engineering level integral fuel behaviour codes. This approach has severe limitations in modelling of situations with load reductions and reversals. Also, additional postulated phenomena such as creep recovery have been introduced to account for the experimental observations. In this paper we have derived a creep model based on the theory of viscoelasticity. We have shown that it can be used to model the observed transient creep phenomena on an empirical macroscopic level as well as provide interpretation on the experimentally observed creep strain recovery phenomenon.

While conventionally nuclear fuel cladding deformation has been considered to consist of elastic and viscoplastic components, our analysis demonstrates that viscoelastic behaviour should also be considered. This influences cladding response to transient

conditions, and therefore has implications to analysis of phenomena such as pellet cladding interaction and lift-off.

Acknowledgements

This work was partially funded by SAFIR2014, the Finnish Research Programme on Nuclear Power Plant Safety 2011-2014, and Academy of Finland funded IDEA project.

Appendix A. Derivation of the SLS solution and the primary creep algorithm

The elastic and primary creep terms in Eq. (4) can be solved from the general form of the SLS solution (Eq. (2)) by substituting for $\sigma(t)$ the piece-wise constant stress function of Eq. (3), and $d\sigma(t)/dt = \sum_{i=1}^{N}\Delta\sigma_i\delta(t-t_i)$ for the time derivative. Here $\delta(t-t_i)$ is the Dirac delta distribution. This results in the equation

$$\kappa_A\epsilon + \kappa_A\tau\frac{d\epsilon}{dt} = \sum_{i=1}^{N}\Delta\sigma_i\Theta(t-t_i) + \frac{\eta_C}{\kappa_B}\sum_{i=1}^{N}\Delta\sigma_i\delta(t-t_i).$$

The strain ϵ can be solved by taking the Laplace transform $\hat{\epsilon}(s) = \int_{t_0}^{t}\epsilon(t')e^{st'}dt'$, and assuming the initial condition $\epsilon(t_0)=0$. Then, one has

$$\kappa_A(1+\tau s)\hat{\epsilon}(s) = \sum_{i=1}^{N}\left[\Delta\sigma_i e^{-st_i}\left(\frac{1}{s}+\frac{\eta_C}{\kappa_B}\right)\right],$$

which, after re-arranging gives

$$\hat{\epsilon}(s) = \frac{1}{\kappa_A}\sum_{i=1}^{N}\left\{\Delta\sigma_i e^{-st_i}\left[\frac{1}{s}+\left(\frac{\eta_C}{\kappa_B\tau}-1\right)\frac{1}{s+1/\tau}\right]\right\}.$$

Inverse Laplace transform of $\hat{\epsilon}(s)$ gives

$$\begin{aligned}\epsilon(t) &= \sum_{i=1}^{N}\left[\Delta\sigma_i\Theta(t-t_i)\left(\frac{1}{\kappa_A}-\frac{\kappa_B}{\kappa_A(\kappa_A+\kappa_B)}e^{-\frac{t-t_i}{\tau}}\right)\right]\\ &= \frac{1}{\kappa_A+\kappa_B}\sum_i\Delta\sigma_i\Theta(t-t_i) + \frac{\kappa_B}{\kappa_A(\kappa_A+\kappa_B)}\sum_{i=1}^{N}\Delta\sigma_i\left[1-e^{-\frac{t-t_i}{\tau}}\right]\Theta(t-t_i)\\ &= \frac{\sigma(t)}{\kappa} + C\sum_{i=1}^{N}\Delta\sigma_i\left(1-e^{-\frac{t-t_i}{\tau}}\right)\Theta(t-t_i),\end{aligned}$$

with C given by Eq. (6). The primary creep of Eq. (8) is then identified as the second term,

$$\epsilon_p(t) = C\sum_{i=1}^{N}\Delta\sigma_i\left(1-e^{-\frac{t-t_i}{\tau}}\right)\Theta(t-t_i).$$

Force balance implies that the stress imposed on the SLS (A, B, C) and the secondary creep (D) parts of the model shown in Fig. 1 are equal. Therefore the strain due to secondary creep can be simply added to the strain of the SLS part, as is done in Eq. (4).

To derive the algorithm of Eqs. (9) and (10), we first use Eq. (8) to write down $\epsilon_p(t+\Delta t)$, then divide the sum over stress changes into two parts: those changes occurring before time t, and those occurring between t and $t+\Delta t$:

$$\begin{aligned}\epsilon_p(t+\Delta t) &= C\sum_{i=1}^{N}\Delta\sigma_i\left(1-e^{-\frac{t+\Delta t-t_i}{\tau}}\right)\Theta(t+\Delta t-t_i)\\ &= C\sum_{i=1}^{N}\Delta\sigma_i\left(1-e^{-\frac{t+\Delta t-t_i}{\tau}}\right)\Theta(t-t_i)\\ &\quad + C\sum_{i=1}^{N}\Delta\sigma_i\left(1-e^{-\frac{t+\Delta t-t_i}{\tau}}\right)\Theta(t+\Delta t-t_i)\Theta(t_i-t)\end{aligned}$$

If the length of the time step Δt is chosen such that the stress is constant between t and $t+\Delta t$, the last term is equal to zero. In this case,

$$\begin{aligned}\epsilon_p(t+\Delta t) &= C\sum_{i=1}^{N}\Delta\sigma_i\left(1-e^{-\frac{t+\Delta t-t_i}{\tau}}\right)\Theta(t-t_i)\\ &= C\sum_{i=1}^{N}\Delta\sigma_i\left(1-e^{-\frac{t-t_i}{\tau}}\right)\Theta(t-t_i)e^{-\frac{\Delta t}{\tau}} +\\ &\quad - C\sum_{i=1}^{N}\Delta\sigma_i\left(1-e^{-\frac{\Delta t}{\tau}}\right)\Theta(t-t_i)e^{-\frac{\Delta t}{\tau}}\\ &= \epsilon_p(t)e^{-\frac{\Delta t}{\tau}} + C\sigma(t)\left(1-e^{-\frac{\Delta t}{\tau}}\right) + \left[\epsilon_p(t)-\epsilon_p(t)\right]\\ &= \epsilon_p(t) + \left[C\sigma(t)-\epsilon_p(t)\right]\left(1-e^{-\frac{\Delta t}{\tau}}\right)\end{aligned}$$

To derive the form of the algorithm used in this work, we introduce the internal stress variable $\sigma_{\mathrm{int}}(t)$ as $C\sigma_{\mathrm{int}}(t) = \epsilon_p(t)$. Hence, from Eq. (8),

$$\sigma_{\mathrm{int}}(t) = \sum_{i=1}^{N}\Delta\sigma_i\left(1-e^{-\frac{t-t_i}{\tau}}\right)\Theta(t-t_i).$$

Repeating the steps shown for ϵ_p above, one gets

$$\sigma_{\mathrm{int}}(t) = \sigma_{\mathrm{int}}(t)e^{-\frac{\Delta t}{\tau}} + \sigma(t)\left(1-e^{-\frac{\Delta t}{\tau}}\right).$$

By re-arranging terms, the primary creep algorithm is then obtained as

$$\begin{aligned}\epsilon_p(t+\Delta t) &= \epsilon_p(t) + C[\sigma(t)-\sigma_{\mathrm{int}}(t)]\left(1-e^{-\frac{\Delta t}{\tau}}\right),\\ \sigma_{\mathrm{int}}(t+\Delta t) &= \sigma(t) - [\sigma(t)-\sigma_{\mathrm{int}}(t)]e^{-\frac{\Delta t}{\tau}}.\end{aligned}$$

We note that one may use the above derivation to write down a mathematically equivalent algorithm without introducing the internal stress variable σ_{int}. An equivalent algorithm to Eqs. (9) and (10) would be, for instance,

$$\epsilon_p(t+\Delta t) = \epsilon_p(t)e^{-\frac{\Delta t}{\tau}} + C\sigma(t)\left(1-e^{-\frac{\Delta t}{\tau}}\right).$$

Finally, we recall that both forms of the algorithm rely on the assumption of constant stress over the time step Δt. To take into account the stress change occurring at t_i, one would need to take small time steps δt that bound the stress change as $t \leqslant t_i \leqslant t+\delta t$, and derive the corresponding equations for updating ϵ_p. However, it can be shown that the correction due to this additional step goes to zero in the limit of small δt. That is, $\epsilon_p(t+\delta t) = \epsilon_p(t)$ as $\delta t \to 0$ even when the stress changes between t and $t+\delta t$. In practice one can ignore this intermediate step and change the value of $\sigma(t)$ at the beginning of each time step Δt.

References

[1] K. Murty, K. Yoon, Transactions of the 5th International Conference on Structural Mechanics in Reactor Technology (SMiRT-5) C3/6, 1979.
[2] G. Lucas, R. Pelloux, Nucl. Technol. 53 (1981) 46–57.
[3] D. Franklin, G. Lucas, A. Bement, ASTM STP 815 (1983).
[4] Y. Matsuo, J. Nucl. Sci. Technol. 24 (1987) 111–119.
[5] Y. Matsuo, ASTM STP 1023 (1989) 678–691.
[6] M. Limback, T. Andersson, ASTM STP 1295 (1996) 448–468.
[7] P. Delobelle, P. Robinet, P. Geyer, P. Bouffioux, J. Nucl. Mater. 238 (1996) 135–162.
[8] M. McGrath, Proceedings of the 2000 International Topical Meeting on LWR Fuel Performance, 2000.
[9] A. Soniak, N. L'Hullier, J.-P. Mardon, V. Rebeyrolle, P. Bouffioux, C. Bernaudat, ASTM STP 1423 (2002) 837–862.
[10] K. Ito, K. Kamimura, Y. Tsukuda, Proceedings of the 2004 International Meeting on LWR Fuel Performance, 2004, pp. 440–451.
[11] J. Moon, P. Cantonwine, K. Anderson, S. Karthikeyan, M. Mills, J. Nucl. Mater. 353 (2006) 177–189.
[12] J. Foster, M. McGrath, Proceedings of the 2007 LWR Fuel Performance Meeting, 2007.

[13] R. Holt, J. Nucl. Mater. 372 (2008) 182–214.
[14] D. Lee, F. Zaverl, E. Plaza-Meyer, J. Nucl. Mater. 88 (1980) 104–110.
[15] L. Jernkvist, Transactions of the 15th International Conference on Structural Mechanics in Reactor Technology (SMiRT-15) C04/3, 1999, pp. 477–484.
[16] K. Murty, JOM 51 (1999) 32–39.
[17] F. Onimus, J.-L. Bechade, J. Nucl. Mater. 384 (2009) 163–174.
[18] M. Rautenberg, D. Poquillon, P. Pilvin, C. Grosjean, J. Cloue, X. Feaugas, Nucl. Eng. Des. 269 (2014) 33–37.
[19] T. Ikonen, V. Tulkki, Nucl. Eng. Des. 275 (2014) 229–241.
[20] V. Tulkki, T. Ikonen, J. Nucl. Mater. 445 (2014) 98–103.
[21] H. Banks, S. Hu, Z. Kenz, Adv. Appl. Math. Mech. 3 (2011) 1–51.
[22] R. Kozar, A. Jaworski, T. Webb, R. Smith, J. Nucl. Mater. 444 (2014) 14–22.
[23] S. Hanawa, HWR-882, 2008.
[24] M. McGrath, HWR-471, 1996.
[25] IFPE Database NEA IFPE/IFA-585 Experimental Data (modified 13.03.08).
[26] K. Geelhood, Nucl. Eng. Technol. 43 (2011) 509–522.
[27] K. Geelhood, W. Luscher, C. Beyer, NUREG/CR-7022, vol. 1, 2011.
[28] W. Luscher, K. Geelhood, NUREG/CR-7024, 2011.
[29] J. Foster, R. Baranwal, 16th ASTM Zirconium Symposium, 2010.
[30] J. Katto, Corrosion and its Modeling in Nuclear Reactor Fuel Cladding, M.Sc Thesis, 2013.
[31] K. Geelhood, Proceedings of the 2013 International Topical Meeting on LWR Fuel Performance, 2013.

PUBLICATION V

Modelling anelastic contribution to nuclear fuel cladding creep and stress relaxation

Journal of Nuclear Materials, **465**, 34–41.

Journal of Nuclear Materials 465 (2015) 34–41

Contents lists available at ScienceDirect

Journal of Nuclear Materials

journal homepage: www.elsevier.com/locate/jnucmat

Modelling anelastic contribution to nuclear fuel cladding creep and stress relaxation

Ville Tulkki*, Timo Ikonen

VTT Technical Research Centre of Finland Ltd, P.O.Box 1000, 02044, VTT, Finland

ARTICLE INFO

Article history:
Received 24 January 2015
Received in revised form
10 April 2015
Accepted 25 April 2015
Available online 3 June 2015

Keywords:
Zircaloy-4
Cladding
Stress relaxation
Creep
Anelastic
Viscoelastic
Modelling

ABSTRACT

In fuel behaviour modelling accurate description of the cladding mechanical response is important for both operational and safety considerations. While accuracy is desired, a certain level of simplicity is needed as both computational resources and detailed information on properties of particular cladding may be limited. Most models currently used in the integral codes divide the mechanical response into elastic and viscoplastic contributions. These have difficulties in describing both creep and stress relaxation, and often separate models for the two phenomena are used.

In this paper we implement anelastic contribution to the cladding mechanical model, thus enabling consistent modelling of both creep and stress relaxation. We show that the model based on assumption of viscoelastic behaviour can be used to explain several experimental observations in transient situations and compare the model to published set of creep and stress relaxation experiments performed on similar samples. Based on the analysis presented we argue that the inclusion of anelastic contribution to the cladding mechanical models provides a way to improve the simulation of cladding behaviour during operational transients.

1. Introduction

The cladding of a fuel rod both contains the radioactive fission products and protects the fuel pellets from the cooling water. As such, the integrity of the cladding tube is of utmost importance. During its reactor life, the cladding tube is first under a pressure differential at elevated temperatures and under irradiation, and creeps inwards. The rate of this inward creep determines in part the time of hard contact between the fuel pellets and the cladding wall as well as influences the heat conduction across the gas gap. After a hard contact between the pellet and the cladding wall the pellets push the cladding outward as they expand. At high burnup the rod internal overpressure may even push the cladding to creep faster than the fuel pellet swells. Ergo, at different times the cladding wall is either freestanding under a pressure differential, a case where creep deformation is of interest, or experiences forced displacement with unknown stress that needs to be solved.

Fuel behaviour analysis is commonly performed with integral codes utilizing separate models to describe various phenomena. The number of individual models is large and the number of required fuel rod simulations may rise to hundreds of thousands depending on the application. As such, a simple and practical approach to modelling cladding creep and stress relaxation is needed. Conventionally creep models are derived from experiments conducted with internally pressurized tubes. The models have been used utilizing strain hardening law to take into account the cladding behaviour during alternating stresses. However, the conventional strain hardening law cannot be used to describe creep response to load drops or reversals [1–4], and this is also an issue modelling stress relaxation where the stress is constantly decreasing. Yet in order to model the fuel rod cladding mechanical behaviour during its whole reactor life, the model needs to be able to describe also the stress relaxation behaviour. While strain hardening law has its deficiencies it has been widely adopted in fuel behaviour codes in part due to its simplicity. In order for the alternative approach to replace the established strain hardening law it also needs to retain simplicity and implementability of the old approach.

In our previous work we have introduced an empirical model based on the viscoelastic theory that is capable of describing the observed creep response to transient stresses [5,6]. Viscoelastic models should be able to describe both the creep and the stress

* Corresponding author.
E-mail address: ville.tulkki@vtt.fi (V. Tulkki).

http://dx.doi.org/10.1016/j.jnucmat.2015.04.056
0022-3115/

relaxation behaviour of the materials, at least for small deformations [7]. Therefore assessing the model capability for zirconium alloy stress relaxation is of interest. In this paper we investigate the time evolution of cladding transient response, construct a viscoelastic model and both qualitatively and quantitatively investigate the model behaviour.

The structure of the paper is as follows. In Section 2, we discuss the cladding mechanical behaviour and its relation to viscoelasticity. The simulation model is constructed the Section 3 and its behaviour is investigated in Section 4. The results of the paper are discussed in Section 5 and summarized in Section 6.

2. Background

2.1. Mechanical response

The material response to stresses is usually a combination of elastic, viscous and plastic deformations. For metals the usually considered responses are elastic and viscoplastic (creep) responses. Historically, the cladding creep has been considered to follow the strain hardening law. This was shown by Lucas and Pelloux [1] to provisionally apply to Zircaloy-2 cladding. While their work also showed that the strain hardening rule does not hold for load drops and reversals (further corroborated by Matsuo [2]) many models have adopted it for taking stress transients into account. The online measurements of in-pile creep experiments at Halden reactor [3,4,8] show primary creep reinitializing at every stress change independent of accumulated strain and being proportional to the preceeding stress change, which also is at odds with the strain hardening rule.

Stress relaxation at the imposed specimen elongation is another difficult behaviour for strain hardening law to handle. In a stress relaxation experiment the highest stresses are encountered when the deformation is applied, and then the stresses reduce as the elastic deformation turns into plastic deformation. The strain hardening law assumes that at given stress the creep behaves as in the experiments with a single increase to the given stress. The law assumes that the change in stress can be dealt by moving to the creep curve corresponding to the new stress while keeping the strain constant. In the constantly diminishing stress case this means that all the changes advance the apparent time towards the steady state creep region. Effectively in a stress relaxation experiment nearly all of the deformation would be accounted for by the steady state creep, as the initial high stress provides enough strain for lower stress primary creep to saturate.

Historically the results obtained from stress relaxation experiments have been successfully used to obtain information on cladding creep properties of Zircaloy-2 and Zr-2.5 Nb samples in the region where creep stress dependency is linear, which was defined by the authors of the experimental papers as the region of less than 150 MPa of stress [9,10]. These stresses are encountered after the initial fast relaxation, and it is implicitly assumed that all the transient behaviour similar to primary creep has already happened during the loading of the sample and the initial fast relaxation. More recently there have been studies [11,12] showing that by increasing the stress exponent in creep correlations originally derived from creep experiments of Matsuo [13], the loading and initial relaxation of ZIRLO segments can be also described. However in these studies it is assumed that all the cladding behaviour can be described with equations originally describing only the steady state behaviour, which is curious considering the transient nature of the stress relaxation experiments. There are also other interpretations to the Zircaloy-4 stress relaxation results, such as dividing the stresses into transient and remnant [14], but these do not have direct correspondence to creep experiments.

Formulations of increasing complexity for describing the exact state of cladding do exist, e.g. Refs. [15,16]. Of interest here is the work of Delobelle et al. [15] where a complex model with kinematic variables is created. They concentrate on describing the anisotropy of the material and intentionally leave the description of anelastic properties from the model. However they note that its inclusion would be warranted to describe the cladding response to changing temperature. The model created is still considered too calculationally intensive for use in fuel performance codes [17] so there is still demand for the simplifying approach.

2.2. Viscoelastic modelling

Several authors have either described observed anelastic contributions [10,18] to cladding mechanical behaviour or used anelastic components as a part of their creep model [19]. In the following we use the terminology as defined by Nowick (p. 3 of [20]) where anelasticity is defined as time-dependent recoverable and viscoelasticity as time-dependent nonrecoverable mechanical behaviour. While the model we construct will contain an anelastic part, the inclusion of permanent deformation or steady state creep will make the model as a whole viscoelastic in nature.

Anelastic deformation is originated from several sources. According to Blanter et al. [21] these are point defects such an interstitial atoms which move or rotate in response to stresses to new positions, dislocations that move to accommodate the external stresses and interfaces of the larger scale structures such as grain boundaries, and the relaxation may originate from grain boundary sliding or movement in normal direction (grain growth). Thermoelastic relaxation also produce anelastic deformation as spatially heterogeneous thermoelastic stresses produce temperature gradients that relax by heat flow. Some of these mechanisms are accounted for in the mechanistic formulations of the creep, such as the build-up of internal stresses by pinning of dislocations. Yet in practice this has led to ignoring the anelastic component in engineering models. Therefore the separation of creep and anelastic deformation is warranted in a phenomenological formulation.

In metals anelastic strain is often considered small in relation to the other strain contributions. Also, in the usual applications, anelastic response operates in parallel with primary creep [22], and thus its effect is in part included in the primary creep formulations. However as anelastic deformation is both recoverable and time-dependent it can influence fuel cladding under changing conditions. While there are exceptions [19], not taking anelastic response into account can be considered as a norm in fuel behaviour code creep models.

In studies of viscoelastic properties of solids, a common method of describing models is via so-called mechanical analogs. These combine springs representing the elastic component of the material to dashpots representing the viscous components. The springs' displacement is $\varepsilon_{\text{spring}}=\sigma/\kappa_i$, where κ_i is the elastic modulus of spring i and σ is the external stress affecting the given component, while the dashpots' rate of displacement is of $\dot{\varepsilon}_{\text{dashpot}} = \sigma/\eta_i$, where η_i is the viscosity of the dashpot i.

A Kelvin unit is an analog with a spring and a dashpot in parallel. A general Kelvin model is a serial arrangement of n Kelvin units and a spring, as depicted in Fig. 1. The individual Kelvin units model various relaxation processes that take place at different time scales. The strain response to N step stress increases $\Delta\sigma_j$ at times t_j is [6].

$$\varepsilon(t) = \frac{\sigma(t)}{\kappa_0} + \sum_{j=1}^{N} \Delta\sigma_j \sum_{\kappa_i}^{1} \left(1 - e^{-\frac{t-t_j}{\tau_i}}\right) \Theta(t - t_j), \tag{1}$$

where κ_0 is the elastic modulus of the lone spring, κ_i is the elastic modulus of the spring of the ith spring-dashpot system, $\tau_i=\eta_i/\kappa_i$ is

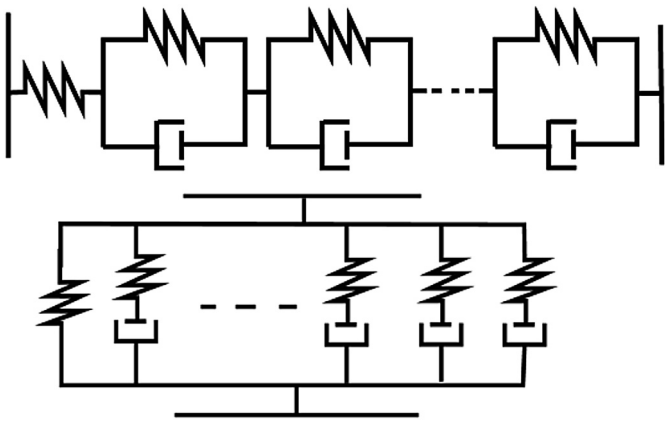

Fig. 1. Mechanical analog for the general Kelvin model (top) and the general Maxwell model (bottom).

the characteristic relaxation time of ith spring-dashpot system and Θ is the Heaviside step function. Higher n provides more accurate representation of a system with multiple relaxation modes at the cost of increasing model complexity. It should be noted that the individual Kelvin units are not meant to represent individual physical processes but instead a macroscopic aggregate of various microscopic processes acting on similar time scales.

The General Kelvin model is often used to analyse cases where the stress is a known input as the stress is transmitted along the whole system as per force balance and the solution of individual Kelvin units are separable. In cases where the imposed elongation is known, the general Maxwell model, consisting of parallel arrangement of a spring and n Maxwell units (a spring and a dashpot in series) is used instead. For both general models setting $n = 1$ creates a Standard Linear Solid (SLS) model (see e.g. pp. 87–88 of [23]).

3. Model for cladding mechanical response to transients

Usually the choice between Kelvin and Maxwell formulations is done based on the topic investigated. Our aim is to construct a model capable of simulating both creep and stress relaxation. We will also need to model the steady state creep, and this has been accomplished earlier [5,6] with a dashpot-like element placed in series to the rest of the solution. The steady state creep dashpot is decoupled from the rest of the solution in the imposed stress case but affects it in the imposed strain case. Therefore we can still obtain the "pure" solution to the general Kelvin model in the creep simulations while no such advantage can be had with the general Maxwell model. Therefore the former is chosen as a basis for our model.

The special case of the general Kelvin model with $n = 1$ units yields exponential time evolution, i.e. $e^{-t/\tau}$ for the viscoelastic deformation or primary creep. For zirconium alloy claddings, the time evolution of primary creep has been argued to be of the form $e^{-\sqrt{t}}$ [13,24] or a more complex one [19]. The $e^{-\sqrt{t}}$ form in particular is an instance of a stretched exponential or Kohlrausch function [25,26], which describes a system with several relaxation mechanisms operating at different rates. The stretched exponential can be approximated by a Dirichlet-Prony series (a weighted sum of exponential functions) [27]:

$$e^{-(t/\tau)^{\beta}} \approx \sum_{i=1}^{n} g_i e^{-t/\tau_i} \tag{2}$$

where each instance of e^{-t/τ_i} describes a relaxation mechanism with a time constant of τ_i and weight of g_i where $\sum g_i = 1$. This is the mathematical background justifying use of general Kelvin models with $n>1$ to describe the systems with observed time evolution of the type of Eq. (2).

We build a model with a spring for elastic response, n number of Kelvin units and a dashpot for plastic deformation, all in series. While conventionally the plastic deformation includes the primary creep, in this model the primary creep is as a whole given by the Kelvin units. This is in line with observed in-reactor creep behaviour [4–6,8]. In general the higher the model's n the better the description. However this both increases the complexity of the model and sets requirements for the amount and quality of the experimental data. In this work we restrict the model to n=1,2. For $n = 1$ this corresponds to our earlier modified SLS model [6]. The system for n=2 is displayed in Fig. 2.

The number of components in a system as depicted in Fig. 2 as well as nonlinearity of the most plastic deformation correlations makes finding analytical solution to the system challenging. A common engineering solution [7] is to use the internal variable approach, where the elongation of each individual component is calculated.

For stress relaxation, we use an explicit numerical solution, calculating the stress arising from the elastic deformation of the lone spring based on the difference between the imposed elongation and the elongation of Kelvin units and the lone dashpot as per Eq. (3). This stress determines the system stress as a whole. Then the elongations of the Kelvin units and the lone dashpot are calculated assuming the stress stays constant for the duration of the time step. The elongations of the Kelvin units are calculated based on Eq. (4) and the plastic strain from Eq. (5):

$$\sigma(t) = \left(\varepsilon_{tot}(t) - \varepsilon_s(t) - \sum_{i=1}^{n} \varepsilon_i(t)\right)\kappa_0, \tag{3}$$

$$\varepsilon_i(t+\Delta t) = \varepsilon_i(t) + (\sigma(t) - \varepsilon_i(t)\kappa_i)\cdot\left(1 - e^{-\frac{\Delta t}{\tau_i}}\right)\kappa_i^{-1}, \tag{4}$$

$$\varepsilon_s(t+\Delta t) = \varepsilon_s(t) + f(\sigma(t))\cdot\Delta t, \tag{5}$$

where ε_{tot} is the total (imposed) strain, κ_0 the elastic spring constant, ε_i, κ_i and τ_i are the strain, spring constant and characteristic time of the ith Kelvin unit, ε_s is the plastic strain, Δt the time step used and σ the stress. $f(\sigma)$ denotes the function for steady state creep rate, which may be a simple function of stress as will be used in this work or a more complex function such as the ones used by Matsuo [13] or Limback and Andersson [24]. This solution scheme requires using very short time steps.

For solving the system during imposed stress (creep experiment), Eqs. (4) and (5) can be directly used as the stress σ is known and each Kelvin unit as well as the lone spring and the lone dashpot experiences the same stress. In order to find out the strain of the

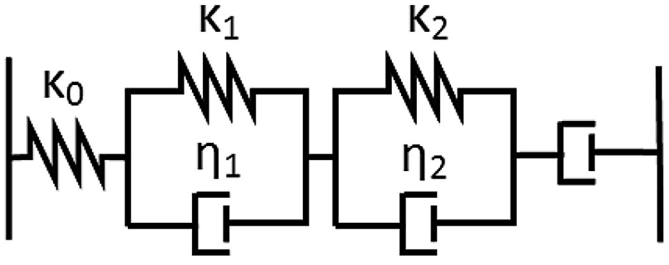

Fig. 2. Mechanical analog for the model describing cladding mechanical response containing a series of spring, 2 K units and a dashpot representing plastic deformation.

whole system ε_{tot} the individual strain components are combined:

$$\varepsilon_{tot}(t) = \frac{\sigma(t)}{\kappa_0} + \varepsilon_s(t) + \sum_{i=1}^{n} \varepsilon_i(t). \quad (6)$$

For the simulations initial values for the internal strains ε_i are needed. In this work we assume $\varepsilon_i(0)=0$ for the *laboratory conditions*. Validity of this assumption could be tested with annealing test of as-manufactured sample with zero externally applied stress. The experimental study with pressurized tubes published by Garzarolli et al. [28] would indicate that for the *reactor conditions* $\varepsilon_i(0) \neq 0$.

4. Model behaviour

4.1. Qualitative behaviour

We investigate the qualitative behaviour of two models, one with elastic (instantaneous recoverable deformation) and plastic (slow nonrecoverable deformation) components and the other with elastic, anelastic and plastic components. The former model corresponds in behaviour to traditional strain hardening models in situations where enough strain has been accumulated for the primary creep to be fully developed. The anelastic component is modelled with a single Kelvin unit yielding slow recoverable deformation, whereas the elastic and plastic components are the same in both models.

One technique for investigating the metal transient response is called stress dip experiment (e.g. p. 67 of Ref. [22]). In the experiment a load is first applied to a sample until a steady strain rate is achieved. Then, the load is reduced for a while and finally increased to its original value. According to Ref. [22], the sample deformation appears to stop for a while at the load reduction before it starts to creep at the rate corresponding to the reduced stress. After the subsequent increasing of the stress the strain rate increases for a while before returning to the strain rate corresponding to the applied stress. Models based on purely plastic deformation do not explain these observations, but as illustrated in Fig. 3a, the observed behaviour is well in line with the one provided by the viscoelastic model.

Several authors of experimental papers [24,29] describe issues encountered when during a creep experiment the stress is reduced to zero while the sample is still at the experimental temperatures. Limback and Andersson [24] describe the need to quickly cool down the experimental Zircaloy-4 sample before the creep recovery sets in and Kozar et al. [29] measure the change in strain in Zircaloy-2 samples during zero stress period. Fig. 3b shows the difference between traditional and viscoplastic interpretation following a prolonged zero stress period. It should be noted that it is common to clean up such periods of zero stress from experimental results, as according to strain hardening law they should not have any effect on the sample strain. However, this results in fast dips in measured strain, which is subsequently recovered, as seen for instance in Fig. 3 of Kozar et al. [29].

Kapoor et al. [14] have performed stress relaxation experiments where they attempt to expedite the acquisition of what they call remnant stress (stress remaining after a long time from the beginning of the stress relaxation experiment) by stepwise reduction of imposed elongation. They report observing at some occasions that after the elongation reduction the stress of the sample increases, contrary to what the plastic models would indicate. As demonstrated in Fig. 3c this can be explained by the viscoelastic properties of the material. The plot also shows that the addition of viscoelastic component to mechanical model increases the rate of initial stress relaxation.

Finally, in Fig. 3d, the strain recovery annealing experiment is illustrated. While the rate of stress relaxation depends on the assumed plastic strain rate, one definite viscoelastic effect can be demonstrated. At the end of the stress relaxation experiment when the loading device is relaxed, i.e. no elongation is imposed and the stress of the sample is at zero, the viscoelastic deformation continues if the elevated temperature is maintained. Should the deformation be purely plastic no deformation should be seen after the load is removed. The same effect can be obtained with post test annealing of the samples. Such observations of strain recovery annealing are reported by Causey et al. [10] who describe it being anelastic in nature.

4.2. Quantitative behaviour

In order to demonstrate the model capability to describe both creep and stress relaxation behaviour, we need experimental data on both experiment types performed on similar samples. These are surprisingly hard to find from open literature, as most of the experimental publications focus on either creep or stress relaxation experiments. As the cladding mechanical properties are strongly influenced by the manufacturing processes and the final heat treatment, the different samples require different model parameters.

Delobelle et al. [15] performed various experiments, including both creep and stress relaxation, for unirradiated Zircaloy-4 samples with two different experimental heat treatments. As they performed both experiments using similar samples we can use the creep experiment to determine the required material-dependent coefficients for our model and use them to simulate the stress relaxation experiment. While Ref. [15] provides a wealth of experimental data, most of it focuses on investigation of material anisotropy. In this work we use the available uniaxial data from the publication, which concerned the experiments in the axial direction for both the recrystallized (denoted by Denobelle et al. as the R sample) and the cold worked stress relieved (denoted by Denobelle et al. as the CWSR sample) Zircaloy-4 at 623 K (350 °C). The former state was achieved with a thermal treatment of 4–5 h at 973 ± 30 K and the latter with 5 h at 733 K. The data for creep experiment was taken from Fig. 16 of Ref. [15] and for stress relaxation from Fig. 15 of Ref. [15]. As all the experiments discussed in this work have been performed at the same temperature, we can focus on the mechanical response of the material.

In the creep experiments the stress was stepwise increased and the elongation measured. For R sample the stress steps used were 125, 135, 150 and 170 MPa and for the CWSR sample 170, 250 and 300 MPa. In the stress relaxation experiments the sample was deformed to a desired strain at the rate of $6.6 \cdot 10^{-4}$ s^{-1}. Then the strain was held constant for 48 h and the stress measured. The strain steps were 0.4%, 0.8%, 1.2%, and 4% for the R sample and 0.4%, 0.8%, and 1.2% for the CWSR sample, with the original zero strain kept as a reference level during the experiment.

Delobelle et al. [15] provide measured Young's modulus for both R and CWSR samples ($7.8 \bullet 10^4$ MPa and $7.3 \bullet 10^4$ MPa, respectively). These are relatively close to the MATPRO [13,24,30] formula

$$E = 1.148 \cdot 10^5 - 59.9T \text{ MPa}, \quad (7)$$

where T is temperature in K, giving $E=7.7482 \cdot 10^4$ MPa at 623 K. The reported value is used for the CWSR material. However, the R material appears to be extremely soft so that in order to use the reported value for Young's modulus and match the experimental observations we would need to assume very rapid deformation after the initial elastic jump. In the following the rapid deformation is combined with the elastic response, represented by the apparent

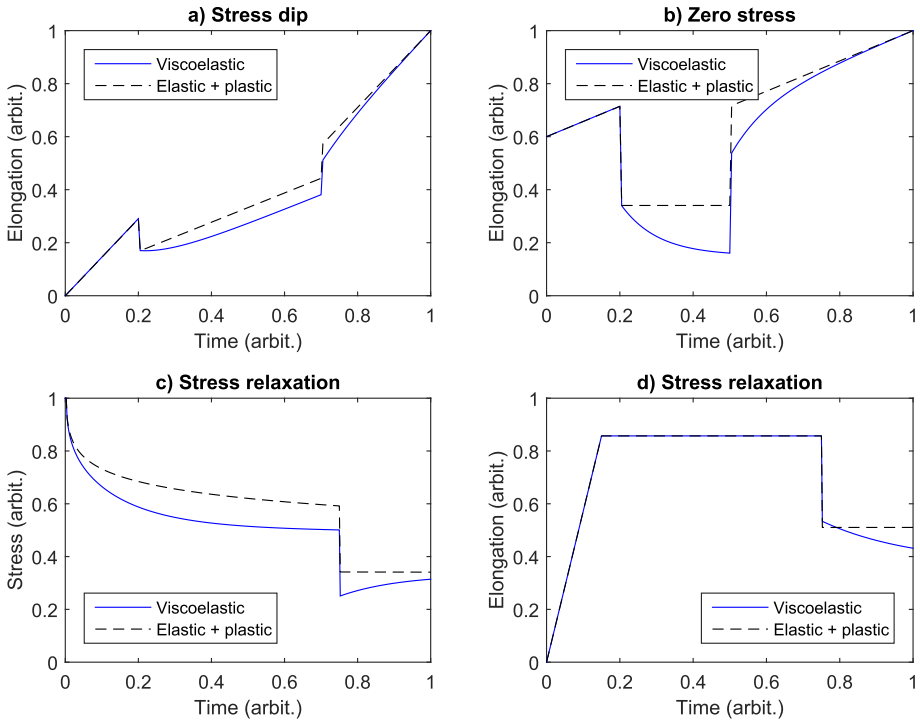

Fig. 3. Qualitative behaviour of viscoelastic model as compared to model with purely elastic and plastic components. The solid line denotes the viscoelastic model results and the dashed line a corresponding model with only elastic and plastic components. In the simulation shown in the upper left plot (a), the sample stress has first been held until steady state creep has been obtained. Then the stress is reduced for a while, and returned to its original value. The viscoelastic model shows apparent stop at stress dip, and faster elongation at return to stress. The upper right plot (b) features similar situation, but with the stress reduced to zero. The apparent deformation continues in viscoelastic model, but will return to in line with the previously achieved rate as is seen in several experiments [24,29]. The lower left plot (c) features a stress relaxation experiment where the elongation is reduced mid-experiment as per Ref. [14]. The viscoelastic model shows in this particular case an increase in stress as reported. In the lower right plot (d) the stress relaxation experiment ends with a release of the sample, yielding σ=0 at the last part of the plot. This causes a viscoelastic deformation that is not seen if the sample deformation is assumed to consist of solely elastic and plastic components.

Young's modulus of $3.9\cdot10^4$ MPa, as the coarse experimental data does not allow us to differentiate between them. This effectively reduces the maximum stresses in the stress relaxation predictions.

We use a simple engineering model for the modelling of the steady state creep:

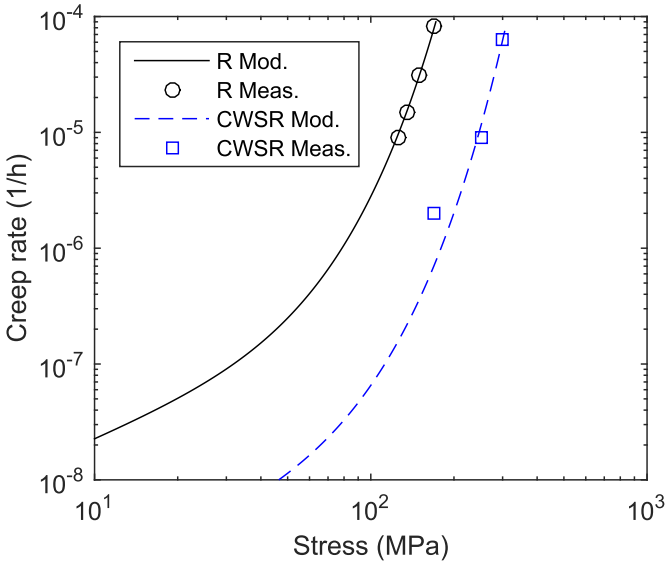

Fig. 4. Steady state creep rate for R and CWSR claddings as a function of applied stress. Lines represent model results and circles and squares values calculated from experimental data. Experimental data obtained from Fig. 6 of [15] and simulated rates as per Eq. (8).

$$\dot{\varepsilon}_t = A\sinh(B\sigma), \tag{8}$$

where A and B are coefficients fitted to the steady state creep data obtained from Fig. 6 of [15]. The coefficients are listed in Table 1 and the steady state creep rate provided by Eq. (8) as a function of applied stress is shown in Fig. 4. The use of hyperbolic sine function is a common engineering approximation used to cover both low stress region below 100 MPa where $\dot{\varepsilon}\sim\sigma$ and high stress region where $\dot{\varepsilon}\sim\sigma^5$ [31,32]. At high stress limit the hyperbolic sine tends to exponential behaviour, which is in line with power law break down region.

The first stress step is simulated for the creep experiment and the model parameters are fitted to match the experimental data. Creep experiments have been successfully modelled earlier with a $n=1$ model [5,6], and a $n=2$ model will be used to investigate the effect of increasing the number of Kelvin units. For the individual Kelvin units the strength of the springs (κ_i) determine the extent of the elongation in creep experiments and the characteristic time is determined by $\tau_i=\eta_i/\kappa_i$. For the model with $n=1$ both κ and τ are fitted to the creep experiments. For the model with $n=2$ we use τ_1 to correspond to the fast and τ_2 to the slow creep compliance, assuming $\tau_2=10\tau_1$ to limit the number of free variables and obtain a clear separation of effect of individual Kelvin units, and use Matlab optimization tools to fit the curves to the creep experiments. The resulting coefficients are listed in Table 1. The stress transient in the creep experiment is assumed to be instantaneous.

For the stress relaxation experiment all the experimental strain steps were modelled. During the periods where the strain was increased to new holding level several steps of the strain increase were modelled. In most of the cases this resulted in maximum

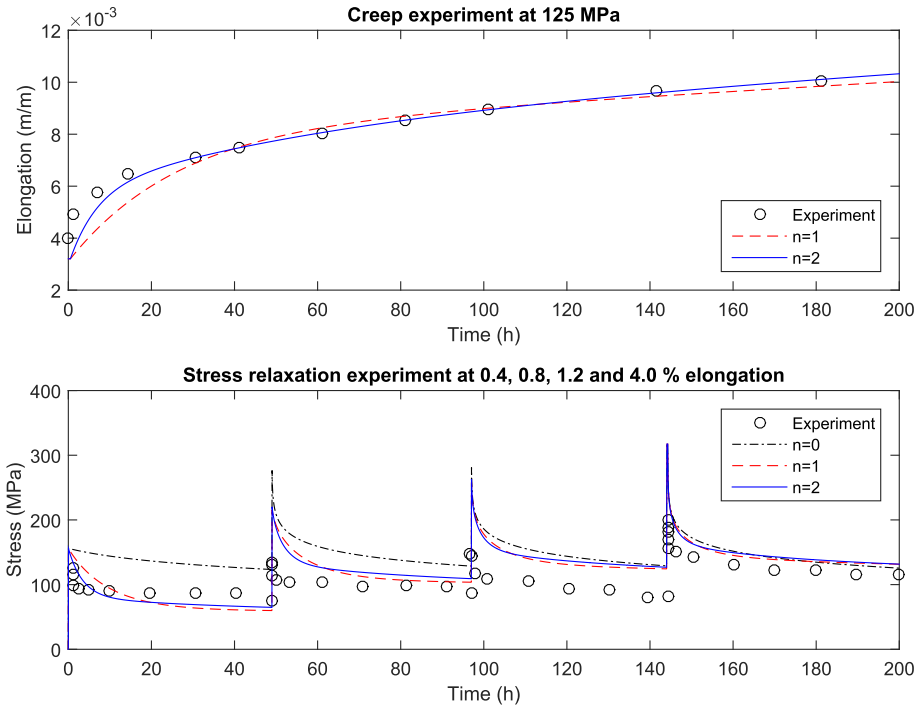

Fig. 5. Creep and relaxation of R samples. Comparison between the experimental data (circles) and simulations with model with different number n of Kelvin units. $n = 0$ represents the pure elastic and plastic deformation, $n = 1$ is the Standard Linear Solid and plastic deformation, $n = 2$ the model introduced in this paper.

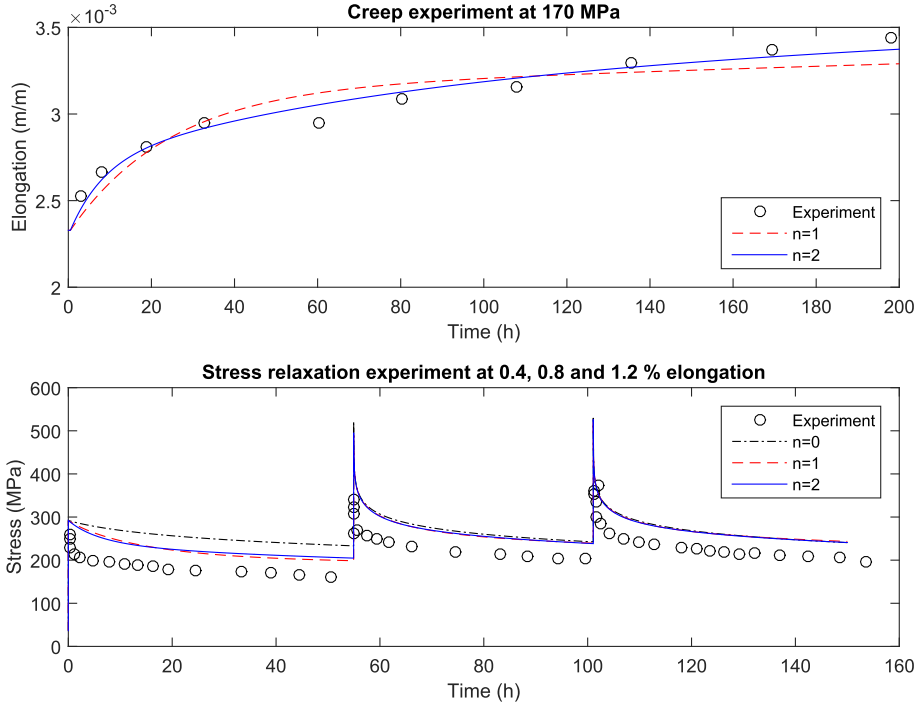

Fig. 6. Creep and relaxation of CWSR samples. Comparison between the experimental data (circles) and simulations with model with different number n of Kelvin units. $n = 0$ represents the pure elastic and plastic deformation, $n = 1$ is the Standard Linear Solid and plastic deformation, $n = 2$ the model introduced in this paper.

stress reduction of less than 5 MPa when compared to instantaneous strain. As the strain was applied at the rate of $6.6 \cdot 10^{-4}$ s^{-1} yielding strain of 0.4% in approximately 6 s, the small difference between instant and very fast strain increase is understandable. The exception was the last step of the R sample (to 4% strain) where the strain increase was high enough to require taking the relaxation into account during the increase.

The simulation of the creep and stress relaxation experiments are shown in Fig. 5 for R samples and in Fig. 6 for the CWSR samples. The simulations are performed with models with 0, 1 and 2 Kelvin units. The model with 0 Kelvin units is shown only for the stress relaxation plot, where it represents the traditional strain

Table 1
Model coefficients used to model both R and CWSR claddings.

Cladding	A (1/h)	B (1/MPa)	κ_0 (MPa)	κ_1 (MPa)	κ_2 (MPa)	τ_1 (h)	τ_2 (h)
R $n=0$	4.5168×10^{-6}	4.82×10^{-2}	3.9×10^{4}	–	–	–	–
R $n=1$	4.5168×10^{-6}	4.82×10^{-2}	3.9×10^{4}	2.52×10^{4}	–	26	–
R $n=2$	4.5168×10^{-6}	4.82×10^{-2}	3.9×10^{4}	4.80×10^{4}	4.49×10^{4}	6.5	65
CWSR $n=0$	4.2416×10^{-7}	3.43×10^{-2}	7.3×10^{4}	–	–	–	–
CWSR $n=1$	4.2416×10^{-7}	3.43×10^{-2}	7.3×10^{4}	2.08×10^{5}	–	24	–
CWSR $n=2$	4.2416×10^{-7}	3.43×10^{-2}	7.3×10^{4}	4.40×10^{5}	3.03×10^{5}	8.0	80

hardening law model in stress relaxation, as discussed in Section 2.

5. Discussion

The anelastic contribution to cladding mechanical behaviour has been investigated and accounted for in some models in the 1970s and 1980s [10,18,19]. However, later on it has been neglected [1,2,15,24], either implicitly or explicitly, and several experimentally observed cladding transient responses have remained unexplained. Yet the viscoelastic model described in this paper is able to provide a qualitative interpretation of the observations on the metal response to transient stresses such as load drops, creep reversal and quick stress relaxation. The observed time evolution of the primary creep can be explained by various concurrent processes operating at different time scales and approximated by a series of relaxation processes. In our previous work we have shown that similar models can be used to simulate various creep experiments performed both in laboratory conditions and in-pile [5,6]. The model is self consistent in the sense that the creep and stress relaxation are simulated with the single model.

Figs. 5 and 6 show the benefit of inclusion of Kelvin units to the simulation model, as both the creep and stress relaxation modelling is improved. While the creep results with the model without anelastic contribution (n=0) would not represent traditional models as there is no primary creep contribution, with the stress relaxation it provides the results corresponding to the use of strain hardening law. Increasing the number of Kelvin units enhances the correspondence between the measurements and the simulation results. This is especially noticeable in stress relaxation of R sample in Fig. 5. However, the stress relaxation experiments also demonstrate the current shortcomings of the model. The stresses, especially the maximum ones, are generally overestimated. The time evolution of the model, while qualitatively correct, is still somewhat too slow. However, for the uniaxial creep and stress relaxation, the simple model presented in this paper performs similarly to the one derived by Delobelle et al. [15].

The maximum stresses are encountered when the strain has reached the target value. They are overestimated by our model as well as the model used by the authors of the original experimental paper [15]. The stress given by the model is dominated by the elastic modulus of the material. Delobelle et al. [15] assume the reason is that during the imposing of the strain the sample plastically deforms. This is probable as the strain rate is high enough to require very fast relaxation processes if the instantaneous plastic deformation is ruled out. However there is not enough experimental data to create a strain rate dependent plastic deformation model.

The modelling of especially R specimen could be improved by using higher n to simulate a larger range of time dependent processes. However, as the data available are just a few points, that is not feasible within this work. Also, it should be noted that the current implementation presented in Eqs. (3)–(5) requires the use of time steps shorter than the smallest τ_i in the stress relaxation simulations. This limits the n to be used in an actual fuel performance application.

The comparison of Figs. 5 and 6 demonstrates that the creep strength of the material also has an effect on whether taking viscoelastic effects into account is necessary. The viscoelastic contribution to creep resistant CWSR specimen is small and this shows in the stress relaxation experiment. On the other hand in the soft R specimen the viscoelastic contribution is visible in both the creep and stress relaxation experiments. It should be noted that in-pile conditions appear to enhance the viscoelastic contribution [10] and it is not affected by the accumulated fluence according to the observations in the instrumented creep experiments performed at Halden reactor [4,8].

It should be also noted that in the stress relaxation experiments the viscoelastic behaviour has most effect on the first relaxation. This stems from the assumptions made in the model. First, initially the sample is assumed to be relaxed to zero stress, yielding the stress differential of 200–300 MPa depending on material at the start of the experiment. At subsequent strain jumps this difference is somewhat smaller. And while the viscoelastic part is assumed to be linear and to operate on the stress difference, the plastic part of the model depends on the stress and is strongly non-linear in the region of the later strain steps.

6. Conclusions

Accurate modelling of nuclear fuel cladding mechanical behaviour is important for both fuel performance and safety analysis. The mechanical response to transient stresses has traditionally been analysed as consisting of elastic and (visco)plastic components, with the latter containing all non-instantaneous phenomena. Usually the changing conditions have been taken into account by strain hardening rule, which is an engineering approximation assuming accumulated creep strain stays invariant when the conditions change. Historically the anelastic contribution to nuclear fuel cladding mechanical behaviour has been identified. However for some reason it has not been taken into account in the models currently in use in nuclear fuel behaviour analysis. This has lead to the inability to explain several experimental observations such as re-initiation of in-pile primary creep.

In this paper we have derived a model for describing both the creep and the stress relaxation using the methods from the theory of viscoelasticity. An appropriate model formulation has been designed based on the application, and its ability to model cladding mechanical transients has been demonstrated. Also, an interpretation on the observed time-dependence of the primary creep evolution has been provided. Based on the analysis presented we argue that the inclusion of anelastic contribution to the cladding mechanical models provides a simple way to improve the simulation results. While the effect is most pronounced at small strain jumps and low stress situations, it should be noted that both slow strain rates and reactor conditions can be expected to make the viscoelastic effects more important.

The ultimate goal of the research presented is a creation of a cladding mechanical model both capable of consistent description

of creep and stress relaxation behaviour and implementable to a fuel behaviour code. The remaining major methodological challenges are the cladding response to the changes in temperature and the correspondence between the in-pile and the out-of-pile cladding behaviour. These, along with the validity of the assumption made in this work that the anelastic part of the model is initialized at rest, are to be investigated in the future.

Acknowledgements

This work was partially funded by SAFIR2014, the Finnish Research Programme on Nuclear Power Plant Safety 2011-2014, and Academy of Finland funded IDEA project (grant decision number 260493).

References

[1] G. Lucas, R. Pelloux, Nucl. Technol. 53 (1981) 46–57.
[2] Y. Matsuo, ASTM STP 1023 (1989) 678–691.
[3] M. McGrath, in: Proceedings of the 2000 International Topical Meeting on LWR Fuel Performance, 2000.
[4] J. Foster, M. McGrath, in: Proceedings of the 2007 LWR Fuel Performance Meeting, 2007.
[5] V. Tulkki, T. Ikonen, J. Nucl. Mater. 445 (2014) 98–103.
[6] V. Tulkki, T. Ikonen, J. Nucl. Mater. 457 (2015) 324–329.
[7] H. Banks, S. Hu, Z. Kenz, Adv. Appl. Math. Mech. 3 (2011) 1–51.
[8] S. Hanawa, HWR-882, 2008.
[9] D. Fraser, P. Ross-Ross, A. Causey, J. Nucl. Mater. 46 (1973) 281–292.
[10] A. Causey, F. Butcher, S. Donohue, J. Nucl. Mater. 159 (1988) 101–113.
[11] Y. Long, C. Beard, S. Henk, G. Zhou, in: Proceedings of 2010 LWR Fuel Performance Meeting, 2010. Paper 054.
[12] G. Zhou, L. Hallstadius, G. Wikmark, Y. Long, J. Foster, in: Proceedings of 2011 Water Reactor Fuel Performance Meeting, 2011. Paper T2–038.
[13] Y. Matsuo, J. Nucl. Sci. Technol. 24 (1987) 111–119.
[14] R. Kapoor, S. Wadekar, J. Chakravartty, Mater. Sci. Eng. A 328 (2002) 324–333.
[15] P. Delobelle, P. Robinet, P. Geyer, P. Bouffioux, J. Nucl. Mater. 238 (1996) 135–162.
[16] L. Jernkvist, in: Transactions of the 15th International Conference on Structural Mechanics in Reactor Technology (SMiRT-15) C04/3, 1999, pp. 477–484.
[17] M. Rautenberg, D. Poquillon, P. Pilvin, C. Grosjean, J. Cloue, X. Feaugas, Nucl. Eng. Des. 269 (2014) 33–37.
[18] F. Povolo, B. Molinas, J. Nucl. Mater. 114 (1983) 85–94.
[19] K. Murty, K. Yoon, in: Transactions of the 5th International Conference on Structural Mechanics in Reactor Technology (SMiRT-5) C3/6, 1979.
[20] A. Nowick, B. Berry, Anelastic Relaxation in Crystalline Solids, Academic Press, New York, 1972.
[21] M. Blanter, I. Golovin, H. Neuhuser, H. Sinning, Internal Friction in Metallic Materials: a Handbook, Springer, 2007.
[22] F. Nabarro, F. de Villiers, Physics of Creep and Creep-resistant Alloys, CRC Press, 1995.
[23] D. Gutierrez-Lemini, Engineering Viscoelasticity, Springer, 2014.
[24] M. Limback, T. Andersson, ASTM STP 1295 (1996) 448–468.
[25] R. Kohlrausch, Pogg. Ann. Phys. Chem. 91 (1854) 179.
[26] R. Anderssen, S. Husain, R. Loy, Anziam J. 45 (2004) C800–C816.
[27] R.S. Anderssen, M.P. Edwards, S.A. Husain, R.J. Loy, in: 19th International Congress on Modelling and Simulation, 2011, pp. 263–269.
[28] F. Garzarolli, H. Stehle, E. Steinberg, ASTM STP 1295 (1996) 12–32.
[29] R. Kozar, A. Jaworski, T. Webb, R. Smith, J. Nucl. Mater. 444 (2014) 14–22.
[30] W. Luscher, K. Geelhood, NUREG/CR-7024, 2011.
[31] T. Hayes, M. Kassner, R. Rosen, Metallurgical Mater. Trans. A 33A (2002) 337–343.
[32] T. Hayes, M. Kassner, Metallurgical Mater. Trans. A 37 A (2006) 2389–2396.

Series title and number

VTT Science 109

Title	**Modelling nuclear fuel behaviour and cladding viscoelastic response**
Author(s)	Ville Tulkki
Abstract	In light water reactors the nuclear fuel is in the form of uranium dioxide pellets stacked inside a thin-walled tube made from Zirconium alloy. The fuel rods provide the first barriers to the release of radioactivity as the isotopes are contained within the fuel matrix and the cladding tubes. Fuel behaviour analysis investigates the state of the fuel at given boundary conditions and irradiation history. The scope of this thesis consists of two main themes. The first is the uncertainty and sensitivity in fuel behaviour modelling and the tools required for its propagation to the rest of the nuclear reactor calculation chain. The second is the analysis and modelling of cladding response to transient stresses. A nuclear reactor is a strongly coupled system. The neutronics depend on the fuel and coolant temperature, the fuel temperature on the neutronics and the heat flux to coolant and coolant thermal hydraulics on the amount of heat transferred from the fuel. Propagation of uncertainties through the nuclear reactor calculation chain is an international on-going effort, and the complex interactions in the fuel rods make them challenging to analyze. In this thesis uncertainty and sensitivity of fuel behaviour codes is investigated and the development of a fuel module suitable for propagation of the uncertainties is detailed. The creep response of a cladding tube to changing conditions is conventionally modelled using the strain hardening rule. The rule assumes accumulated strain to be invariant during changes in the conditions, and is relatively simple to utilize. However, the original experiments which are used to justify the use of the strain hardening rule show that it applies only to a restricted set of conditions. In this thesis a simple methodology for predicting fuel cladding macroscopic response to stresses and imposed strains is developed by taking anelastic behaviour into account. The model is shown to perform well in describing both creep and stress relaxation experiments.
ISBN, ISSN, URN	ISBN 978-951-38-8346-1 (Soft back ed.) ISBN 978-951-38-8347-8 (URL: http://www.vttresearch.com/impact/publications) ISSN-L 2242-119X ISSN 2242-119X (Print) ISSN 2242-1203 (Online) http://urn.fi/URN:ISBN:978-951-38-8347-8
Date	October 2015
Language	English, Finnish abstract
Pages	65 p. + app. 56 p.
Name of the project	
Commissioned by	
Keywords	Nuclear fuel behaviour, modelling, uncertainty and sensitivity analysis, cladding creep, stress relaxation, viscoelasticity
Publisher	VTT Technical Research Centre of Finland Ltd P.O. Box 1000, FI-02044 VTT, Finland, Tel. 020 722 111

Julkaisun sarja ja numero

VTT Science 109

Nimeke	**Ydinpolttoaineen käyttäytymisen ja suojakuoren viskoelastisen vasteen mallinnus**
Tekijä(t)	Ville Tulkki
Tiivistelmä	Kevytvesireaktoreissa ydinpolttoaine koostuu uraanidioksiditableteista, jotka on pinottu ohuen zirkonium-metalliseoksesta valmistetun putken sisään. Polttoainesauvat muodostavat ensimmäiset esteet radioaktiivisten aineiden leviämiselle. Polttoaineen käyttäytymisen tutkimus tarkastelee polttoaineen tilaa annetuilla tehohistorioilla ja reunaehdoilla. Tämä väitöskirja käsittelee kahta teemaa: Ensimmäinen on epävarmuus- ja herkkyysanalyysit polttoaineen mallinnuksessa ja työkalut epävarmuusinformaation kuljetukseen ydinreaktorianalyysin laskentaketjussa. Toinen on suojakuoren jännitysvasteen analyysi ja mallinnus. Ydinreaktori on vahvasti kytkeytynyt systeemi. Neutroniikka riippuu polttoaineen ja jäähdytteen lämpötilasta, polttoaineen lämpötila neutroniikasta ja lämpövuosta jäähdytteeseen ja jäähdytteen termohydrauliikka polttoaineesta siirtyvästä lämpöenergiasta. Epävarmuuksien kuljetus laskentaketjun läpi on kansainvälinen käynnissä oleva työ, ja polttoaineen osalta monimutkaiset vuorovaikutukset tekevät siitä haasteellista. Tässä väitöstyössä on tutkittu polttoainekoodien epävarmuutta ja herkkyyttä lähtösuureiden epävarmuudelle. Epävarmuusinformaation kuljetusta reaktorianalyysiketjussa varten on aloitettu uuden polttoainemallin kehitys. Perinteisesti suojakuoriputken virumisvaste vaihtuviin olosuhteisiin on mallinnettu käyttäen ns. "strain hardening" -sääntöä. Säännössä oletetaan venymän pysyvän vakiona olosuhteiden vaihtuessa, ja se on verrattain helppokäyttöinen. Kuitenkin alkuperäiset kokeet joilla säännön käyttö perustellaan osoittavat, että se pätee vain rajattuihin tapauksiin. Tässä väitöskirjassa esitetään yksinkertainen metodologia, jolla ennakoidaan polttoaineen suojakuoriputken makroskooppista vastetta jännityksiin ja pakotettuihin venymiin ottamalla anelastinen käyttäytyminen huomioon. Mallin näytetään suoriutuvan hyvin sekä virumis- että jännitysrelaksaatiokokeiden mallinnuksessa.
ISBN, ISSN, URN	ISBN 978-951-38-8346-1 (nid.) ISBN 978-951-38-8347-8 (URL: http://www.vtt.fi/julkaisut) ISSN-L 2242-119X ISSN 2242-119X (Painettu) ISSN 2242-1203 (Verkkojulkaisu) http://urn.fi/URN:ISBN:978-951-38-8347-8
Julkaisuaika	Lokakuu 2015
Kieli	Englanti, suomenkielinen tiivistelmä
Sivumäärä	65 s. + liitt. 56 s.
Projektin nimi	
Rahoittajat	
Avainsanat	Ydinpolttoaineen käyttäytyminen, mallinnus, epävarmuus- ja herkkyysanalyysi, viruminen, jännitysrelaksaatio, viskoelastisuus
Julkaisija	Teknologian tutkimuskeskus VTT Oy PL 1000, 02044 VTT, puh. 020 722 111

Modelling nuclear fuel behaviour and cladding viscoelastic response

In light water reactors the nuclear fuel is in the form of uranium dioxide pellets stacked inside a thin-walled tube made from Zirconium alloy. The fuel rods provide the first barriers to the release of radioactivity as the isotopes are contained within the fuel matrix and the cladding tubes. Fuel behaviour analysis investigates the state of the fuel at given boundary conditions and irradiation history.

The scope of this thesis consists of two themes: The uncertainty and sensitivity in fuel behaviour modelling and the analysis and modelling of cladding response to transient stresses.

A nuclear reactor is a strongly coupled system and the complex interactions in the fuel rods make them especially challenging to analyze. In this thesis the uncertainty and sensitivity of fuel behaviour codes is investigated and the development of a fuel module suitable for propagation of the uncertainties is detailed.

The creep response of a cladding tube to changing conditions is conventionally modelled using the strain hardening rule. While simple to utilize, the original experiments which are used to justify its use show that it applies only to a restricted set of conditions. In this thesis a simple methodology for predicting fuel cladding macroscopic response to stresses and imposed strains is developed by taking anelastic behaviour into account. The model is shown to perform well in describing both creep and stress relaxation experiments.

ISBN 978-951-38-8346-1 (Soft back ed.)
ISBN 978-951-38-8347-8 (URL: http://www.vttresearch.com/impact/publications)
ISSN-L 2242-119X
ISSN 2242-119X (Print)
ISSN 2242-1203 (Online)
http://urn.fi/URN:ISBN:978-951-38-8347-8